Contents

Citations to Previously Published Work

The whole chapter 3 and most of chapter 4 appeared in the following paper:

> ”Understanding Hydrogen Atom Adsorption on Graphene”,
> S. Casolo, O.M. Løvvik, R. Martinazzo and G.F. Tantardini
> J. Chem. Phys **130**, 054704 (2009), `cond.matt/0808.1312`;

The dynamical study of chapter 5 is now in press as

> “Quantum dynamics of the Eley-Rideal hydrogen formation reaction on graphite at typical interstellar cloud conditions”, J. Phys. Chem. A doi:10.1021/jp9040265

The last part of chapter 4 will be part of a paper now in preparation.
Electronic preprints (shown in `typewriter font`) are available on the Internet at the following URL:

> `http://arXiv.org`

Acknowledgments

I gratefully acknowledge my supervisor Prof. Gian Franco Tantardini for his precious guide and support during my PhD. He gave me not only the opportunity to become a scientist and do research in surface science, but also the freedom to do it according to my aspirations and needs. My ”second” supervisors, Rocco Martinazzo, and Ole Martin Løvvik are also very warmly acknowledged. Rocco has an ability to cut through reams of algebra with a single visual explanation that I will always admire, and I have learned a great deal of physics from him even though I often tend to be orthogonal to mathematical reasoning. Ole Martin guided me during my stay in Oslo and taught me the DFT, material science and how to survive in Norway. Both of them are, other than great scientists, good friends without whom this period would not have been the same.

I cannot omit the people who have been close to me in these years. In Oslo I met great people from which I learned a lot. The one with whom I have collaborated the most is Espen Flage-Larsen, black belt of installing and testing software, but all the others in the structural physics and in the solid state ionics group in Oslo are acknowledge. In particular Demie Kepaptsoglou and Niina Jalarvo are the most nice and witty people one could possibly hope to spend a lunch-break gossiping with. Together we had tons of fun and eventually some science in between. I will always remember my stay in Oslo with them two: and I will never smile again to a pregnant woman if I am not the baby's father.
Francesca and her family have been fundamental for my survivor in the great north, to them goes a special thank. A big hug to all the others (I hope it will be large enough to enclose Rob).

From the Italian side all my colleagues: Fausto, Matteo, Stephanie, Marco, Angelo, Ahmed, Elena, Valentina, Mattia, Simone, etc. are also acknowledged together with life-long friends that supported my fragile ego during this three years.

My family, of course, was the strongest pillar that supported me so far: the warmest thank is for them.

Finally, Natalia s(u/o)pported me over the (almost) last two years: she is the best souvenir I could take home from Norway. She has seen my best and my worst, and despite that provided me love and support. She washed hundreds of my dishes, lovely.

Chapter 1

Graphene and Graphite Structures

In this section we will introduce lattice and electronic structure of graphene and graphite. This two materials are indeed very similar, being the first the two-dimensional limit of the latter. Nevertheless this limit shows extraordinary features, in particular in its electronic structure: graphene's charge carriers (both electrons and holes) behave as pseudo-relativistic particles making this material a bridge between condensed matter physics and quantum electrodynamics.
The chapter is divided in two parts: the first will focus on the graphene lattice and its electronic structure, with emphasis on some among the many consequences of having pseudo-relativistic electrons and on the application in a future carbon-based electronics [1]. The second will present graphite and show why graphene can be used as a valid model for graphite surface simulations such as the one in chapter 5. It will also be mentioned the importance of the interaction between hydrogen atoms and this materials: both for fundamental science, for instance to understand the hydrogen recombination in the interstellar medium, and in technology *e.g.* in hydrogen storage, nuclear fusion reactors and nano-electronics.

1.1 Graphene Lattice Structure

Graphene is a single graphite layer. Since the crystalline ordering is then confined to a single plane, its unit cell is a two dimensional hexagonal Bravais lattice. As it can be seen in fig.1.1 the two atoms in cell form a honeycomb structure owing to the symmetry point group D_{6h} and space group D_{6h}^4 (or $P/6mmm$ following

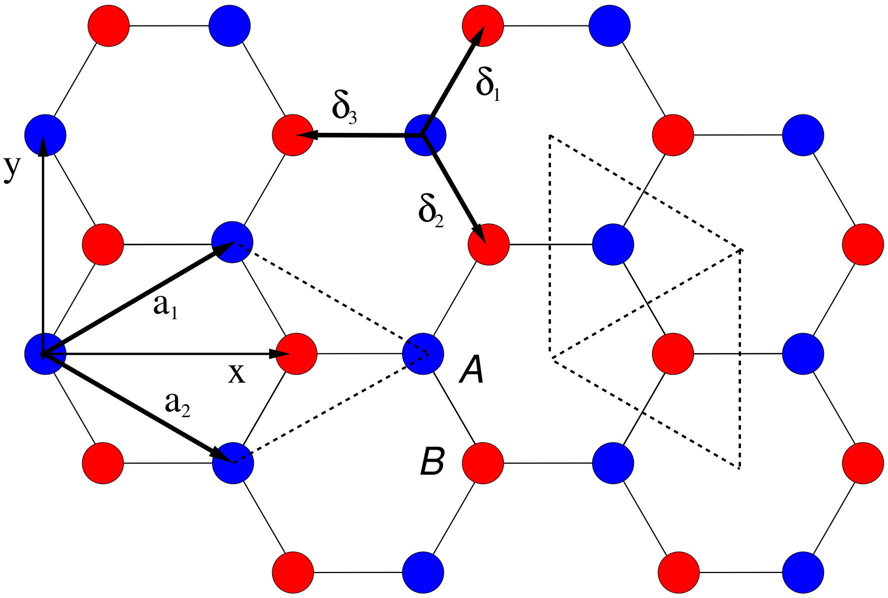

Figure 1.1: Graphene lattice in real space. The unit cell is defined by the two lattice vectors $\mathbf{a}_1$ and $\mathbf{a}_2$, and contains two atoms belonging to different sublattices: A (blue) and B (red). The nearest neighbours vectors δ_i and the sublattices unit cells are also shown.

Hermann-Mauguin notation). The lattice vectors have coordinates

$$\mathbf{a}_1 = d\left(\frac{3}{2};\frac{\sqrt{3}}{2}\right) \qquad \mathbf{a}_2 = d\left(\frac{3}{2};-\frac{\sqrt{3}}{2}\right) \tag{1.1}$$

where d=1.42 Å is the carbon-carbon bond distance and the lattice constant is a=2.42 Å. The two atoms in cell are located at (in direct cell coordinates, *i.e.* as Wyckoff positions)

$$\mathbf{C}_1 = [0;0] \qquad \mathbf{C}_2 = \left[\frac{2}{3};\frac{2}{3}\right] \tag{1.2}$$

Each of the two spans alone a different triangular sublattice, labeled A and B, made of every second carbon atom, so every atom has as nearest neighbours three sites belonging to the other sublattice. Structures of this kind are known as *bipartite* lattices: a condition with important consequences on the system's Hamiltonian, so on its electronic structure as shown in appendix A. Note that each sublattice alone shows the same point group symmetry as the full graphene lattice but a different space group.

Graphene unit cell in momentum (k)-space: the unit vectors are $\mathbf{b}_1$ and $\mathbf{b}_2$. Graphene's first Brilloiun zone is shown in fig.1.2, together with its construction

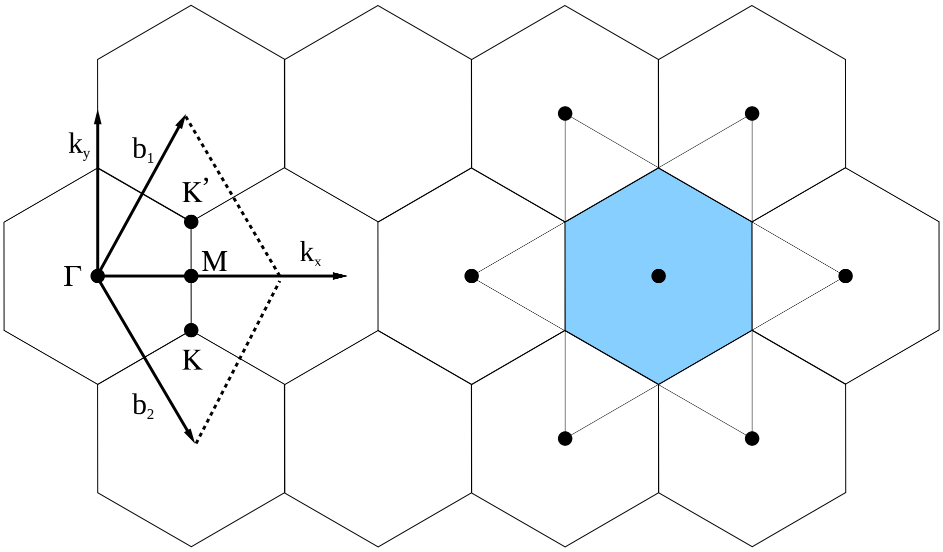

Figure 1.2: The first Brillouin is built and shown in light blue together with the special points Γ, M, and the K, K' points.

from the reciprocal lattice nodes. The reciprocal lattice vectors are

$$\mathbf{b}_1 = \frac{2\pi}{d}\left(\frac{1}{3};\frac{1}{\sqrt{3}}\right) \qquad \mathbf{b}_2 = \frac{2\pi}{d}\left(\frac{1}{2};-\frac{1}{\sqrt{3}}\right) \tag{1.3}$$

Here the shape of the Wigner-Seitz and Brillouin zones is the same, although they are rotated by $\pi/2$. In this two dimensional Brillouin zone there are only three nonequivalent special k-points (other than Γ) at the positions (in direct cell coordinates respect to reciprocal lattice vectors)

$$\mathbf{K} = \left[\frac{1}{3};\frac{2}{3}\right] \qquad \mathbf{K}' = \left[\frac{1}{3};\frac{2}{3}\right] \qquad \mathbf{M} = \left[\frac{1}{2};\frac{1}{2}\right] \tag{1.4}$$

The $\mathbf{K}$ and $\mathbf{K}'$ points are very important for graphene since the Fermi surface is present only at these points. The point group here is D_{3h} that supports two dimensional irreducible representations: so the two points are degenerate in energy. Moreover they are related by time reversal symmetry since the Bloch function for $\mathbf{K}$ is mapped in $\mathbf{K}'$ by a center of inversion ($\mathbf{K}' = -\mathbf{K}$).

$$T\,|\psi(\mathbf{K})\rangle = Te^{i\mathbf{K}\cdot\mathbf{r}}u_{\mathbf{K}}(\mathbf{r}) = e^{-i\mathbf{K}\cdot\mathbf{r}}u_{-\mathbf{K}}(\mathbf{r}) = |\psi(\mathbf{K}')\rangle \tag{1.5}$$

1.1.1 Graphene as Two-Dimensional Crystal

The existence of free standing graphene is by itself everything but a trivial fact. The physics community believed for decades that was not possible to

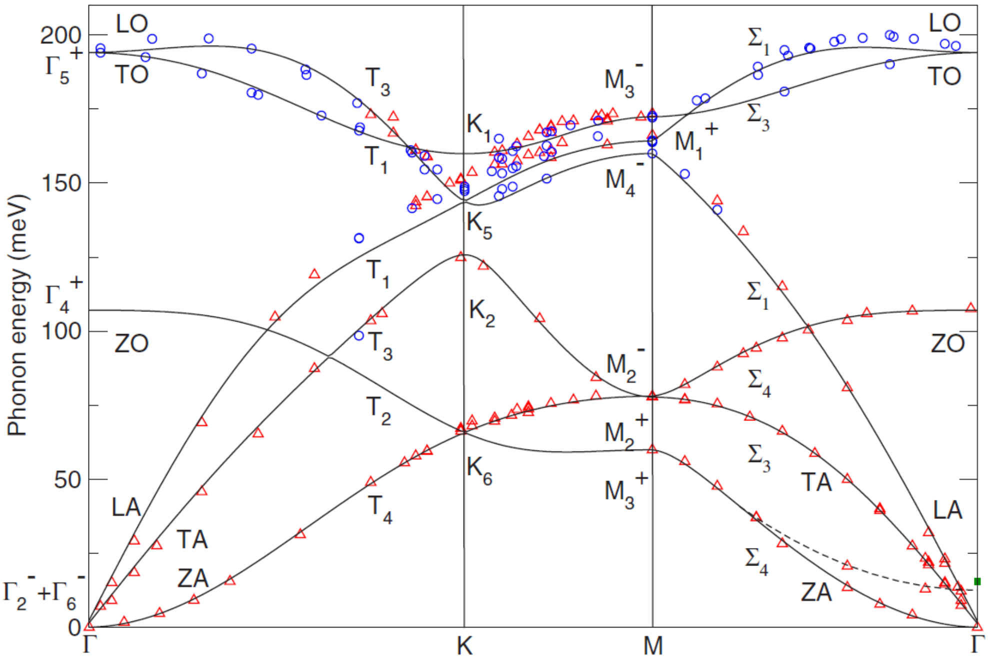

Figure 1.3: Phononic band structure in graphene taken from ref.[9]. Red and blue marks come from two different experimental studies, while black lines are results form a theoretical tight-binding calculation.

have crystalline order in less than three dimensions. This result is known as the Mermin-Wagner theorem: a rather complex mathematical theory that extended some results by Landau and Peierls. They showed that thermal fluctuations (as a phononic contribution) at any finite temperature should destroy the crystalline order for any infinite two-dimensional solid [2, 3, 4, 5, 6]. For this reason when single layer graphene has been syntetized in 2004, first on a support and then as a free standing membrane [7, 8] this was seen as a real breakthrough.

In solids acoustic modes correspond to translations of atoms, while optical modes to stretching bonds in the lattice. In the long wave length limit (as $k \to 0$) the first should have a linear energy dispersion, because their frequency goes as a sine function centered at Γ, while the latter usually have a quasi-constant dispersions. Restricting the atomic motion to in-plane displacement only, graphene's two atoms in cell should generate two acoustic and two two optical phonons branches, instead, being atoms free to move also in the out-of-plane direction, graphene shows overall 3 acoustic (with $A_{2u} + E_{1u}$ symmetry) and 3 optical (with $B_{2g} + E_{2g}$ symmetry) phonon modes. [9, 10]. In the out-of-plane acoustic mode, known as the flexural mode, is a free translation since normally to the graphene plane no lattice site is connected with any other atom, so its frequency $\omega(k)$ is proportional to $\propto k^2$. In fig 1.3 is shown the graphene phononic band structure. It is possible to notice how close to Γ the flexural acoustic mode has a parabolic dispersion, while the others show a quasi-linear behaviour. When considering now the number of flexural phonons per unit area one have to integrate the Bose-Einstein distribution n_k all over the occupied k states

$$N_{ph} = \int n_k \frac{d^2\mathbf{k}}{(2\pi)^2} = \frac{1}{(2\pi)^2} \int_0^\infty \frac{k\ dk}{e^{\alpha\beta k^2} - 1} \tag{1.6}$$

this integral diverges logarithmically in the infrared limit ($k \to 0$), hence at every temperature an infinite number of out-of-plane modes will lead to the crumpling of the graphene sheet and the to lose the crystalline order. This result holds for every two dimensional solid as far as the harmonic approximation is valid. However in a finite size system one might limit the integral in eq.1.6 introducing a lower bound by a cutoff $k_{min} = \frac{2\pi}{L_T}$ to make it finite whenever the crystal dimension $L \ll L_T$: a size limit for two-dimensional ordered structures. Carrying on a more detailed analysis, after having introduced the elastic properties of the material, the dimension limit for graphene turns to be less then 1 Å at T=300 K, indicating that free-floating graphene should always crumple in the third dimension at room temperature conditions in order to stabilize it energy [11]. More recently it has been shown that the coupling between in- and out-of plane modes can also drive graphene to a metastable flat phase at reasonable temperatures [12].

In the much more stable graphite most of the 12 phonon branches are nearly doubly degenerate very close on shape to graphene ones. Nevertheless this divergent number of flexural modes does not occur. Indeed close to the Γ point the interaction between different graphene sheets splits some of the quadratic acoustic modes degeneracy into a *linear* acoustic and an optical mode that for $k = 0$ have a finite value. In this way the integral in eq.1.6 is well behaved at every k value and so graphite turns to be thermodynamically stable at room temperature.

1.2 Graphene Electronic Structure

Graphene has a very peculiar electronic structure. With its four valence electrons carbon has an half filled shell that can hybridize to form complex bonds. In graphene the atoms are connected each other trough three very stable σ bonds coming from the overlap of carbons sp^2 hybrid orbitals. This states are rather

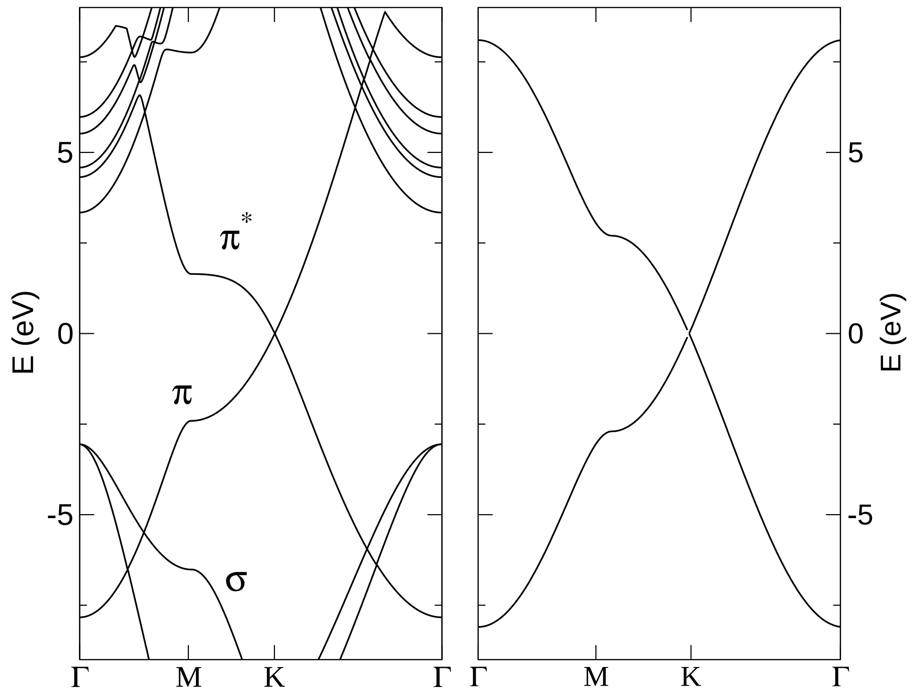

Figure 1.4: Graphene band structure computed with DFT (left panel) and π-model tight-binding calculation. The Fermi energy has been set as the zero in the energy scale.

deep in the valence band, and very seldom involved in the electronic properties of graphene. The other available electron lay in p_z orbitals, whose overlap gives rise to the π bonds, extended all over the lattice in an aromatic network such as in benzene or in other polycyclic aromatic hydrocarbons.

The band structure along the high symmetry directions in graphene is shown in fig.1.2. The most important feature here is the crossing of π (valence) and π^* (conduction) bands exactly at the Fermi energy. In building up a Hamiltonian for graphene one can then consider only the π contribution in order to obtain an effective model for states close to the charge neutrality point. For instance is possible to use the following Hamiltonian, here in its second quantization form, in which interactions can be seen as electron hoppings from one p_z orbital to any of its neighbours.

$$\hat{H} = \sum_{<i,j>} \sum_{\sigma=\uparrow,\downarrow} -t \left(\hat{a}^{\dagger}_{i,\sigma} \hat{b}_{j,\sigma} + h.c. \right) \tag{1.7}$$

Here $a^{\dagger}_{i,\sigma}$ creates an electron with spin σ on the i lattice site, part of the A sublattice and its conjugate complex will annihilate it. In the same fashion $b^{\dagger}_{j,\sigma}$

($b_{j,\sigma}$) will create (annihilate) an electron on the j in the B sublattice. The sum in eq.1.7 is limited to nearest-neighbours sites but, if necessary, further nearest-neighbours orders can be easily added to the Hamiltonian.
Such a simple single-particle description, known as the *tight-binding* model, is already surprisingly accurate in describing graphene electronic structure close to the Fermi energy as shown in fig.1.2. Its eigenvalues (see appendix A for details) are:

$$E(\mathbf{k})_{\pm} = \pm t\sqrt{3 + 2\cos\left(\sqrt{3}dk_x\right) + 4\cos\left(\frac{3}{2}dk_x\right)\cos\left(\frac{\sqrt{3}}{2}dk_y\right)} \tag{1.8}$$

where the minus (plus) sign represents the π (π^*) band. From this dispersion equation is possible to locate the zeroes, *i.e.* the Fermi surface, in two points in the Brillouin zone, corresponding to special points $\mathbf{K}$ and $\mathbf{K}'$ where the $\pi - \pi^*$ bands have an intersection due to symmetry reasons (see appendix A). Looking at the density of states, the presence of the two cones at the Fermi energy makes it linearly vanishing in that point. Hence graphene is a semi-metallic solid with no band gap but zero density of states at the charge neutrality point.
Expanding the hamiltonian at the first order in the momentum close to $\mathbf{K}, \mathbf{K}'$, one obtains (see appendix A)

$$\mathbf{k} = \mathbf{K} + \mathbf{q} \tag{1.9}$$

$$\hat{H}_{\mathbf{K}} = \nu_F \begin{pmatrix} 0 & q_x + iq_y \\ q_x - iq_y & 0 \end{pmatrix} \tag{1.10}$$

$$\hat{H}_{\mathbf{K}} = \nu_F \sigma \cdot \mathbf{p} \qquad \hat{H}_{\mathbf{K}'} = -\nu_F \sigma \cdot \mathbf{p} \tag{1.11}$$

where the σ are Pauli matrices and ν_F the Fermi velocity. For momentum values close enough to the Fermi energy the intersection is conical so the band structure is isotropic and *linear*

$$E(\mathbf{q}) = \pm \nu_F q \tag{1.12}$$

where $\nu_F = 3ta/2$ is the Fermi velocity and ($\mathbf{q}$ the momentum vector relative to $\mathbf{K}$ ($\mathbf{K}'$). The Hamiltonian in eq.1.11 is indeed the same as in Dirac's equation for massless relativistic fermions, that have the same *linear* energy dispersion. Note that the Dirac-like Hamiltonian in eq.1.11 contains ν_F in place of c: this means that electrons in graphene will follow the laws of (massless) relativistic particles but with a much smaller velocity, the Fermi velocity, as an effective speed of light.

The eigenvectors close to **K** have the form of:

$$\psi_{\pm,\mathbf{K}}(\mathbf{q}) = \frac{1}{\sqrt{2}} \begin{pmatrix} 1 \\ s\ e^{i\theta} \end{pmatrix} e^{i\mathbf{q}\cdot\mathbf{r}} \tag{1.13}$$

$$u(\mathbf{q}, s) = s\ e^{i\theta} \qquad \theta = \arctan(q_x/q_y) \tag{1.14}$$

where $s = \pm 1 = \mathrm{sign}(E)$: minus for the π and plus for π^* band. This particular mathematical form is another consequence of the linear band dispersion close to K, and it is responsible for some of the peculiar effects shown by graphene electrons.

1.2.1 Graphene's Massless Dirac Fermions

As shown before, graphene's Fermi surface is made of two independent points: **K** and **K′** (also known as Dirac points). The Dirac's equation is the analogous of Schrödinger's equation for relativistic particles and has a spectrum (for two spatial dimensions)

$$E(\mathbf{k}) = \pm\sqrt{m^2c^4 + k^2c^2} \tag{1.15}$$

where m is now the *rest* mass of the particle. Now, setting the rest mass to zero and replacing c with ν_F one recovers the graphene linear spectrum close to **K**: in this sense one can say that electrons in graphene behave as massless Dirac particles because of the $\pi - \pi^*$ conical intersection at the Fermi energy [13, 14]. Dirac fermions eigenstates, as in eq.1.13, are indeed two-dimensional spinors, whose components represents the quantum amplitudes of the wave function onto the two sublattices. This particles show particular mathematical properties responsible of many interesting physical phenomena *e.g.* the anomalous quantum hall effect, Klein tunneling, etc.

When a gate potential is applied to graphene, the Fermi energy rises or falls in one of the two cones. Above zero energy (in the upper cone), the charge carriers are negatively charged electrons. Otherwise, at negative bias (lower cone) the valence band is not completely filled so the unoccupied electronic states behave as holes, which are often viewed as a condensed-matter equivalent of positrons. Holes moves in the opposite direction as electrons and are positively charged. The value of the eigenstate's projection along the momentum direction **q** close to **K** is s (see also appendix A),

$$\langle\psi_K|\hat{\sigma}|\psi_K\rangle = \psi^\dagger\sigma_x\psi \cdot \hat{q}_y + \psi^\dagger\sigma_y\psi \cdot \hat{q}_y = s \tag{1.16}$$

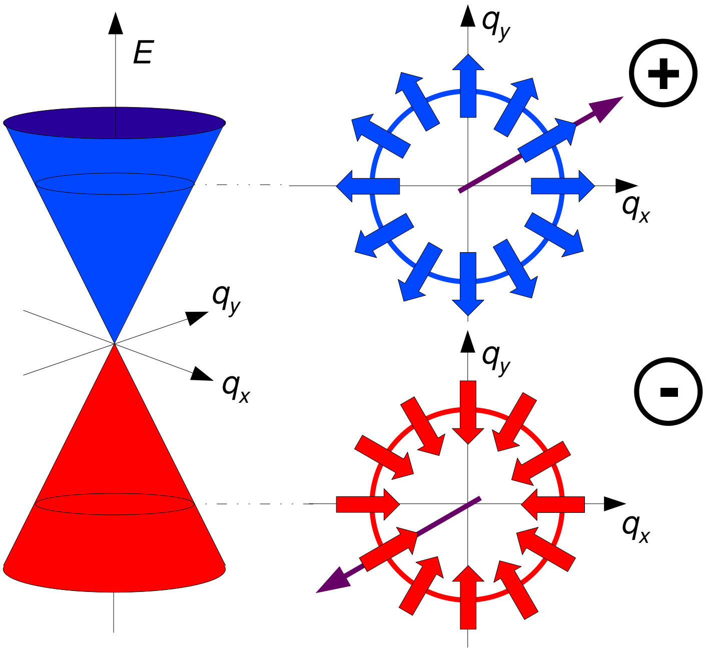

Figure 1.5: Two cuts of the Dirac cones in graphene band structure at **K**. When the Fermi energy lays in the upper cone charge carriers are electrons and their momentum (purple arrow) is parallel to the pseudospin (bold arrows). Otherwise, when E_F is in the lower cone, carriers are holes whose momentum points in the opposite direction and is anti-parallel to the pseudospin. Hence the two cones have opposite chiralities, positive for the upper and negative for the lower one.

hence it points toward the cone axis for holes (against $\mathbf{q}$) and outward for electrons (along $\mathbf{q}$), as shown in fig.1.5. This projection is known as *pseudospin* and it is closely connected with the two sublattices of graphene since it is the sign of the two sublattices contributions ratio. The projection of pseudospin along the direction of motion is known as *chirality* (since it is related to the chirality degree of freedom of wavefunctions is quantum electrodynamics) and here is positive and negative for electrons and holes, respectively. Chirality is a good quantum number close to the Dirac point: in this framework one can say that electrons in graphene behave as massless chiral fermions.

1.2.2 Pseudo-Relativistic Electrons Properties

Among the peculiar effects of pseudo-relativistic massless fermions we will focus here on the two most known, as an example of the striking differences between electrons in classical semiconducting materials and in graphene [15, 11]. The first is known in relativistic theory by many years as Klein tunneling and it is probably the most studied effect in graphene[16, 17], and it has been recently seen experimentally in graphene $p-n$ junctions [18, 19]. In non-relativistic quantum mechanics is known that a wave (here an electron) with energy E has a finite probability to penetrate a potential barrier with a height $V_0 < \infty$. For a square barrier of height L this probability is [20]

$$T = \begin{cases} \frac{4E\eta^2}{4E\eta^2 + V_0^2 \sin^2 \eta L} & \text{if } E > V_0 \\ \\ \frac{4E\zeta^2}{4E\zeta^2 + V_0^2 \sinh^2 \zeta L} & \text{if } E < V_0 \end{cases} \tag{1.17}$$

where $\zeta = \sqrt{V_0 - E}$ and $\eta = \sqrt{E - V_0}$. This probability is necessarily lower than one when the channel is closed ($E < V_0$) but eventually is non-zero due to tunneling effect. Then it rises up to total transmission, with some oscillation due to interference effects, when the energy overcome the barrier height.

The result above is obtained by matching of both the wave function and its derivative at the sharp edges of the barrier. When dealing with relativistic particles they do not require derivative continuity, so it turns out that the transmission coefficient is one whichever is the barrier height: also for the paradox case of infinite potentials [1].

The usual interpretations of this effect in quantum field theory is based on particle-antiparticle pairs production at the potential edge, but in graphene this may be understood invoking pseudospin conservation. When a particle impinges on an infinitely high potential barrier it should be reflected back, inverting its momentum component along the barrier's normal direction. The change of the propagation direction would change the sign of its momentum k so, if the particle does not change cone, this implies a pseudospin change. Indeed, in the absence of pseudospin-flip processes (such processes are rare as they require a short-range potential, which would act differently on A and B sites of the graphene lattice) or inter-valley ($\mathbf{K}$-$\mathbf{K}'$) scattering, an electron moving toward right can be scattered

---

[1] In the extension to the two dimensional case this is true for angles close to normal incidence only.

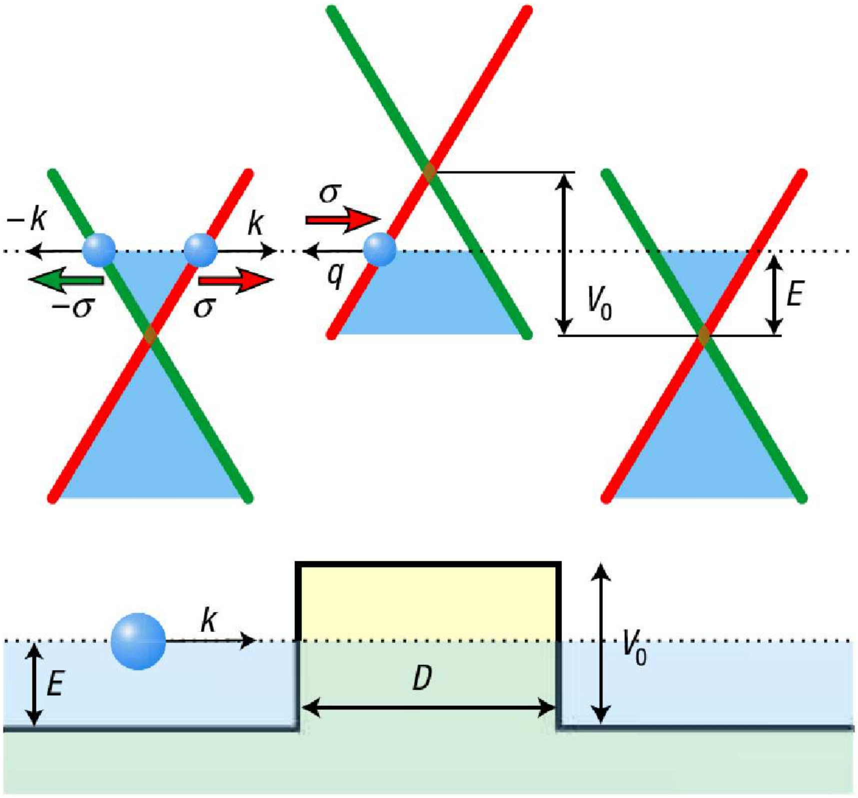

Figure 1.6: A scheme of Klein paradox in graphene, taken from ref.[16]. Because of pseudospin conservation electrons can scatter only into the red band branches, so only in the forward direction giving total transmission.

only to a right-moving electron state or a left-moving hole state. As shown in fig.1.6 an electron with a given group velocity direction k, as in the red branch, can be scattered by the potential difference only in states with the same pseudospin projection, hence into a hole with opposite group velocity and again in the same electron state (red band branch) out from the barrier. Since no fraction of the initial wave packet can scatter back into green branches states without breaking the pseudospin conservation the result is total transmission: infinite barriers are transparent to graphene's electrons [16, 21, 22]. Note that chirality is not conserved here: since electrons turns to be holes in the barrier region. Chirality is a good quantum number only for energies close to the charge neutrality point, so where the Dirac equation is valid. Pseudospin is instead conserved as long as the tight binding Hamiltonian in eq.1.7 is valid.

The second effect known as *Zwitterbewegung*, and it is a rapid wiggling of the

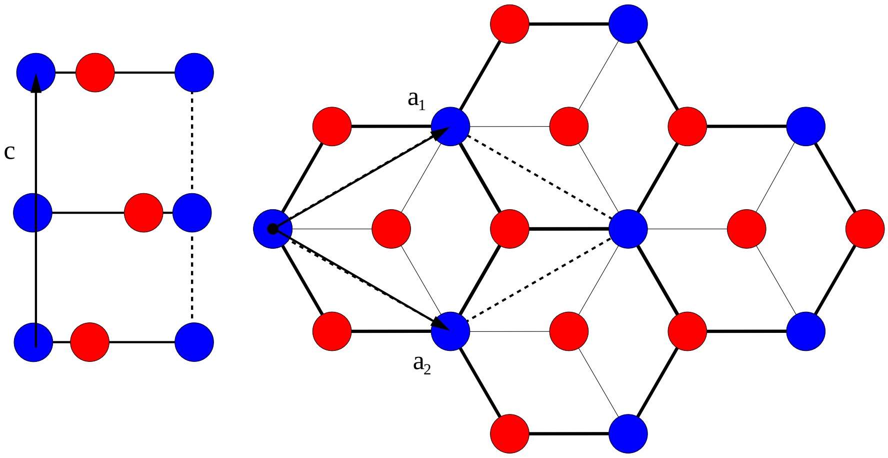

Figure 1.7: Graphite unit cell: the unit vectors lying on the layer are the same as in graphene while the c vector 3.5x Å long normal to them defines the third dimension. In the so-called Bernal structure, the stacking is of AB kind hence the unit cell is made of two layers only.

particle position around its center mass due to the interference of positive- and negative-energy components allowed in the relativistic framework. This jittery motion origin is rather complicated to explain in details, but one can say very briefly that it is a consequences of uncertainty principle for massless Dirac particles. For these relativistic particles the momentum-position uncertainty is also related to the time-energy uncertainty[23]. It can be shown that for every initial state (wave packet) with positive momentum components only this *Zwitterbewegung* effects is absent. Although whenever a potential energy operator acts on it introduces negative energy components: the positive and negative energy components of the wave packet travel in opposite directions giving rise to interference phenomena hence to the jittery motion. This effect should appear when trying to confine the wave function and can be seen in experiments as anomalies in the Shubnikov-de Haas oscillations[24].

1.3 Graphite Lattice and Band Structure

Graphite three-dimensional structure is made of parallel layers of graphene (see fig1.7). The distance between two adjacent graphene layers, $c/2 = 3.35$ Å, is significantly longer than the in-plane bond length of 1.42 Å: this implies a pronounced anisotropy in macroscopic properties such as electric conductivity, optical response and elasticity. Graphite layers are arranged in the so-called Bernal stacking, namely of the ABAB... kind. The atomic positions in one plane are connected to other layers by a roto-reflexion symmetry operation, from this follows that graphite belongs to non-symmorphic group $P6_3/mc$. Its Brillouin zone is of course shaped as a three dimensional hexagonal prism and contains twice the special k points of graphene, now lying at half the prism's height and at its basis. The ABAB stacking sequence of the layers produces two different kind of carbon sites on the surface: one that have a carbon in the same position and another that lays in the middle of an hexagonal ring of the graphene layer immediately below the surface (i.e. along the $\{000\bar{1}\}$ crystallographic direction).

The stacking arrangement turns to be very important for the electronic structure [25, 26], and in the limit of a totally disordered situation (turbostatic graphite) each layer is totally decoupled from the others hence it behaves as graphene[27]. The interaction between carbon atoms that are nearest neighbours in different layers breaks the sublattices symmetry of graphene destroying the Dirac cones. A useful example of this effect is the band structure of graphene bilayer. Here there are four different sublattices that within the same tight binding approximation used in section 1.2 show two quasi-conical bands touching at the Fermi energy. This can be interpreted still as pseudo-relativistic fermions but with a non zero mass. In three-dimensional graphite the band structure is non-linear at the Fermi energy: its density of states is still zero at the Fermi energy making it a classical semi-metallic system [28].

The layers are weakly bonded to each other by van der Waals forces, so are easily cleavable to expose the $\{0001\}$ surface, also known as basal plane. The van der Waals force comes from a quantum fluctuation in one graphene layer that generates an instantaneous electric dipole moment. The moment induces another electric dipole on the neighbouring layer, proportional the electric polarizability of the latter and the dipole-dipole attraction keeps the graphene planes together. This quantum fluctuation can arise because of correlation of electron density oscillations: if the fluctuations were statistically independent the interaction energy would vanish after integrating over the whole space. Because of they origin from electron correlation the strength of the interlayer forces is weak compared to the in-plane ones that form σ and π bonds, based on orbital overlap. For this reason the "chemical" behaviour of graphite, that usually involve interactions in the order of tenths of an electronvolt, should not be significantly affected by the van

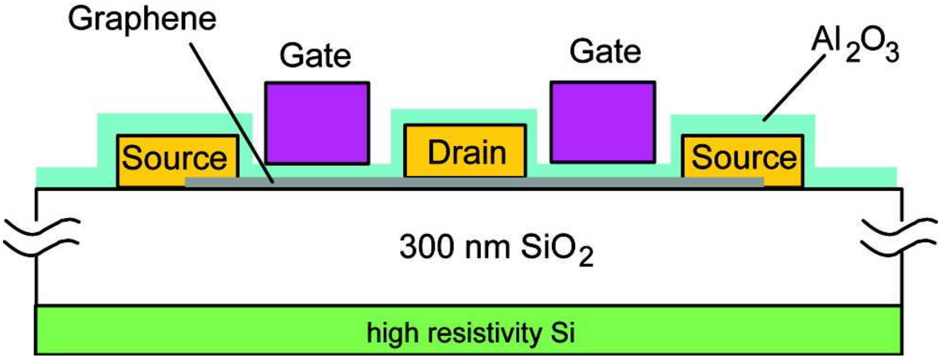

Figure 1.8: Scheme of a single-layer graphene Field Effect Transistor (FET) recently realized by Avouris *et al.*[32]

der Waals force, so should not be much chemically different form graphene that can be considered as a good approximation of graphite {0001} surface.

1.4 Technological Application of Graphene

Graphene looks a very promising material for novel electronic devices in fact, due to its semi-metallic character, the charge carriers can be continuously tuned from electrons to holes. Recent transport experiments showed that graphene has an extraordinary electron mobility up to room temperature, with reported values of 15000 $cm^2V^{-1}s^{-1}$ and higher [8, 29, 30]: mobility is nearly independent of temperature between 10 K and 100 K, moreover this holds up to very high charge carriers concentrations. This phenomena are consequences of ballistic transport, possible very low number of defects in graphene samples allows mean free paths for electrons in the sub-micrometers scale. The temperature independence of mobility suggests that the main scattering mechanism for charge carriers in graphene is due to impurities and not to the phononic motion. An intrinsic limit to electron mobility of around 2 10^5 $cm^2V^{-1}s^{-1}$ is indeed given by scattering with acoustic phonons, nevertheless this correspond to the lowest resistivity known at room temperature [31]. Based on this results graphene based devices such as the transistor in fig.1.8 have been produced and they show excellent performances [32].

The presence of Dirac cones drives graphene's density of states to zero at the Fermi energy. This means that without any doping the charge carriers density is zero at zero temperature, hence that conductivity should be completely turned off at low temperatures as in traditional semiconductors. Strangely, it has been reported [29] a non-zero minimal conductivity whose origin is still debated [33, 34, 35, 36]. The lacking of a real band gap is a serious problem for the design of a graphene-based ballistic field effect transistor that needs a high on/off ratio, *i.e.* an absence of conduction within a given range of applied source/drain potential. For this reason several attempts to open a band gap in graphene are currently under study. They can be divided in two main classes: methods based on electron confinement and on the breaking of the sublattices symmetry. The first class consists in confining the wave function to a finite spatial area such as cutting out from graphene a *nanoribbon*[37, 38, 39], or using adsorbates to induce electron scattering[40]. The latter instead removes the degeneracy at the Fermi level by removing some symmetry elements of the lattice: this is what happens for instance when a graphene lays on a supporting surface that interacts with some carbon atoms only such as on silicon carbide [41, 42, 43, 44].

Another approach to a graphene electronics is to consider graphene as a conductor material to carve for producing single electron transistor circuits. In this way one might design circuits with components dimensions down to a benzene ring width. Recently it has been shown how arrays of holes dug on graphene can behave as quantum dots structures. Ordinary techniques would require growth and controlled etching of semiconductors layers, while in this case nano-lithographic technique may be easily produce such holes [45, 46, 47].

Many other applications have been so far proposed for graphene, ranging from gas sensors [48] to electron lenses [49] and liquid crystal devices[50]: for a more exhaustive list of them the reader is encouraged to see recent reviews such as [51, 13]

1.5 The Importance of the Hydrogen-Graphite Surface Interaction

1.5.1 Graphite for Energy Applications

Nuclear fusion is a highly exothermic process that naturally occurs in stars and that produces energy in a clean and efficient way. The nuclear reaction that is actually under study for the production of a test reactor is the one between a deuterium nucleus that tunnels into tritium producing helium nucleus (α particles) and neutrons at 14 MeV. The reaction occurs only at very high collision

energies (few keV) where the hydrogen isotopes are in a plasma state, confined by strong magnetic fields, usually in toroidal reactors known as tokamak.
Other than nuclear fusion many other reactions can take place in the plasma. Those which produce neutral species are particularly undesirable since these are not confined by the magnetic field and tend to escape from the plasma. The main neutral side-product in fusion reactors are hydrogen atoms. These can travel to the reaction vessel and erode its walls: this pollutes the plasma causing its cooling down to temperatures in which fusion reactions cannot occur. Plasma cooling efficiency is proportional to the pollutant atomic mass, for this reason the reactor walls are usually covered by graphite: a good and light thermal insulator. Still, the hydrogen atoms impinging on graphite can recombine, induce vacancies, phase transitions to diamond, etc. The hydrogen atoms - graphite surface interaction is then important in this framework in order to design better reactor walls coatings [52].

Another possible use of hydrogen in energy applications is its combustion in engines for the automotive industry. In the oxidation reaction to form water hydrogen can be used as an energy vector with a low environmental impact. In an hypothetical hydrogen propelled internal combustion engine, the efficiency will necessarily be limited by the Carnot's cycle, so comparable to fossil fuels. However the same chemical reaction can occur in an electrochemical cell: a fuel cell, where the yield can be as high as 60 percent.
In this perspective the oxygen source can directly be air, but one problem to deal with is the storage of hydrogen. To liquefy hydrogen is a rather expensive process and it would still take a considerable volume. It has been computed that to provide a car with 400 km of range around 225 liters of liquid hydrogen would be needed [53]. Then, a large effort has been made to find a suitable solid material for hydrogen storage, and current research is working mostly on light metals hydrides such as alanates, amides, *etc.*[54, 55] and also on carbon based materials. While for hydrides it is necessary to find a *reversible* chemical reaction that can make a material release hydrogen upon heating, for carbon based materials is it necessary to modify their natural adsorption properties. This means either to enhance the weak H_2 physisorption interaction or to destabilize the strong hydrogen atom chemisorption to tailor the adsorption energy to the best temperature range. Among carbon materials the best candidates so far are

high surface area graphites or nanotubes doped with alkali on which hydrogen molecules can bind, although the target hydrogen weight percent established by the American department of energy are still quite far, so a better understanding of this interaction might also help in optimizing hydrogen storage materials.

1.5.2 Graphite in the Interstellar Medium

The Interstellar medium (ISM) is that region made of rarefied matter that fills the space between stars. Within the ISM is possible to distinguish several regions that differ by temperature, density and chemical composition. Important environments for the chemistry of ISM are the *clouds*, regions made of gas and dust classified in dense and diffuse clouds. Diffuse clouds are rather harsh environments. They have a density of about 10^2 cm^{-3} and temperatures in the range of 10 to 100 K. Stellar radiation is here usually sufficient to ionize most of the chemical species that compose the gas, giving rise to an active network of ionic reactions. The molecular products of these reactions are often quickly photo-dissociated, while small dust grains made of carbonaceous particles or even just of polycyclic aromatic hydrocarbons (PAH), can survive thanks to their high density of states that prevents internal conversion an so dissociation. Dense clouds are instead much denser (10^4 cm^{-3}) and contain more dust. This is sufficient to extinguish stellar radiation, hence to shield molecular species from UV radiation, and to support the synthesis of more complex molecules [56, 57, 58, 59].

The dynamics of the clouds is of paramount importance in astrophysics: clouds are born from the matter ejected from the dying stars they surround, and grow in this way increasing their density, from diffuse to dense clouds. Increasing in mass the cloud starts to collapse onto itself due to the gravitational pull that at some point should be balanced by the internal gas pressure reaching a steady state. Surprisingly this does not happen, probably because the molecular species that compose the cloud are rotationally excited by collisions (pressure) and then, if the pressure is not high enough to have frequent collisions, they relax emitting photons. This radiative cooling process allows the collapse to continue until pressure and temperature are large enough for nuclear reactions to ignite and new stars form at the center of the cloud. To understand this star forming cycle it is necessary to know which processes occur in the cloud at each stage, hence for different temperature and pressure values.

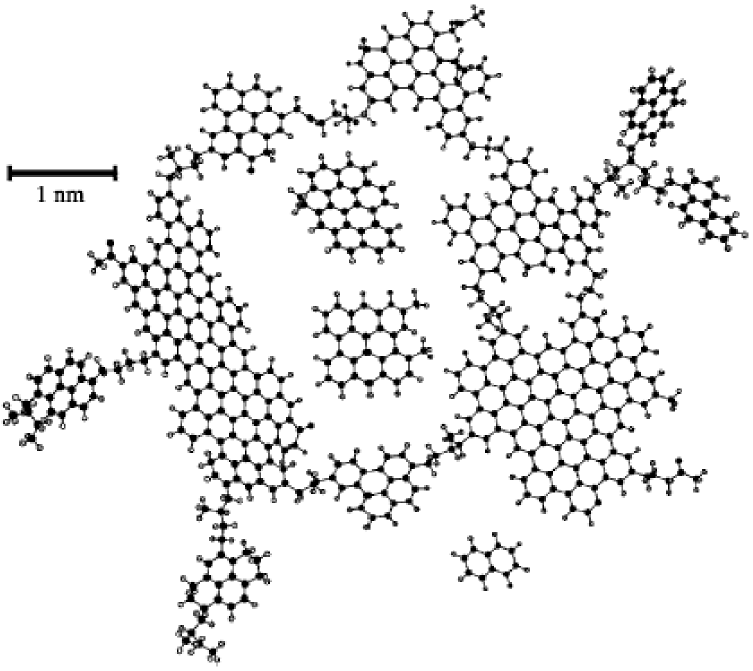

Figure 1.9: A model for the typical dust grain of diffuse clouds in the interstellar medium: mostly made by large areas of polycyclic aromatic hydrocarbons connected together. picture from ref.[60]

$$\mathrm{H} + \mathrm{H} \rightarrow \mathrm{H}_2 + \gamma \tag{1.18}$$

The most abundant molecule in dense clouds is molecular hydrogen. Although its efficiency in radiative cooling is rather low, its concentration is so high that H_2 contribution has to be fundamental for the overall process. For this reason hydrogen formation in clouds is the object of intense research. In the gas phase H_2 can be produced by several reactions and, in particular *via* radiative association: the direct formation in which reaction exothermicity is dissipated trough photon emission. This mechanism is very common in the ISM, since the extremely low pressure, and it is quite efficient. Unfortunately this cannot be the case for H_2 since the reaction cross section is proportional to the product molecule dipole moment. This means that there should be another efficient pathway for molecular hydrogen production in interstellar clouds.

It has been proposed [61, 62] that atomic recombination occurs on the surface of dust grains, that should act as a catalyst for H_2 production [63, 60]. Dust grains in diffuse clouds are generally very small and mostly made of large PAH, as shown in fig.1.9, while in dense clouds PAH are embedded in a carbonaceous shell covered in ices that surrounds a silicate core. Hydrogen atoms might then recombine on this graphite like surface following the classical mechanisms of surface reactions, namely the Eley-Rideal or Langmuir-Hinshelwood mechanisms.

Chapter 2

Fundamentals of Density Functional Theory

Density functional theory (DFT) is a theoretical approach to electronic structure that is becoming a standard in condensed matter and materials physics. It made feasible to obtain total energies, physical properties and relaxed geometries of solids and molecules up to hundreds of atoms. Most of the work presented in this thesis has been done with the help of this technique. In particular DFT have been used to compute chemisorption energies of hydrogen atoms on graphene and graphite, and to build of potential energy surfaces for the study of Eley-Rideal recombination dynamics of H_2 molecules on dust grains.

In this chapter we will introduce the theoretical framework of DFT, starting from density matrices, their correspondence to wave functions and the definition of the electron density. The possibility to get the total energy as a functional of the electron density, is traditionally shown through the Hohenberg-Kohn theorems. Although very didactic they have some pitfalls: for this reason we shall introduce first the Levy constrained search and from it retrieve the theorems results in order to present a more general theoretical framework. Then, we will state the Kohn - Sham equations, that are in fact the way to the solution of the electronic structure problem. Moreover we will present some other important theoretical tools, that have been fundamental in computing the gas-surface interaction, such as the Hellmann - Feynman forces and the plane wave approach for applying DFT to periodical system, being them either bulk solids or surfaces.

2.1 Density Matrix Formalism

The density operator for a pure state is usually defined as:

$$\hat{\rho} = |\Psi\rangle \langle\Psi| \tag{2.1}$$

where $|\Psi\rangle$ is the physical system's wave function and it is most known in its matrix form, once introduced a basis set. The density matrix is a very useful tool used to define a physical system in an univocal way. In fact for every system one has an infinite set of wavefunctions $\{\Psi(\mathbf{r})\}$ differing only for a complex phase factor $e^{i\phi}$, but in building the ρ matrix such phases are factored out and so for every system there exists only one density matrix with unitary trace

$$\hat{\rho} = e^{i\phi} |\Psi\rangle \langle\Psi| e^{-i\phi} = |\Psi\rangle \langle\Psi|$$

Here the system is composed by the quantum state $|\Psi\rangle$ alone, hence is a so-called *pure state*. For pure states the density operator reduces to a projector on the subspace $\mathcal{S} \subseteq \mathcal{H}$ spanned by the state $|\Psi\rangle$ itself

$$\hat{\rho}\,|f\rangle = |\Psi\rangle \langle\Psi|f\rangle = f(\Psi)\,|\Psi\rangle \tag{2.2}$$

and of course are valid its projector properties: idempotency and self-adjointness

$$\langle n|\hat{\rho}^2|n\rangle = \langle n|\Psi\rangle \langle\Psi|\Psi\rangle \langle\Psi|n\rangle = \langle n|\hat{\rho}|n\rangle \tag{2.3}$$

$$\Rightarrow \hat{\rho}^2 = \hat{\rho}^\dagger = \hat{\rho} \tag{2.4}$$

Its trace, independent on the basis, is one for normalized state vectors $|\Psi\rangle$

$$\mathrm{Tr}\hat{\rho} = \sum_n \langle n|\Psi\rangle \langle\Psi|n\rangle = \int \Psi_n^*(\mathbf{r})\Psi_n(\mathbf{r})d\mathbf{r} = 1 \tag{2.5}$$

and in the same way one obtains

$$\mathrm{Tr}\rho^2 = 1 \tag{2.6}$$

So, a density operator describes a pure state if it is a rank one projection operator (an elementary projector), so we may conclude that formally speaking a density operator is a positive semi definite, unitary trace hermitian operator acting on the states space.

If the physical system is not in a pure state but in a *statistical mixture* of quantum states then it has a probability $p_1, p_2, ...$ of being in the state $|\Psi_1\rangle, |\Psi_2\rangle, ...$ respectively. Its density matrix has the form

$$\hat{\rho} = \sum_i p_i \left|\Psi_i\right\rangle \left\langle\Psi_i\right| \tag{2.7}$$

where $p_i \in [0,1]$ are the statistical weights of each state $\left|\Psi_i\right\rangle$ not necessarily orthogonal to each other. The unity of trace is still granted by the normalization of probability[1]

$$\mathrm{Tr}\rho = \sum_{in} p_i \left\langle n|\Psi\right\rangle \left\langle\Psi|n\right\rangle = \tag{2.8}$$

$$= \sum_{in} p_i \left\langle\Psi|n\right\rangle \left\langle n|\Psi\right\rangle = \sum_i p_i = 1 \tag{2.9}$$

and, while $\hat{\rho}$ remains self-adjoint, its idempotency is no more valid

$$\hat{\rho}^2 = \sum_i p_i \left|\Psi_i\right\rangle \left\langle\Psi_i\right| \hat{\rho} = \tag{2.10}$$

$$= \sum_{ij} p_i p_j \left|\Psi_i\right\rangle \left\langle\Psi_i|\Psi_j\right\rangle \left\langle\Psi_j\right| = \tag{2.11}$$

$$= \sum_{ij} p_i p_j \left|\Psi_i\right\rangle \delta_{ij} \left\langle\Psi_j\right| = \sum_i p_i^2 \left|\Psi_i\right\rangle \left\langle\Psi_i\right| \tag{2.12}$$

$$\Rightarrow \begin{cases} \hat{\rho}^2 = \hat{\rho} & \left|\Psi_i\right\rangle = \left|\Psi_j\right\rangle \\ \hat{\rho}^2 \neq \hat{\rho} & \left|\Psi_i\right\rangle \neq \left|\Psi_j\right\rangle \end{cases} \tag{2.13}$$

In the same way the ρ^2 trace is less than 1 if there is a $p_i \neq 0$ for more than one state $\left|\Psi_i\right\rangle$

$$\mathrm{Tr}\hat{\rho}^2 = \sum_n \left\langle n|\hat{\rho}^2|n\right\rangle = \sum_n \sum_i p_i \left\langle n|\Psi_i\right\rangle \rho \left\langle\Psi_i|n\right\rangle = \tag{2.14}$$

$$= \sum_n \sum_{ij} p_i p_j \left\langle n|\Psi_i\right\rangle \left\langle\Psi_i|\Psi_j\right\rangle \left\langle\Psi_j|n\right\rangle = \tag{2.15}$$

$$= \sum_n \sum_{ij} p_i p_j \left\langle\Psi_i|\Psi_j\right\rangle \left\langle\Psi_j|n\right\rangle \left\langle n|\Psi_i\right\rangle = \sum_i p_i^2 \left|\left\langle\Psi_j|\Psi_i\right\rangle\right|^2 \tag{2.16}$$

$$\Rightarrow \begin{cases} \mathrm{Tr}\hat{\rho}^2 = 1 & \left|\Psi_i\right\rangle = \left|\Psi_j\right\rangle \\ \\ 0 \leq \mathrm{Tr}\hat{\rho}^2 < 1 & \left|\Psi_i\right\rangle \neq \left|\Psi_j\right\rangle \end{cases} \tag{2.17}$$

So the idempotency condition is necessary and sufficient to identify a physical system as a pure state.

---

[1] Note that here the trace is defined on the Fock space, hence on states with different particle number. All the trace properties (semi-positivity, invariance under cyclic permutations,...) are conserved but formally the two operations are defined on different spaces.

We introduce now a representation of the density operator by using a basis such as

$$\{\Psi_n\}: \qquad \rho_{nm} = \langle \Psi_n | \rho | \Psi_m \rangle \tag{2.18}$$

$$\{x_i\}: \qquad \rho(x, x') = \langle x | \rho | x' \rangle \tag{2.19}$$

Using this definition the expectation values of a generic observable A are the following:

$$\langle A \rangle = \sum_i p_i \langle \Psi_i | A | \Psi_i \rangle \tag{2.20}$$

and any of them can be obtained directly from the density matrix simply by tracing

$$\langle A \rangle = \sum_{i,n} p_i \langle \Psi_i | A | \Psi_n \rangle \langle \Psi_n | \Psi_i \rangle = \sum_{i,m} p_i \langle \Psi_n | \Psi_i \rangle \langle \Psi_i | A | \Psi_n \rangle = \tag{2.21}$$

$$= \sum_n \langle \Psi_n | \rho A | \Psi_n \rangle = \mathrm{Tr}(\rho A) \tag{2.22}$$

From all the properties stated above one may conclude that the density matrix ρ is a matrix with the dimension of the number of system's degrees of freedom and contains *all* the information (observables) on the physical system.

A more compact form is the *reduced density matrix*, given from the trace (integration) of some degrees of freedom

$$\rho_{(p)}(x_1, .., x_p, x'_1, .., x'_p) = \tag{2.23}$$

$$= \begin{pmatrix} N \\ p \end{pmatrix} \int \Psi(x_1, .., x_p, x_{p+1}, .., x_n) \Psi^*(x'_1, .., x'_p, x_{p+1}, .., x_n) dx_{p+1}, .., dx_n \tag{2.24}$$

where p is the *order* of the reduced matrix and the binomial coefficient rises from particles indistinguishably. These matrices are still hermitian and corresponds to semipositive defined self-adjoint operators. Their spectrum is discrete *i.e.*

$$\hat{\rho}_{(p)} |\gamma_n\rangle = \gamma_n |\gamma_n\rangle \tag{2.25}$$

and the eigenfunctions $|\gamma_n\rangle$ are known as natural functions. In particular for first order density matrices are known as natural orbitals and for second order as natural geminals, while eigenvalues γ_n are their occupation numbers.

Reduced density matrices may be used as the wave functions in evaluating physical properties. Between the different reduced density matrices the most widely used are the first and second order ones from which one can retrieve information on one- and two-electron operators' observables

$$\rho(\mathbf{x'}_1, \mathbf{x}_1) = N \int \Psi(x_1, .., x_n)\Psi^*(x'_1, .., x_n) dx_2, .., dx_n \tag{2.26}$$

$$\rho(\mathbf{x'}_1\mathbf{x'}_2, \mathbf{x}_1, \mathbf{x}_2) = \frac{N(N-1)}{N} \int \Psi(x_1, .., x_n)\Psi^*(x'_1, .., x_n) dx_3, .., dx_n \tag{2.27}$$

normalized respectively to the number of electrons and to the number of electron pairs

$$\mathrm{Tr}\rho(\mathbf{x'}_1, \mathbf{x}_1) = N \qquad \mathrm{Tr}\rho(\mathbf{x'}_1\mathbf{x'}_2, \mathbf{x}_1, \mathbf{x}_2) = \tfrac{N(N-1)}{N} \tag{2.28}$$

One of the most important examples is the expectation value for a simple hamiltonian

$$H = \frac{e^2}{2}\sum_{ij}\frac{Z_iZ_j}{r_{ij}} + \sum_i\left(\frac{p_i^2}{2m} - e^2\sum_j\frac{Z_j}{r_{ij}}\right) + \sum_{ij}\frac{e^2}{r_{ij}} \tag{2.29}$$

$$E = \frac{e^2}{2}\sum_{ij}\frac{Z_iZ_j}{r_{ij}} + \frac{1}{2m}\int p_1^2\rho(\mathbf{x}_1, \mathbf{x'}_1)dx_1 - \tag{2.30}$$

$$-e^2\sum_i Z_i\int\frac{\rho(\mathbf{x}_1, \mathbf{x}_1)}{r_{1i}}dx_1 + e^2\int\frac{\rho(\mathbf{x}_1\mathbf{x}_2, \mathbf{x}_1, \mathbf{x}_2)}{r_{12}}dx_1dx_2 \tag{2.31}$$

Note that for a fermionic system, the wave function must be antisymmetric due to Pauli principle. In this way the corresponding reduced density matrices must reflect this property i.e.

$$\rho(\mathbf{x'}_1\mathbf{x'}_2, \mathbf{x}_1, \mathbf{x}_2) = -\rho(\mathbf{x'}_2\mathbf{x'}_1, \mathbf{x}_1, \mathbf{x}_2) \tag{2.32}$$

$$\rho(\mathbf{x'}_1\mathbf{x'}_2, \mathbf{x}_1, \mathbf{x}_2) = -\rho(\mathbf{x'}_1\mathbf{x'}_2, \mathbf{x}_2, \mathbf{x}_1) \tag{2.33}$$

this implies that

$$\rho(\mathbf{x'}_1\mathbf{x'}_2, \mathbf{x}_1, \mathbf{x}_2) = 0 \quad \text{if} \quad \mathbf{x}_1 = \mathbf{x}_2 \text{ or } \mathbf{x'}_1 = \mathbf{x'}_2 \tag{2.34}$$

This is due to the repulsion between electrons with the same spin and give rise to the so called *Fermi correlation hole*: that represents the probability of finding two fermions in a given points in space as a function of their separation. This function has, as expected, a global minimum that reaches zero if the spatial distance between two electrons with the same spin is null.

2.2 The Levy Costrained Search

For a given physical system made of N_e electrons it exists an Hamiltonian, defined by the potential field in which they are embedded

$$\hat{H} = \hat{T} + \hat{V}_{ext} + \hat{V}_{ee} \tag{2.35}$$

here $\hat{V}_{ext} = v_{ext}(\mathbf{r})\cdot$ is the (*local*) external potential field generated by nuclei and $\hat{V}_{ee}$ the *full* electron-electron interaction operator. The system total energy is the matrix element of the Hamiltonian on a given basis set, namely a functional of the wave function

$$\hat{H}\left|\Psi\right\rangle = E\left|\Psi\right\rangle \tag{2.36}$$

$$E[\Psi] = \langle\Psi|\hat{H}|\Psi\rangle \tag{2.37}$$

Usually, both in electronic structure and dynamics, the system's description is based on the wave function Ψ. From the Schrödinger's equation it is known that Ψ contains all the information needed, hence all the *observables* as eigenvalues of an operator acting on the wave function. Nevertheless, $\Psi(\mathbf{r})$ is a very large function. It is indeed a function of a spatial coordinate $\mathbf{r}$, so three degrees of freedom $\{x, y, z\}$, and a spin index for every nuclei and every electron. In this way the system coordinates grows very fast with the number of electrons. For the simple H_2 molecule the electronic $\Psi(\mathbf{r})$ has already 8 degrees of freedom, and so for larger molecules this object will become very soon too large to be handled computationally.

The use of the density matrix in place of the wave function is possible, since it still contains all the information of the system, but not much easier. So the need of a method based on some smaller representation of $\Psi(\mathbf{r})$ started to rise rather soon in the history of quantum chemistry.

Being interested in the *ground* state energy and noting that its electron density ρ_0 is connected to both the ground state wave function Ψ_0 trough

$$E[\rho_0] = \langle\Psi_0|\hat{H}|\Psi_0\rangle = \mathrm{Tr}(\rho_0 H) \tag{2.38}$$

is then possible to think about a theory that aims to the total energy of an electronic system directly from its density $\rho_0(\mathbf{r})$. This approach can be seen as related to the density matrix of the system, being the electronic density the collection of diagonal elements of the first order reduced density matrix.

$$\rho(\mathbf{r}) = \rho_1(\mathbf{x}_1, \mathbf{x}_1) \tag{2.39}$$

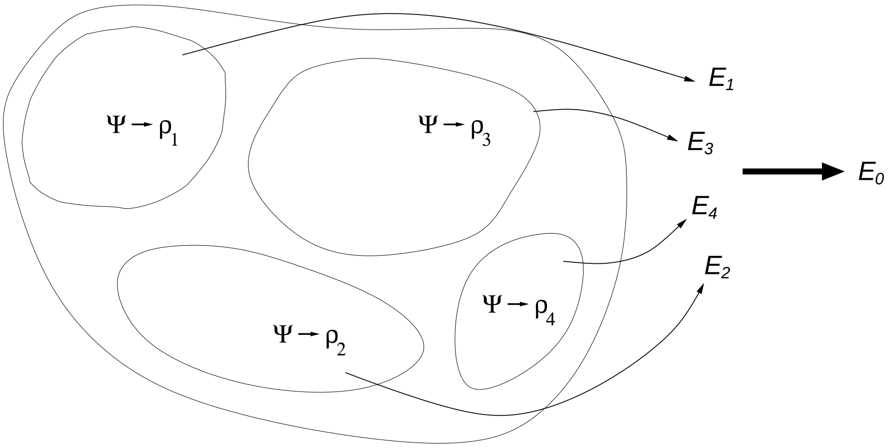

Figure 2.1: Pictorial view of the Levy constrained search. The space of ground state wave function is first partitioned according to the electron densities they generates, then the variational search is done in two steps: first over the wavefunctions, then over the densities. See text.

Moreover, despite the natural loss of information due to the integration on all but one degree of freedom of the full density matrix, the electron density is always a purely three dimensional function, so much easier to handle computationally on numerical grids.

In order to build an electronic structure method based upon the electron density is first necessary to establish a variational principle. From the Rayleigh-Ritz variational principle to find the system's ground state energy is sufficient to search the wave function that minimizes the Hamiltonian expectation value

$$E_0[\Psi] = \min_{\Psi} \langle \Psi | H | \Psi \rangle \tag{2.40}$$

where the wave functions have to be anti-symmetric and fulfill the appropriate boundary conditions. This procedure can be divided in two steps. First the space of the Ψ is partitioned into subsets of wave functions that give by quadrature the same electron density $\rho(\mathbf{r})$ and constrain the search for the minimum energy in this subset only

$$E_\rho[\rho] = \min_{\Psi \to \rho} \langle \Psi | \, \hat{H} \, | \Psi \rangle = \min_{\Psi \to \rho} \langle \Psi | \, T + \widehat{V_{ee}} + V_{ext} \, | \Psi \rangle \tag{2.41}$$

$$= \min_{\Psi \to \rho} \langle \Psi | \, \hat{T} + \hat{V}_{ee} \, | \Psi \rangle + \int v_{ext}(\mathbf{r}) \rho(\mathbf{r}) d\mathbf{r} = \tag{2.42}$$

$$= F[\rho] + \int v_{ext}(\mathbf{r}) \rho(\mathbf{r}) d\mathbf{r} \tag{2.43}$$

where it has been introduced a *universal* functional $F[\rho]$

$$F[\rho] = \min_{\Psi \to \rho} \langle \Psi | \hat{T} + \hat{V}_{ee} | \Psi \rangle \tag{2.44}$$

The universal functional contains the electron-electron interaction only that is independent from the external potential but unique for every physical system. Once obtained the variational energy for a given ρ, so the functional $E_\rho[\rho]$, in order to complete the search one minimizes the energy with respect to the densities that integrates to N electrons

$$E_0 = \min_\rho E_\rho = \min_\rho \left\{ F[\rho] + \int v_{ext}(\mathbf{r})\rho(\mathbf{r})d\mathbf{r} \right\} \tag{2.45}$$

This variational principle can also be written as a Lagrange multipliers problem

$$\delta \left\{ E[\rho] - \mu \left[\int \rho(\mathbf{r})d\mathbf{r} - N \right] \right\} = 0 \tag{2.46}$$

$$\frac{\delta E[\rho(\mathbf{r})]}{\delta \rho} - \mu = 0 \tag{2.47}$$

and using eq.2.44 one gets the final Euler-Lagrange equation

$$\frac{\delta F[\rho(\mathbf{r})]}{\delta \rho} + v_{ext}(\mathbf{r}) = \mu \tag{2.48}$$

where the multiplier μ is the chemical potential and the constrain in the minimization is the total number of electrons N.
This procedure is known as the Levy constrained search (also pictorially represented in fig.2.1) and it defines immediately a variational principle based upon the electron density equivalent to the Rayleigh-Ritz one, results also known as the second Hohenberg-Kohn theorem.

$$E_0 = \min_\rho E_\rho = \min_\rho \left\{ F[\rho] + \int v_{ext}(\mathbf{r})\rho(\mathbf{r})d\mathbf{r} \right\} = \tag{2.49}$$

$$= \min_\rho \left\{ \min_{\Psi \to \rho} \langle \Psi | \hat{T} + \hat{V}_{ee} | \Psi \rangle + \int v_{ext}(\mathbf{r})\rho(\mathbf{r})d\mathbf{r} \right\} = \tag{2.50}$$

$$= \min_\rho \left\{ \min_{\Psi \to \rho} \langle \Psi | H | \Psi \rangle \right\} = \min_\Psi \langle \Psi | H | \Psi \rangle \tag{2.51}$$

For a theory based on the electron density is also necessary to make sure that a given ρ corresponds to only one physical system, hence to show that two different v_{ext} will never give the same $\rho(\mathbf{r})$. This is not trivial, since a given potential can

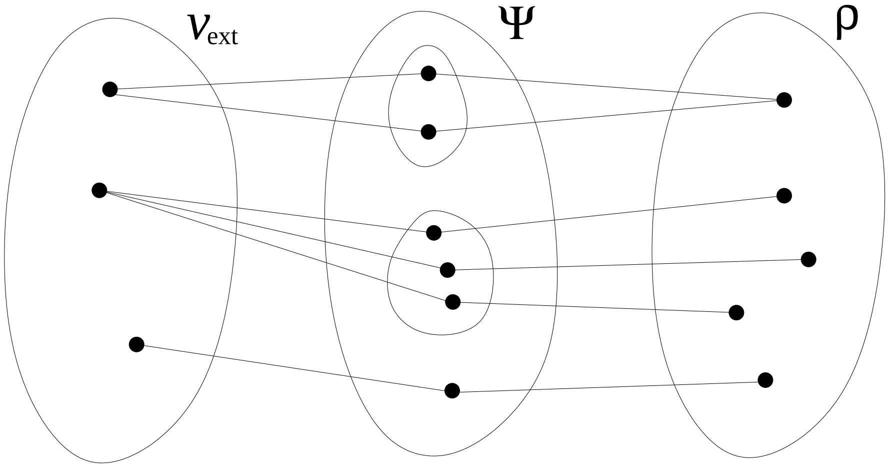

Figure 2.2: A scheme representing the first Hohenberg-Kohn theorem. Although a local potential can have many different ground-state densities, two different potentials cannot give the same ground state density.

generate many wave functions, hence multiple densities, as shown in fig.2.2. In order to show this by *reductio ab absurdo* let suppose that two external potentials $v_{ext}(\mathbf{r})$ and $v'_{ext}(\mathbf{r})$ that differ by more than a constant scale factor, give the same electron density $\rho(\mathbf{r})$. It is then possible to write two separate Euler-Lagrange equations as in eq.2.48

$$\frac{\delta F[\rho(\mathbf{r})]}{\delta \rho} + v_{ext}(\mathbf{r}) = \mu \tag{2.52}$$

$$\frac{\delta F[\rho(\mathbf{r})]}{\delta \rho} + v'_{ext}(\mathbf{r}) = \mu' \tag{2.53}$$

Now, by subtracting the two equations term by term one gets

$$v_{ext}(\mathbf{r}) - v'_{ext}(\mathbf{r}) = \mu - \mu' \tag{2.54}$$

hence, the two potentials can at most only differ by a multiplicative constant, contradicting the initial statement. This result is known as the first Hohenberg-Kohn theorem and connects univocally an external potential with an electron density. Note that this approach holds also in case of degenerate ground state wave functions.

Summarizing, the Hohenberg-Kohn theorems state that electron density determines the positions of the nuclei in a system, and also all ground state electronic properties, because $v_{ext}(\mathbf{r})$ and N completely define $\hat{H}$. In particular the ground state electron density can be obtained variationally form $\rho(\mathbf{r})$.

2.2.1 v- and N- Representability Problem

The set of all the possible electron densities has to be chosen carefully. Indeed to every three-dimensional positive functions can be the ground state density of a physical system. As a very simple example is sufficient to take a cube: this obviously does not correspond to any nuclear arrangement, hence to any external potential. This problem is known as v-representability and it is particularly difficult to solve from a mathematical point of view. However, the constrained search approach overcomes this issue since by construction the universal functional $F[\rho]$ of eq.2.44 is v-representable because it results from a minimization over a set of wave functions, that originate from an Hamiltonian. The problem is not fully solved since, during the minimization over the densities, one should choose only the ρ that come from an antisymmetric N-electron wave functions without any explicit connection to an external potential. This issue is the so called N-representability, well known problem in density matrix theory. At the practical act the constrained search should be limited only to N-representable densities, a condition much weaker than v-representability.

2.3 The Kohn-Sham Scheme

Once a connection between the electron density and the Hamiltonian has been established through the Hohenberg-Kohn theorems, an efficient scheme to compute $E_0[\rho]$ is needed. All the machinery introduced in section 2.2 is not very useful in practice since the electron-electron interaction, included in the potential $\hat{V}_{ee}$ and in the kinetic term, is not explicitly known. The Kohn-Sham scheme introduces in fact another physical problem in such a way that the kinetic energy can be computed simply, leaving all the differences with the true Hamiltonian to a corrective term.

The Kohn-Sham *ansatz* assumes that for every physical system of interacting particles exists a dummy *auxiliary* system of non-interacting particles and that they share the same electron density. If so, following sec.2.2, in order compute the ground state energy one can work on of the auxiliary system: in this case the appropriate functionals are known and easy to compute. Later is possible to add a parametric term that accounts for the many-body effects to retrieve the "real" physical system's energy. The many-body term can be either empirical or obtained from physical reasoning (*first principles*), but nothing prevents to design it fully *local* in a way to simplify dramatically the computational cost.

The Kohn-Sham (KS) functional contains a non-interacting universal functional $F_s[\rho]$ and the effective potential $v_s(\mathbf{r})$

$$E_{KS}[\rho] = F_s[\rho] + \int \rho(\mathbf{r}) v_s(\mathbf{r}) d\mathbf{r} \tag{2.55}$$

$$F_s[\rho] = T_s[\rho] + J[\rho] \tag{2.56}$$

The correction to electronic interaction is included within v_s by the *exchange and correlation* functional that includes all the non-classical terms: exchange, correlation and the kinetic energy induced by this two contributions.

$$E_{KS}[\rho] = F_s[\rho] + E_{xc}[\rho] + \int \rho(\mathbf{r}) v_{ext}(\mathbf{r}) d\mathbf{r} \tag{2.57}$$

$$E_{xc}[\rho] = (T[\rho] - T_s[\rho]) + E_x[\rho] + E_c[\rho] \tag{2.58}$$

Of the terms in eq.2.56 and eq.2.58, only $J[\rho]$ is known, while the explicit forms of the other contributions remain unknown. In particular $T[\rho] - T_s[\rho]$ is the interaction contribution to the kinetic energy: a term also known as *dynamical* correlation.

A good exchange and correlation functional is crucial in order to have a good approximation to the ground state energy. They might be local or not, obtained from benchmark *ab initio* calculations or from first principles, etc. and their design is an active research field.

2.3.1 The Kohn-Sham Equations

Now we shall derive the practical equations used to obtain the total ground state energy. Fist we have to choose a trial wave function as close as possible to the non-interacting system's one. This is indeed an easy task since it is known that this kind of physical systems are exactly represented by a wave function that is the antisymmetrized product of single particle orbitals (a Slater determinant)

$$\Psi(\mathbf{r}_1, \ldots, \mathbf{r}_N) = \frac{1}{\sqrt{N!}} \det \begin{pmatrix} \phi_1(\mathbf{r}_1) & \ldots & \phi_N(\mathbf{r}_1) \\ \vdots & \ddots & \vdots \\ \phi_1(\mathbf{r}_N) & \ldots & \phi_N(\mathbf{r}_N) \end{pmatrix} \tag{2.59}$$

Second it is necessary to write down the explicit form of the functionals in eq.2.57 for the non-interacting auxiliary system

$$E[\rho] = T_s[\rho] + \int v_{ext}(\mathbf{r}) \rho(\mathbf{r}) d\mathbf{r} + J[\rho] + E_{xc}[\rho] \tag{2.60}$$

$$E[\rho] = -\sum_i^N \langle\phi_i|\frac{\nabla^2}{2}|\phi_i\rangle + \int v(\mathbf{r})\rho(\mathbf{r})d\mathbf{r} + \frac{1}{2}\int \frac{\rho(\mathbf{r})\rho(\mathbf{r}')}{|\mathbf{r}-\mathbf{r}'|}d\mathbf{r}d\mathbf{r}' + E_{xc}[\rho] \quad (2.61)$$

and then minimize the energy respect to the orbital variation.

$$\frac{\delta E_{KS}}{\delta\langle\phi_i|} = \frac{\delta T_s}{\delta\langle\phi_i|} + \left[\frac{\delta E_{ext}}{\delta\rho(\mathbf{r})} + \frac{\delta J}{\delta\rho(\mathbf{r})} + \frac{\delta E_{xc}}{\delta\rho(\mathbf{r})}\right]\frac{\delta\rho(\mathbf{r})}{\delta\langle\phi_i|} = 0 \quad (2.62)$$

where we have used a shorthand notation for the nuclear contribution (the external potential) $E_{ext}[\rho] = \int v_{ext}(\mathbf{r})\rho(\mathbf{r})d\mathbf{r}$. The term in square brackets in eq.2.62 can be seen as an effective potential v_{eff} acting on the auxiliary system adopted here in order to obtain the ground sate energy of the interacting one.

The minimization is usually done keeping orthonormal the orbitals and imposing that they must altogether integrate to the total number of electrons N. In this way one could also set up a Lagrange multipliers scheme in which the multiplier gains the meaning of the chemical potential μ as in eq.2.48: for more details about the μ-dependence of the Kohn-Sham equations the reader is invited to see ref.[64]. This procedure leads to a set of single particle equations (known as the *Kohn-Sham equations*),

$$\hat{H}_{KS}|\phi_i\rangle = \epsilon_i|\phi_i\rangle \quad (2.63)$$

$$\left\{-\frac{\nabla^2}{2} + \hat{v}_{eff}(\mathbf{r},\rho)\right\}|\phi_i\rangle = \epsilon_i|\phi_i\rangle \quad (2.64)$$

$$\hat{v}_{eff} = v_{ext}(\mathbf{r}) + \frac{\delta J}{\delta\rho(\mathbf{r})} + \frac{\delta E_{xc}}{\delta\rho(\mathbf{r})} \quad (2.65)$$

where the electron density is now

$$\rho(\mathbf{r}) = \sum_i^N\sum_\sigma|\phi(\mathbf{r},\sigma)|^2 \quad (2.66)$$

Once the set of equations is solved self-consistently the set of single-particle Kohn-Sham (KS) orbitals are obtained. In this scheme the orbitals associated the N lowest eigenvalues will be considered as occupied, while the others as empty.

A final remark on the kinetic energy. Generally, $T[\rho]$ cannot be written easily as a functional of the density, but in the Kohn-Sham approach T becomes explicitly a functional of the orbitals (or, from another point of view of the first order density matrix) and it assumes the usual form as in eq.2.61.

2.3.2 Kohn-Sham Equations in a Plane-Wave Basis

In order to apply density functional theory to small systems such as molecules the choice of a localized basis set for the orbitals becomes natural. In the same way for periodic systems, such as crystalline solids, the use of a plane wave basis set is also straightforward. This comes from the Bloch's theorem that shows how a periodic Hamiltonian has the following eigenfunctions

$$\Psi_{\mathbf{k}}(\mathbf{r}) = e^{i\mathbf{k}\cdot\mathbf{r}} u_{\mathbf{k}}(\mathbf{r}) \tag{2.67}$$

so a plane wave $|\mathbf{k}\rangle$ times a function of the crystal periodicity

$$u_{\mathbf{k}}(\mathbf{r}) = \sum_{\mathbf{G}} c_{\mathbf{k}}(\mathbf{G}) e^{i\mathbf{G}\cdot\mathbf{r}} = \sum_{\mathbf{G}} c_i(\mathbf{G}) |\mathbf{G}\rangle \tag{2.68}$$

where $\{\mathbf{G}_n\}$ is the set of reciprocal lattice vectors Note that $u_{\mathbf{k}}$ satisfy periodic boundary conditions: this generates a set of i eigenfunctions, here labeled as $|\mathbf{k}, i\rangle$ and introduces the need for proper normalization respect to the number of lattice sites (in real space).

We now introduce an abstract notation for plane wave vectors as

$$\langle \mathbf{r}|\mathbf{k}\rangle = \frac{1}{\sqrt{N_{cell}}} e^{i\mathbf{k}\cdot\mathbf{r}} \qquad \langle \mathbf{k}'|\mathbf{k}\rangle = \delta_{\mathbf{k}',\mathbf{k}} \tag{2.69}$$

Since every regular periodical function can be expanded as a Fourier series, hence on a plane wave basis, so it is possible to write Schrödinger's equation on such basis as

$$|\mathbf{k}, i\rangle = \sum_{\mathbf{G}} c_i(\mathbf{G}) |\mathbf{k} + \mathbf{G}\rangle \tag{2.70}$$

$$\sum_{\mathbf{G}} c_i(\mathbf{G}) \langle \mathbf{k} + \mathbf{G}'| H |\mathbf{k} + \mathbf{G}\rangle = \epsilon_i c_i(\mathbf{G}') \tag{2.71}$$

so, each plane wave in the expansion corresponds to a $\mathbf{k}'$ point in the Brillouin zone, connected to $\mathbf{k}$ by the vector $\mathbf{G}$. The size of the basis set used to represent the wave function corresponds to the largest $\mathbf{G}$ vector in eq.2.70, and it is usually expressed as an energy cutoff.

In this basis the kinetic energy matrix element is then simply

$$\langle \mathbf{k} + \mathbf{G}'| \frac{\nabla^2}{2} |\mathbf{k} + \mathbf{G}\rangle = \frac{1}{2} |\mathbf{k} + \mathbf{G}|^2 \tag{2.72}$$

while any local potential can also be used as a Fourier series

$$V(\mathbf{r}) = \sum_{\mathbf{G}} V(\mathbf{k} + \mathbf{G}) e^{i(\mathbf{k}+\mathbf{G})\cdot\mathbf{r}} \tag{2.73}$$

and its matrix elements

$$\langle \mathbf{k} + \mathbf{G}'| V |\mathbf{k} + \mathbf{G}\rangle = \sum_{\mathbf{G}} V(\mathbf{G} - \mathbf{G}') \tag{2.74}$$

and non zero only when they differ by a reciprocal lattice vector $\mathbf{G}_m$. Now for each $\mathbf{k}$ the electronic problem reads

$$\sum_{\mathbf{G}'} H_{\mathbf{G},\mathbf{G}'}(\mathbf{k}) c_{i,\mathbf{G}'}(\mathbf{k}) = \epsilon_i(\mathbf{k}) c_{i,\mathbf{G}}(\mathbf{k}) \tag{2.75}$$

in which

$$H_{\mathbf{G},\mathbf{G}'}(\mathbf{k}) = \langle \mathbf{k}+\mathbf{G}|\, \hat{H}\, |\mathbf{k}+\mathbf{G}'\rangle = \frac{1}{2}|\mathbf{k}+\mathbf{G}|^2 + V(\mathbf{G}-\mathbf{G}') \tag{2.76}$$

The Kohn-Sham form for the total energy in this framework are very convenient to be solved in the momentum space, obtaining

$$E = \frac{1}{N_k}\sum_{\mathbf{k},i} w_{k,i} \left\{ \sum_{\mathbf{G}}{}, \mathbf{G}' c^*_{i,\mathbf{G}}(\mathbf{k}) c_{i,\mathbf{G}'}(\mathbf{k}) \left[\frac{1}{2}|\mathbf{k}+\mathbf{G}|^2 + v_{ext}(\mathbf{G}-\mathbf{G}') \right] \right\} + \\ + \sum_{\mathbf{G}} \epsilon_{xc}(\mathbf{G})\rho(\mathbf{G}) + \frac{1}{2}\sum_{\mathbf{G}\neq 0} \frac{\rho \mathbf{G}^2}{G^2} + \gamma_{Ewald} + \frac{N_e}{\Omega}\sum_{\kappa} \alpha_\kappa \tag{2.77}$$

Note at first that, in order to sample all the $\mathbf{k}$s, one should map out the whole Brillouin zone, otherwise the integrals (sums) can be reduced to an irreducible Brillouin zone by introducing the proper weight $w_{k,i}$ for each point. Then particular attention should be paid to the last three terms in eq.2.77. When averaging the Coulomb potential over the density, the Fourier component at $\mathbf{G} = 0$ is divergent. This is handled within the Ewald sum (γ_{Ewald}) which is the energy of point ions in a compensating background: this is also an ill-defined sum but when combined with the divergent Coulomb term the two compensate each other giving a regular expression. Finally the last part in eq.2.77 contains the energies coming form the core electrons contributions, that usually are considered as frozen and represented by a smooth functions known as *pseudo-potentials.*

2.3.3 Remarks on the Kohn-Sham Wave Function

We will now point out few remarks about the wave function and the orbitals obtained from DFT, that can be a useful tool in theoretical chemistry, but only if used with some care. One must not confuse the Slater determinant generated from the KS orbitals with the true many-electron wave function. The Kohn-Sham scheme relies on the non-interacting auxiliary system that has nothing to do with the real one except that the two share the same electron density. In DFT the exact wave function of the target system is simply not available.

The next point concerns the role of the KS orbitals. Until recently there was believed that the KS orbitals have no physical significance except that the sum of their squares adds up to the exact density. While this is certainly true in a strict sense, after all, the KS orbitals are associated with a one-electron potential which includes all non-classical effects. Actually, the Hartree-Fock (HF) orbitals are in a sense much farther away from the real system since they neither reflect correlation effects nor do they yield the exact density, so KS orbitals should be legitimates as well as the HF ones in *e.g.* reactivity considerations. In the same way, the eigenvalues ϵ connected to the KS orbitals do not have a strict physical meaning. In Kohn-Sham theory, for example, there is no equivalent of Koopmans' theorem, which could relate orbital energies to ionization energies. There is one exception though: the eigenvalue of the highest occupied orbital, ϵ_{max}, of the KS orbitals equals the negative of the exact ionization energy because of the long range behaviour of the electron density. This holds strictly only for ϵ_{max} resulting from the exact exchange and correlation functional, not for solutions obtained with approximated ones.

At last, we have to remark that the Kohn-Sham scheme is a single determinant approach, as well as the Hartree-Fock one. Although there is an important difference among them. In the HF scheme there is no correlation included explicitly, so this should, for example, fail to correctly describe bonds dissociation where strong statical electron correlation due to the orbital near-degeneracy contribution is crucial. To include correlation in the HF scheme is necessary to add interactions among different Slater determinants each of those representing an excited electron arrangement in the orbitals (as in CI, CASSCF, etc.). In DFT, dynamical correlation is always included in the $E_{xc}[\rho]$ see eq.2.58, and for the static correlation the question rather translates into whether or not the KS non-interacting N-electron ground state can be generated by a single Slater determinant built from orbitals that are obtained as the N energetically lowest lying orbitals of a simple local potential [2].

It has been shown [65] that in a number of bond dissociations a single Slater determinant represents the non-interacting Kohn-Sham reference system at every internuclear distance. Of course, the KS orbitals must increasingly differ from

---

[2] This issue is closely related to the v-representability problem, see sec.2.2.1, and it is known as non-interacting v representability

their HF counterparts in order to incorporate the correlation effects and the resulting KS non-interacting wave function is a pretty bad approximation to the true wave function. This is not true in general for each bond, but in most of the cases holds, although approximate DFT fails badly in describing bond cleavage because of the error in $E_{xc}[\rho]$ and in particular in its non-linear behaviour for non integer charge (the so-called *self-interaction error*) that will be discussed in sec.2.5.

2.4 The Exchange and Correlation Functional

It is very important to realize that if the exact forms of the exchange and correlation functional was known, the Kohn-Sham strategy would lead to the exact energy. Thus, unlike the Hartree-Fock model, where the approximation that the wave function is a single Slater determinant (which therefore can never deliver the true solution) is introduced right from the start, the Kohn-Sham approach is in principle exact. The approximation only enters when we have to decide on an explicit form of the unknown functional for the exchange-correlation energy and the corresponding potential.

So far we have not shown any explicit form for $E_{xc}[\rho]$. The correct form of $E_{xc}[\rho]$ is unknown because there is not any simple way to include correlation without add interaction between several Slater determinants. However, it is often possible to approximate a real physical system considering that its electron density behave locally as a Fermi gas. This turns to be a good approximation for metallic systems but it fails badly for insulators ans semiconductors. This approximation is known as the *local density approximation* (LDA). The LDA functional is derived from a model (the Jellium model) assuming that the per-electron exchange-correlation energy at every point in space is equal to the per-electron exchange-correlation energy of the homogeneous electron gas (HEG).

$$E_{xc}^{LDA} = \int e^{LDA}[\rho]d\mathbf{r} = \int e^{HEG}(\rho_s)d\mathbf{r}\bigg|_{\rho_s=\rho_0(\mathbf{r})} \tag{2.78}$$

so the kinetic contribution $(T - T_s)$ and exchange-correlation energy densities (per unit volume: e and t) are approximated by the corresponding HEG analogue where its constant density ρ_s is replaced by the local value of $\rho(\mathbf{r})$. Note that $e^{HEG}(\rho)$ is a function, and not a functional of electron density. The analytical form of $e^{HEG}(\rho)$ is also unknown, but has been parametrized in several ways [66],among which the most important is probably the Ceperley-Adler one, obtained from quantum Monte Carlo calculations [67]. In the same fashion a theory for open-shell system has been developed. This is the Local Spin Density Approximation (LSDA) and take into account polarization effects due to unpaired electrons, where the spin-polarization is defines as

$$\zeta(\mathbf{r}) = \frac{\rho^{\uparrow}(\mathbf{r}) - \rho^{\downarrow}(\mathbf{r})}{\rho^{\uparrow}(\mathbf{r}) + \rho^{\downarrow}(\mathbf{r})} \tag{2.79}$$

The LSDA is simply obtained from the LDA by separation of spin contributions. The non-interacting kinetic term is spin-independent for the paramagnetic case

$$T_s[\rho^{\alpha}, \rho^{\beta}] = T_s[\rho^{\alpha}] + T_s[\rho^{\beta}] = T_s[\frac{1}{2}\rho, \frac{1}{2}\rho] \tag{2.80}$$

In this fashion the Kohn-Sham equations can be rearranged in a spin unrestricted formalism, that turns to be very useful in many practical situations such as open shell species.

Other functionals can be build in order to improve the LDA result to less homogeneous electron densities. This functionals include terms that depend on the density gradient and for this reason are known as generalized gradient approximations (GGA). Several kind of GGA functionals are available in DFT codes, all of them have been designed to fulfill specific physical requirements but still keeping a local form. Of course it is possible to find many different recipes depending on the kind of system or the properties one is interested to compute. For this reason there is not a functional better than the other and a careful testing of functionals is always necessary when approaching a new system.

A fully local exchange and correlation is, of course, not the only possible choice. For instance one can use the (non-local) Hartree-Fock exchange functional, that as well as $T[\rho]$, in the KS scheme is orbital-dependent that should be exact *only* if applied to real orbitals and not to the Kohn-Sham ones [68]. Sometimes is instead better to keep only a fraction of it. This functionals are known as *hybrids* and performs very well for semiconductors. Still hybrid functionals are not so popular since computing the exact exchange is an expensive task. Of course many other approaches exist: an extensive discussion about the several exchange and correlation functionals can be found in [69, 70, 64] or [71].

2.5 Janak Theorem and Fractional Occupation Numbers

In the Kohn-Sham scheme discussed before it has been supposed that the ground state of the physical system is a pure state. This is of course not always true: the system can indeed be in a mixed state as in eq.2.7, hence its orbital expansion can involve an arbitrary number of functions with eventually a fractional occupation number n_i. In this case the derivation of the Kohn-Sham equations is not very different since most of the terms in eq.2.62 depend directly on the electron density, and not upon the orbitals. The kinetic energy term then turns into:

$$\sum_i -n_i \langle\phi_i| \frac{\nabla^2}{2} |\phi_i\rangle \tag{2.81}$$

the minimum condition for the constrained search (sec2.2) will still be valid, provided that

$$\rho(\mathbf{r}) = \sum_{i,j} n_i |\phi_j(\mathbf{r})|^2 \qquad \sum_i n_i = N \qquad n_i \in [0,1] \tag{2.82}$$

Then, the Kohn-Sham equations in this framework remain essentially the same as in eq.2.62 for pure states except for the occupation numbers.

Interestingly the dependence on the occupation number is the following

$$\frac{\partial E}{\partial n_i} = -\langle\phi_i| \frac{\nabla^2}{2} |\phi_i\rangle + \int \frac{\delta}{\delta\rho(\mathbf{r})} \left[J[\rho] + E_{xc}[\rho] + \int v(\mathbf{r}) d\mathbf{r} \right] \frac{\partial \rho(\mathbf{r})}{\partial n_i} d\mathbf{r} \tag{2.83}$$

$$= -\langle\phi_i| \frac{\nabla^2}{2} |\phi_i\rangle + \langle\phi_i| v_{eff}(\mathbf{r}) |\phi_i\rangle = \epsilon_i \tag{2.84}$$

This result is known as the Janak theorem: it is independent on the approximation to the exchange and correlation functional and it is also valid for non-integer occupation numbers.

A non integral occupation number acquires a physical meaning only in the context of a statistical theory, e.g. in the case of an open system able to exchange particles with its environment, but it allows us to see what the system's energy should be for a fractional number of electrons. In this case one notes that system energy $E(N)$ varies *linearly* between two integer N values but a careful analysis [72] showed that it has a derivative discontinuity at every integer electrons number.

Using Janak theorem we can also define the highest partially occupied Kohn-Sham orbital (a kind of HOMO) eigenvalue

$$\epsilon_{HOMO} = \frac{\partial E}{\partial N} = \mu \tag{2.85}$$

and so changes discontinuously at a particular value Z when varying the total electron number N

$$\epsilon_{HOMO} = \begin{cases} -I_Z & N \in (Z-1, Z) \\ -A_Z & N \in (Z, Z+1) \end{cases} \tag{2.86}$$

where I_Z is the ionization energy for $N = Z$ and A_Z is the corresponding electronic affinity. The discontinuous jump between electron affinity and ionization energy turns to be a feature of the exchange-correlation functional E_{xc} [72].

The results above might not look very important but they have a great importance in the the state-of-the-art density functional calculations. Standard DFT is affected by the so-called *self interaction* error: a feature of the (classical) expression for the Coulomb energy contribution for a given electron density

$$J[\rho] = \frac{1}{2}\int \frac{\rho(\mathbf{r})\rho(\mathbf{r}')}{|\mathbf{r}-\mathbf{r}'|} d\mathbf{r} d\mathbf{r}' \tag{2.87}$$

This term allows the unphysical interaction of the density of one electron with itself, because it cannot distinguish between densities contributions coming from different electrons. The correct $E_{xc}[\rho]$ should compensate this error perfectly but indeed approximate exchange and correlation functionals such as LDA, GGA and hybrids fail in this task. The self-interaction error leads to an over-repulsion of the electron density, hence to an over-delocalization of charge. In particular the behaviour of the energy for a fractional number of electrons is spoiled by this error and turns to be convex instead then linear [73, 74]. This is a major problem for the correct prediction of a number of physical properties, especially in cases of strong correlation such as for bond cleavage.

2.6 The Hellmann-Feynman Theorem

We now show an easy way to compute forces acting on atoms that turns to be very useful for geometry relaxation of molecules and solids in DFT calculations. Suppose that the system Hamiltonian depends on a parameter λ. So the energy dependence from this parameter is simply

$$\frac{dE_\lambda}{d\lambda} = \frac{d}{d\lambda'} \left\langle \Psi_{\lambda'} | H_\lambda | \Psi_{\lambda'} \right\rangle \Big|_{\lambda'=\lambda} + \langle \Psi_\lambda | \frac{\partial H_\lambda}{\partial \lambda} | \Psi_\lambda \rangle \tag{2.88}$$

but the first term must vanish because of the energy variational principle and so we have the Hellman-Feynman theorem

$$\frac{dE_\lambda}{d\lambda} = \langle\Psi_\lambda|\frac{\partial H_\lambda}{\partial\lambda}|\Psi_\lambda\rangle \tag{2.89}$$

Being more precise one have to derive the whole left hand side of eq.2.88

$$\frac{dE_\lambda}{d\lambda} = \left\{\frac{d\left\langle\Psi_{\lambda'}\right|}{d\lambda'}H_\lambda\left|\Psi_{\lambda'}\right\rangle + \langle\Psi_\lambda|\frac{\partial H_\lambda}{\partial\lambda}|\Psi_\lambda\rangle + \left\langle\Psi_{\lambda'}\right|H_\lambda\frac{d\left|\Psi_{\lambda'}\right\rangle}{d\lambda'}\right\}\Bigg|_{\lambda'=\lambda} = \tag{2.90}$$

if the hamiltonian is hermitian one may write

$$= \left\{\langle\Psi_\lambda|\frac{\partial H_\lambda}{\partial\lambda}|\Psi_\lambda\rangle + E_\lambda\left(\frac{d\left\langle\Psi_{\lambda'}\right|}{d\lambda'}\left|\Psi_{\lambda'}\right\rangle + \left\langle\Psi_{\lambda'}\right|\frac{d\left|\Psi_{\lambda'}\right\rangle}{d\lambda'}\right)\right\}\Bigg|_{\lambda'=\lambda} = \tag{2.91}$$

$$= \left\{\langle\Psi_\lambda|\frac{\partial H_\lambda}{\partial\lambda}|\Psi_\lambda\rangle + E_\lambda\frac{d\left\langle\Psi_{\lambda'}|\Psi_{\lambda'}\right\rangle}{d\lambda'}\right\}\Bigg|_{\lambda'=\lambda} \tag{2.92}$$

but the second half of the expression above vanishes because of the wavefunction and its conjugate are supposed to depend in the same way from the parameter λ, giving the final expression stated in eq.2.89. This theorem is very useful in computing molecular forces in the harmonic approximation taking the elastic force constant as a parameter, but its validity is restricted to the adiabatic case.

Note that the Hellmann-Feynman theorem when applied to compute the electron-nucleus force along a given direction, gives the same result as in the classical electrostatic picture

$$F_A = Z_A\sum_{B\neq A} Z_B\frac{\mathbf{R}_{AB}}{R_{AB}^3} - Z_A\int \rho(\mathbf{r})\mathbf{r_A}/r_A d\mathbf{r} \tag{2.93}$$

Chapter 3

Adsorption of H Atoms on Graphene

In this chapter we shall study the chemisorption process of hydrogen atoms on graphene as a prototypical system for similar substrates (graphite, nanotubes, etc.) and for other adsorbates that form covalent bonds with carbon. Indeed graphene is a very good approximation to all the aromatic materials, whose electronic structure is essentially dominated by the π bands.

Hydrogen adsorption is a rather complicated process respect to other cases such as adsorption on metals, since a strong substrate modification is needed. The general knowledge about this process comes from few theoretical papers that showed how chemisorption occurs on a *top* site that re-hybridizes from a sp^2 to a sp^3 state. This process induces a barrier to adsorption channel that should prevent chemisorption at low temperatures.

From the experimental side not much more is known. Two different groups tried to study this process with temperature programmed desorption (TPD) and scanning tunneling microscopy (STM) methods. In both cases it was very difficult, if not impossible, to find isolated single adsorbates. They would rather cluster in pairs. In the most common dimers, the H atoms are located in the so-called ortho and para positions. To explain this effect, we will adopt a picture based on Valence Bond (VB) theory, In fact, VB can give us an important support to the physical interpretation of the "bond switching" model familiar to chemists when radical additions on the benzene ring are involved. According to this model, the first H atom would bind to a carbon atom of the benzene ring thus breaking the resonance pattern, and then the electron made free can "switch" to the ortho, para or any other equivalent position on the lattice ready to bind a second incoming H atom, thus leading to a hydrogen pair.

3.1 Theoretical Background

In this section we will summarize the theoretical tools used (beside DFT) in investigating hydrogen adsorption on graphene. This are few theorems and the Valence Bond technique, basis for the model we built to explain the substrate role during the chemisorption process, and the possibility to form magnetic textures induced by the adsorbates. This approaches indeed will allow us to justify and *predict* the total spin of a structure with one or more chemisorbed hydrogen atoms only by knowing their position on the lattice.

3.1.1 Imbalance theorem

The tight-binding (TB) model is a well known and successfully used approach to study simple solids, as shown in chapter 1 for graphene's π bands. More generally the TB Hamiltonian is easily obtained by writing the Schrödinger's equation in second quantization, in terms of atomic basis functions *e.g.* one orbital (a Wannier function) localized on each lattice site

$$\hat{H} = \sum_{\{i,j\} \in \Lambda, \sigma} t_{i,j} c^{\dagger}_{i,\sigma} c_{j,\sigma} \tag{3.1}$$

where t is the hopping integral, σ a spin index and Λ is the set of the lattice site positions, in number $N_s = |\Lambda|$. Considering that nearest-neighbour interactions are usually the largest contribution to the total energy, and neglecting the electron-electron interaction the tight-binding Hamiltonian then reads

$$\hat{H} = \hat{H}_{hop} = \sum_{<i,j>} \sum_{\sigma=\uparrow,\downarrow} t_{i,j} c^{\dagger}_{i,\sigma} c_{j,\sigma} \tag{3.2}$$

In this framework is then rather easy to make simple predictions on the ground state of the system. Using this single-particle Hamiltonian electrons tend to delocalize all over the lattice, and the ground state is essentially a homogeneous electron (Fermi) gas, *i.e.* a metal. The occupation of spin up electrons is independent on the spin down one, so uncorrelated, and if the orbitals are non-degenerate the ground state is paramagnetic, with the lowest $N/2$ orbitals doubly occupied

(Pauli paramagnetism). Let now focus on a particular class of lattices: the bipartite ones. Bipartite lattices are defined as made by two disjoint sublattices A and B with of n_A and n_B sites respectively, where $\Lambda = A \cup B$, $A \cap B = \varnothing$. The above Hamiltonian, with nearest-neighbours hoppings only, is one of such bipartite systems, and can be conveniently rewritten as

$$\hat{H} = \hat{H}_{hop} = \sum_{<i,j>} \sum_{\sigma=\uparrow,\downarrow} \left(t_{i,j} a^{\dagger}_{i,\sigma} b_{j,\sigma} + h.c. \right) \tag{3.3}$$

where now $a^{\dagger}_i$ ($b^{\dagger}_i$) is the creation operator for an electron in the i-th site $\in A$ (B) For bipartite lattices with any sublattices imbalances, Inui *et al*. formulated the following theorem [75]:

Theorem 1. (Inui et al.) *On any bipartite lattice in which the number of sublattices sites n_A and n_B are not equal, there are at least $n_A - n_B$ linearly independent eigenfunctions with zero energy eigenvalues, all with null amplitudes on the minority sublattice sites.*

Proof: the zero-energy Schrödinger's equation reads as

$$\sum_j t_{i,j} \alpha_j = 0 \tag{3.4}$$

$$\sum_i t_{j,i} \beta_i = 0 \tag{3.5}$$

where α_j (β_j) is the component of the wavefunction on the j-th site of the A (B) sublattice. Setting $\beta_i = 0$, one can always find a solution for the first set of equations, being a set of n_B equations in n_A unknowns ($n_A > n_B$), i.e. there exist $n_A - n_B$ eigenvectors at zero energy with null β_i components. .

This result will have a major importance for the density of states of defectual semiconductors for which the tight-binding model holds: anytime there is a vacancy, this introduces a zero-energy state localized on a sublattice only: a *midgap* state. Unfortunately this gives just a partial picture: because the TB Hamiltonian it is lacking of any electron-electron interactions Inui's theorem cannot predict any magnetic ordering of the system. In order to do so, it is necessary to move to an interacting model adding two-electrons terms.

3.1.2 Lieb's Theorems

An extension of the TB Hamiltonian that includes electron - electron interaction is the Hubbard model. This consists in adding to eq.3.1 an on "on-site" repulsive interaction U that rises the energy every time two electrons occupy the same orbital

$$H = \hat{H}_{hop} + \hat{H}_{int} = \sum_{<i,j>} \sum_{\sigma=\uparrow,\downarrow} (t_{i,j} c^{\dagger}_{i,\sigma} c_{j,\sigma} + h.c.) + U \sum_{i \in \Lambda} n_{i,\uparrow} n_{i,\downarrow} \tag{3.6}$$

where $n_{i,\sigma}$ is the number operator for the i-th lattice site and spin σ. The interaction term, H_{int} tends to localize electrons onto lattice sites, giving a transition from a free hopping metallic system to a (Mott-Hubbard) insulator. Both the Hamiltonian parts commute with the total spin operator $\mathbf{S_{tot}}$

$$\hat{\mathbf{S}}_{tot} = (\hat{S}^{x}_{tot}, \hat{S}^{y}_{tot}, \hat{S}^{z}_{tot}) \tag{3.7}$$

$$\hat{S}^{\alpha}_{tot} = \sum_{i \in \Lambda} \sum_{\sigma,\tau=\uparrow,\downarrow} \frac{1}{2} c^{\dagger}_{i,\sigma} \sigma^{\alpha}_{\sigma,\tau} c_{i,\tau} \tag{3.8}$$

(here $\sigma^{x,y,z}$ are the Pauli matrices), i.e. it is always possible to obtain a common eigenstate of both the Hamiltonian and the total spin, and thereafter only these solutions will be considered. Since $\hat{S}_{tot}$ is the generator of the rotations group in the spin space, both H_{hop} and H_{int} are $SU(2)$ invariant.

For a non-hopping system (in which $\hat{H} = \hat{H}_{int}$) electrons tend to localized in atomic orbitals that can be divided in two subsets X and Y which host respectively only spin up or spin down electrons. In the atomic-centered basis the Hamiltonian is already diagonal and its ground state has an energy given by doubly occupied sites only

$$E = \sum_{i \in X \cap Y} U \tag{3.9}$$

The ground state for a given electron number N can be build by choosing two subsets of lattice positions X and Y that minimize the energy. When one has $N \leq |\Lambda|$, one can always choose X and Y such that $X \cap Y = \varnothing$: thus the ground state has energy equal to 0. Otherwise several arrangements are possible, but none of them have a precise long-range magnetic ordering. The phase will be then paramagnetic.

By definition a structure exhibits *ferromagnetism* if its ground state has the maximum total spin, S_{max}. The eigenvalue of the total spin operator for a lattice with

N_s sites and N electrons can be easily predicted to be

$$S_{max} = \begin{cases} N/2 & N \leq N_s \\ (2N_s - N)/2 & N \geq N_s \end{cases} \tag{3.10}$$

Neither the hopping (tight-binding), nor the interaction term of the Hamiltonian alone are responsible for magnetic ordering in the Hubbard model. In fact they give both non magnetic ground states when considered alone and only their mutual action may give rise to magnetic textures. A *U*-*t* phase diagram for the Hubbard model has not been built yet and this relation is still an active field of research. Ferromagnetic solutions are particularly difficult to achieve, nevertheless few analytical results about the necessary conditions for this ordering are known. Here we will present (without proof) few theorems that have deep consequences on the possible rising of ferromagnetism in this model [76].

Theorem 2. (Lieb-Mattis) *Consider a one dimensional lattice* $\Lambda = 1, 2, ..$ *with open boundary conditions. We assume that the hopping matrix elements are* $t_{i,j} = 0$ *when* $|i - j| > 1$*. Then, the system energies satisfy the inequality*

$$E(S) < E(S + 1) \tag{3.11}$$

for any $S = S_{min}, S_{min} + 1, ..S_{max} - 1$ *(where* $S_{min} = mod(N, 2)/2$ *and* $S_{max} = N/2$*).*

The main consequence of this theorem is that the ground state of a one-dimensional Hubbard model will have the lowest $|S_{max}|$ possible, even though some care is needed in using such statement. The open boundary conditions are not a strong limitation, since one can always choose a system big enough to be considered as a realistic material, but the reduced dimensionality and the nearest-neighbour interaction required by this theorem are more serious constrains that limit its application to simple toy models.
Starting from the Lieb-Mattis theorem, Lieb obtained later a more versatile generalization, at the prize to be valid only for bipartite lattices [77].

Theorem 3. (Lieb) *Consider a Hubbard model on a bipartite lattice where* $t_{i,j} = 0$ *if* $i, j \in A$ *or* $i, j \in B$ *and* $t_{i,j} \neq 0$ *elsewhere. We assume that the whole lattice is connected by non zero* $t_{i,j}$ *(connectivity condition). When* $N = N_s$ *the ground*

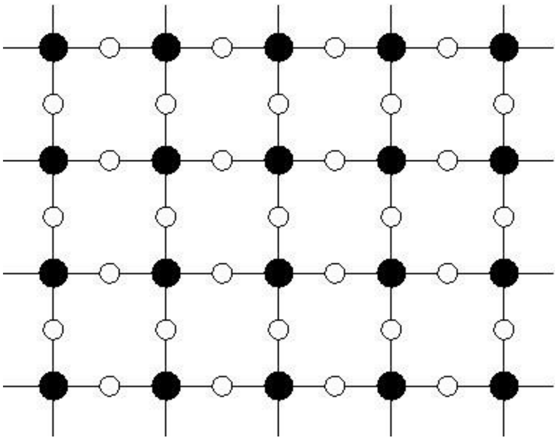

Figure 3.1: An example (the CuO lattice plane in cuprates) of a cubic bipartite lattice in which the number of sites in two sublattices are different. As a consequence of Lieb's theorem the Hubbard model with U > 0 on this lattice has $S_{tot} = N_e/6$ when $N_e = |\Lambda|$. Note that to be bipartite one atom per site has to be considered

state of the system has a total spin $S_{tot} = |n_A - n_B|/2$ *for every non-negative U value, where* $n_A = |A|$ *and similarly for* n_B*.*

Note that this theorem applies to a number of electrons equal to the number of lattice sites $N = N_s$, usually referred as *half filling*, since this is a half of the highest possible orbital occupation.
The Lieb theorem turns to be more useful than the previous one having no limitation respect to the lattice dimensionality and being valid even in the limit $U = 0$, *i.e.* for non-interacting (tight-binding) models. On the other hand the bipartiteness of the lattice is the most stringent condition that involves implicitly a nearest-neighbour interaction. Now the total spin of the system's ground state is known, but theorem 3 gives not still any information the magnetic ordering. In this case it is anti-ferromagnetic as stated by this other theorem [78]:

Theorem 4. (Shen, Qiu and Tian) *Assume the same conditions as in theorem 3, If* $|\Psi\rangle$ *is the system's ground state, then the following inequalities holds:*

$$\left\langle \Psi_0 \left| \hat{\mathbf{S}}_{\mathbf{i}}^{+} \cdot \hat{\mathbf{S}}_{\mathbf{j}}^{-} \Psi_0 \right. \right\rangle \begin{cases} > 0 & \textit{if } \ i,j \in A, \ \textit{or} \ i,j \in B \\ < 0 & \textit{if } \ i \in A, \ j \in B \ \textit{or} \ i \in B, \ j \in A \end{cases} \tag{3.12}$$

Ferromagnetism in bipartite systems is then ruled out by the theorems above, but only if the number of sublattices sites n_A and n_B is equal (see ref.[79] for

further details). Otherwise, when this condition is not fulfilled as in defectual systems or in a lattice such as in fig.3.1, the solution is a *ferrimagnetic* ground state with a total spin of $|n_A - n_B|/2$.
Concluding, from the theorems above one should expect for bipartite lattices at half filling that electrons on nearest neighbour sites are antiferromagnetically coupled (singlet): when introducing a sublattice imbalance $|n_A - n_B|$ midgap states arise, coupled ferromagnetically, to a total spin $|n_A - n_B|/2$.

3.2 Valence Bond Theory

The Valence Bond (VB) approach is a quantum chemistry method that has its roots on the notion that the chemical bond is associated to the pairing of electrons with different spins, that is, essentially the basis of the Lewis theory of chemical bond (*i.e* Lewis structures). The idea behind the VB approach is that the most stable bond between two atoms occurs when their electrons are paired, corresponding to the spin situation S_z=0. The VB theory was applied for the first time by Heitler and London back in 1927 [80], to build the wave function of the hydrogen molecule by using atomic functions (a and b) centered on the H_a and H_b nuclei, as following

$$\Psi(1,2) = \frac{1}{\sqrt{2}}[a(1)b(2) + b(1)a(2)] \tag{3.13}$$

where numbers represent electron spatial coordinates sets. Then, electron spins can be arranged to form a singlet, or a triplet wave function

$$\Psi_{^1\Sigma_g^+}(1,2) = \frac{1}{\sqrt{2}}[a(1)b(2) + b(1)a(2)][\alpha(1)\beta(2) - \beta(1)\alpha(2)] \tag{3.14}$$

$$\Psi_{^3\Sigma_u^+}(1,2) = \frac{1}{\sqrt{2}}[a(1)b(2) - b(1)a(2)] \begin{bmatrix} \alpha(1)\alpha(2) \\ \alpha(1)\beta(2) + \beta(1)\alpha(2) \\ \beta(1)\beta(2) \end{bmatrix} \tag{3.15}$$

the singlet case (corresponding to the structures 1 and 2 in fig.3.2) being the most stable one. The two functions in eq.3.11 can be written as a combination of Slater determinants

$$\Psi_{S,T}(1,2) = |a\bar{b}| \mp |\bar{a}b| \tag{3.16}$$

where the minus and plus signs are for singlet (S) and triplet (T) solutions, and the bar represents a spin down spin-orbital, in the usual quantum chemistry notation.

Figure 3.2: Valence Bond representation of the possible configurations for the H_2 molecule. 1: singlet coupling, anti-symmetrical respect to electron permutation, 2. the same but with exchanged electrons as in the second configuration in eq.3.14. 3 and 4: the two spin structures that, together with the symmetrical combination of 1. and 2., form the triplet solution in eq.3.15.

This approach was extended by Slater and Pauling [81] in order to treat bigger molecules, with several bonds, according to the so-called Heitler-London-Slater-Pauling (HLSP) VB model. Being usually the singlet wave function the most important for the chemical bond description, each bond in a polyatomic molecule can be treated as isolated form all the others. In this way, the singlet function for a $2N$ electrons molecule can be built as the product of N electron pair singlet functions as the one in eq.3.14. These kinds of structures are known as prefect pairing functions. Note that combinations of Slater determinant as in the VB wave function (see eq.3.16) are "pure spin" functions, namely $\hat{S}^2$ eignefunctions.

Back to the H_2 molecule, and its VB wave function in eq.3.13, to a closer look there are two other possible electron arrangements: the so-called ionic structures, in which both electrons are paired in the same spatial orbital, giving determinants of the kind $|a\bar{a}|$ (fig.3.3). The hydrogen molecule perfect pairing wave function, Ψ_S, is already a good description of he system in its ground state, being the H-H bond purely covalent. In general, in order to build a more accurate VB wave function it is necessary to mix the covalent structure with the ionic ones. For H_2, the mixing is of about 25%

$$\Psi_{full} = \lambda(|a\bar{b}| - |\bar{a}b|) + \mu(|a\bar{a}| + |\bar{b}b|) \qquad \lambda > \mu \tag{3.17}$$

Of course the weight of the ionic configurations is not the same along the whole bond dissociation path. While they are rather important close to equilibrium, stretching the bond their weight starts to drop, until the asymptotic point of bond cleavage where the two purely neutral atomic species are present. Indeed, the ionic structures make the VB wave function to dissociate correctly. Of course for non-homopolar bonds the influence of the ionic structures is more relevant,

Figure 3.3: Ionic valence bond structure for the H_2 molecule as in eq.3.17.

even asymptotically.

The HLPS VB theory became a strong tool for quantum chemists widely used in studies of molecular properties. It is important to note that the validity of that empirical approach was confirmed by the first ab initio VB calculations [82].

A further improvement of the VB theory was achieved when flexible orbitals were used in building the wave functions, and this was realized by orbital "polarization", that is, by mixing the orbitals of the two atomic centers, thus giving rise to the so called Coulson-Fisher wave function. This is the basis of the modern VB theory developed in the form of the Spin Coupled VB (SCVB) and Generalized VB (GVB) approaches, in which a single determinant is used in all the possible spin arrangements, and both orbital and spin configurations coefficients are simultaneously optimized, without any particular orthogonality constrain [83, 84, 85, 86] In any case, for our purpose, only covalent structures will be considered in our VB description.

3.2.1 VB Wave Function: Benzene Molecule

Following the HLSP approach is possible to build a Valence Bond theory for molecular systems based on the singlet pairing discussed before. For a given molecule the possible perfect pairing structures grows with the number of nuclei (orbitals) considered. As an example we take the benzene molecule, whose aromatic bonds can be used as a prototype for the understanding of graphene properties. Considering only the six π electrons one of the possible perfect pairing wave functions is the following:

$$\Psi = |(a\bar{b} - \bar{a}b)(c\bar{d} - \bar{c}d)(e\bar{f} - \bar{e}f)| =$$

$$\begin{aligned} &= |a\bar{b}c\bar{d}e\bar{f}| - |a\bar{b}c\bar{d}\bar{e}f| - |a\bar{b}\bar{c}de\bar{f}| + |a\bar{b}\bar{c}d\bar{e}f| - \\ &\quad |\bar{a}bc\bar{d}e\bar{f}| + |\bar{a}bc\bar{d}\bar{e}f| + |\bar{a}b\bar{c}de\bar{f}| - |\bar{a}b\bar{c}d\bar{e}f| \end{aligned} \tag{3.18}$$

A graphical representation of eq.3.18 is known as Rumer diagram, shown in fig.3.4

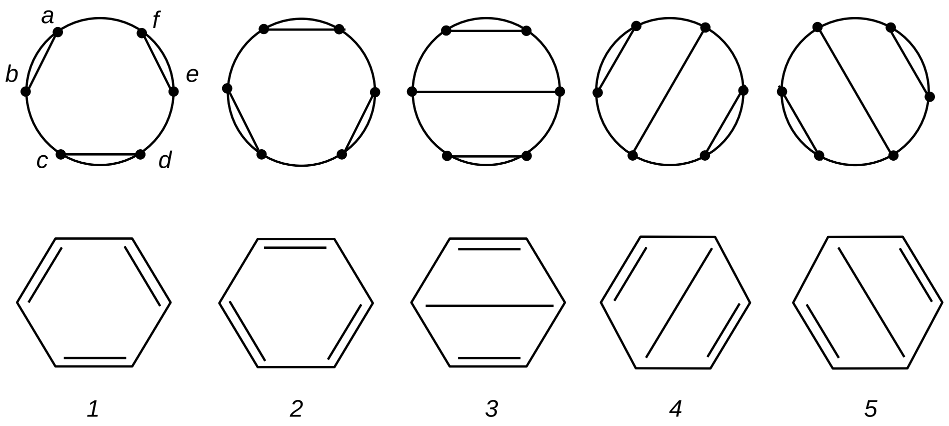

Figure 3.4: The six possible perfect pairing Rumer diagrams for the benzene molecule with their correspondence with Kekulé (1-3) and Dewar (4 and 5) resonance structure.

structure 1, and in this case each of them correspond to eight Slater determinants. In Rumer diagrams each orbital (atom) is represented by a dot on a circumference and the spin pairings by lines that connects them. Indeed by drawing all the possible connections between points one can easily build all the other perfect pairing functions necessary to completely span the subspace of the singlet configurations: for benzene these functions are five (the two Kekulé and three Dewar structures) shown in fig.3.4. Note that when two lines cross each other the resulting pairing is no more independent from the others, hence has not to be taken into account [87].

Rumer functions are then used as basis vectors to diagonalize the electronic Hamiltonian, but they have also another meaning: from the relative weight of each diagram in the optimized wave function is possible to understand which are the most important chemical structures involved in the bond. It is in fact possible to notice that for cyclic π systems the diagrams directly mirror the molecule spatial symmetry, hence they mimic Lewis' formula that in the case of benzene translates into Kekulé and Dewar structures. From another point of view resonance structures commonly drawn for π systems acquire quantum mechanical meaning as they correspond to basis functions that spans the space of function of a given multeplicity. The VB wave function is hence a linear combinations of Lewis structures, from which is natural to develop the concept of *resonance*: this translate into a series of Rumer function with equal weight in the final wave function.

Nowadays VB calculations can be performed rather easily for simple molecules

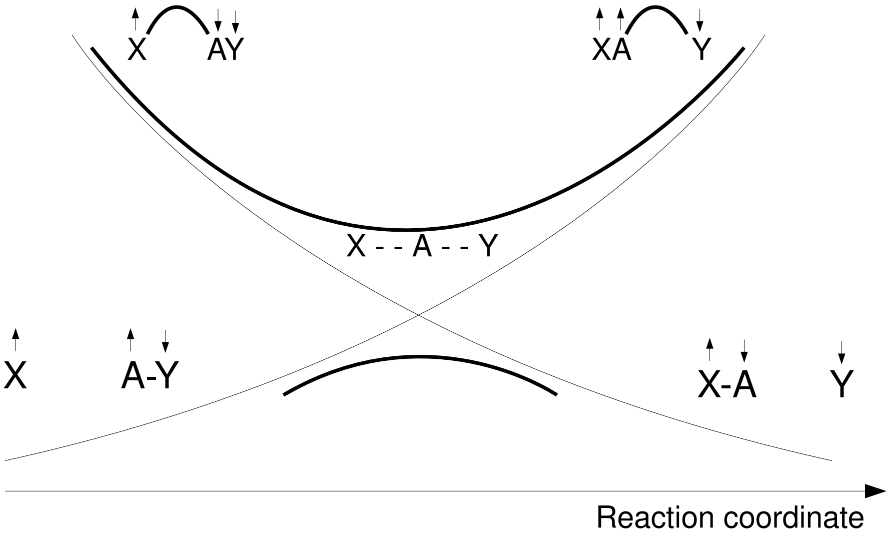

Figure 3.5: Valence Bond correlation diagram for an radical exchange reaction X+AY→XA+Y obtained using the covalent structures only. The reactants and product curves represents the energy profile for a given spin coupling along the reaction coordinate. As the coupled atoms get further (closer) the energy raises (falls). The transition state is located at the curve crossing, and their adiabatic average (avoided crossing) forms two distinct potential energy curves (in bold).

up to 10 - 15 electrons, bigger systems are unfeasible since the number of Rumer functions increases dramatically with the number of electrons. For the case of benzene *ab initio* VB calculation have been performed time ago, including Kekulé, Dewar and a number of ionic structures known as orthopolar [88]. The results show that Kekulé structures are as expected the most important for the aromatic bond, followed by Dewar and orthopolars.

3.2.2 VB Correlation Diagram for Radical Exchange Reactions

To represent how the electrons re-arrange during a reaction from a VB point of view, is possible to build a *correlation diagram*. Such diagrams show the energy profiles for given VB structures as a function of the reaction coordinate, in a ”diabatic” curve. For the simple case of a radical exchange reaction for a diatomical molecule such as in figure 3.5

$$X^{\cdot} + AY \rightarrow XA + Y^{\cdot} \tag{3.19}$$

there are eight different VB structures: two covalent and six ionics. In reactants and products states the two atoms forming the molecule are singlet-coupled close each other, while the radical is placed further away. Let suppose that all of them lay at the same energy, as in $H^{\cdot} + HH \rightarrow HH + H^{\cdot}$, then their VB wave function would be the Heitler-London function for the molecule plus a single atomic function for the a radical. Moving along the reaction coordinate, the $A - Y$ distance will increases, while the $A - X$ one decreases and if the spin coupling is kept fixed the total energy will rise, obtaining a diabatic curve. This energy rise comes form the (triplet) repulsion between the non-bonded fragments A and X. As well the products energy will increase moving toward the reactants. This diabatic curves will cross at the transition state, that in this simple example lays half way between reactants and products.

Allowing the configurations to mix, we then obtain adiabatic curves, in which a barrier appears as result of the avoided crossing of the diabatic ones. The height of the activation barrier is then

$$\Delta E = \Delta E_c - E_{res} \tag{3.20}$$

or the energy at the curves crossing (ΔE_c) minus the stabilizing effect (E_{res}) of the resonance between the reactants and products structures, that lowers the total energy because of the mixing of the two VB structures.

3.3 Single H Atom Adsorption

An hydrogen atom that impinges on a graphene surface can either physisorb or chemisorb. Physisorption has been recently studied with *ab initio* correlated method, and it turned to be a very weak interaction (∼40 meV), meaning that H will easily desorb at temperatures higher than 100 K [89]. For this reason, chemisorption is more interesting for applications. This system has great importance in many fields, but most of all it can be considered as a model for radical adsorption on sp^2 bonded carbon, such as graphite and carbon nanotubes.

Chemisorption of single H atoms on graphite has long been studied since the works of Jeloaica and Sidis [91], and Sha and Jackson [90]. The first study used DFT with atomic basis on a cluster model made of a coronene molecule, while the latter used a plane wave code on a small graphite unit cell in order to model H adsorption. Among the four possible adsorption sites hollow and bridge, are not

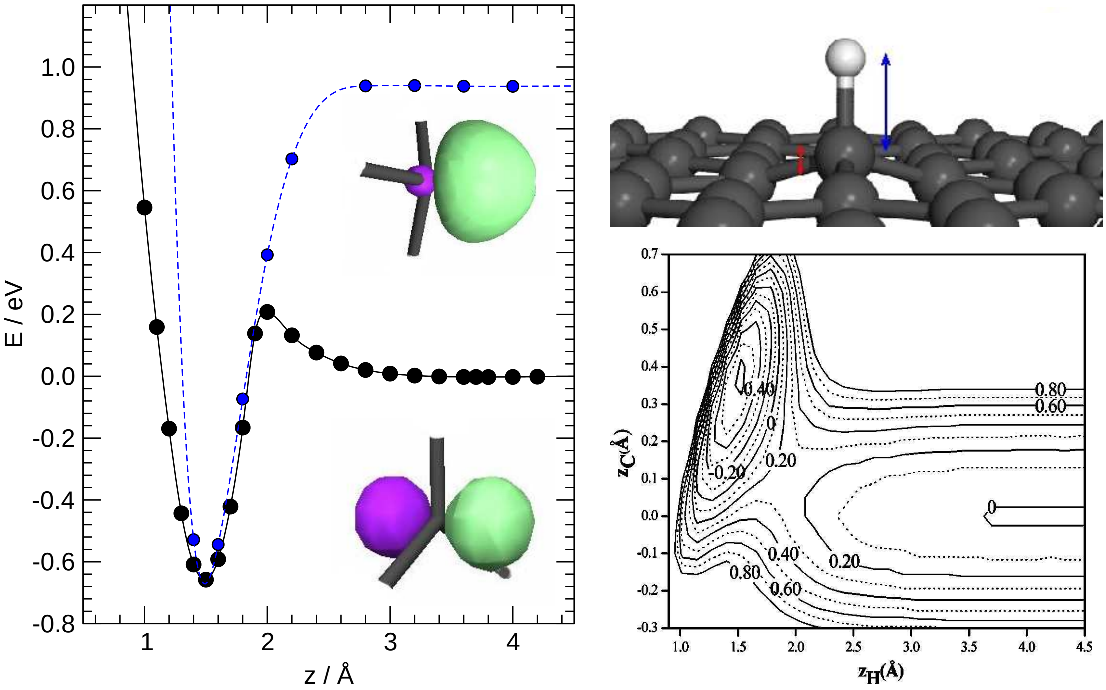

Figure 3.6: Left panel: Chemisorption curve for a H atom on graphene *top* site on a 2x2 supercell. Black curve: the adiabatic path, the carbon atom is allowed to relax to equilibrium geometry at each C-H distance. Blue curve: diabatic path: the top site is kept fixed in the puckered geometry. Here z is the adsorbate height on the surface. Right panel: equilibrium geometry: the red arrow indicates the puckering height, while the blue one the C-H distance. A cut of the potential energy surface for this process is also shown (from ref.[90]) where it can be noticed the barrier position.

binding while the two kinds of top sites (with or without an carbon atom on the layer underneath for graphite) give essentially the same behavior.

Adsorption on the top site induces surface reconstruction. If the graphene layer is kept flat the carbon - hydrogen bond is metastable, while allowing surface relaxation chemisorption becomes an activated process with rather stable products. Such a surface reconstruction consists in the puckering of the carbon atom beneath the adsorbed hydrogen, and occurs as a consequence of $sp^2 - sp^3$ re-hybridization of the valence carbon orbitals needed to form the CH bond. The re-hybridization induces a change in geometry of the substrate site, from a planar (sp^2) to a tetrahedral (sp^3) form, puckering out the carbon atom from the surface plane. The orbital re-hybridization turns to be necessary for the chemisorption process, since the C-H bond in graphene can involve sp^3 carbon only: for this reason chemisorption on sites that cannot re-hybridize atomic orbitals (bridge and hollow) cannot be stable.

When the hydrogen atom impinges on a carbon *top* site to already puckered, so already in the sp^3 form, chemisorption is a barrierless process. Otherwise, following an adiabatic path (hence allowing the carbon atom relaxation to its equilibrium position at every point along the reaction coordinate) we found an energy barrier $\sim$0.2 eV high, induced by the re-hybridization. The adsorption curves are shown in fig.3.6.

This picture found a substantial experimental proof for graphite surfaces from TPD, AES, EELS and HREELS spectroscopy data [92], that have been recently re-interpreted in detail with the help of kinetic Monte Carlo methods [93, 94]. So, it turns out that chemisorption is a thermally activated process which will hardly occurs at and below room temperature.

3.3.1 Adsorption and its Effect on the Substrate Density of States

In order to understand the physics beneath hydrogen atom adsorption we computed first the chemisorption energy on a rather large (5x5) graphene supercell. In addition, we have investigated the electronic substrate properties of the resulting hydrogenated graphene, in order to get hints for understanding the adsorption process of additional atoms. In fig.3.7 we show the density of states (DOS) of the H-graphene equilibrium structure (bottom panel), compared to that of clean graphene (top panel). It is evident from the figure that hydrogen adsorption causes the appearance of a band gap and of two peaks in the DOS, symmetrically placed around the Fermi level: one filled and one empty, with different spin projections. The two peaks in the DOS are known as *midgap* states and represent states localized in space. This comes from the comparison with free-electron bands, fully delocalized, that are parabolic and give broad density of states. Indeed these states are flatbands, localized on a sublattice only, and the filled one lays on the one that does not bear the adsorbate.

The change in the graphene's electronic structure upon adsorption can be understood using the one-electron picture of tight-binding Hamiltonian. When the hydrogen atom binds covalently to carbon its electron couples with one in a p_z orbital, taking it away from the π bonds network, hence creating an imbalance

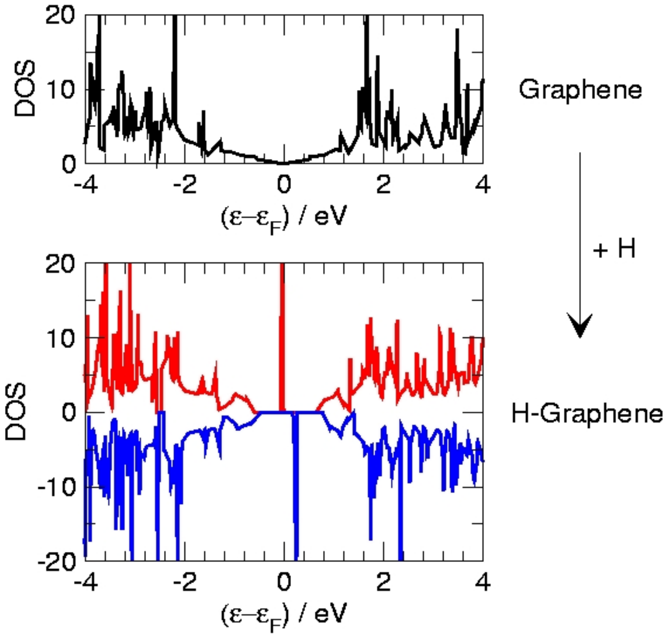

Figure 3.7: Graphene density of states before (upper panel) and after (lower panel) hydrogen adsorption. Note how the sublattice imbalance induced by adsorption opens a band gap and induces two midgap states, one per spin projection.

in the two sublattices. Graphene is made of two equal hexagonal bi-dimensional lattices (A and B) where each of them include every second carbon atom, as can be seen in fig.1.1, so theorem.1 should hold and for such imbalances it predicts the appearance of midgap states. Note that despite the theorem has been formulated for non-interacting systems (as in tight-binding approximation), it seems to be valid in this framework as well.

There is one sublattice imbalance, so one zero-energy midgap state whose spin degeneracy is lifted if exchange-correlation effects are taken into account, as shown in fig. 3.7 for our DFT results. Hence one has a filled midgap state of a single spin projection (spin majority), and an empty one of the other projection (spin minority). The total spin of the system is $S_z = 1/2$ in agreement also with (Lieb's) theorem 3. This suggests that hydrogen atoms can be used to design long range magnetic structures that, being the midgap states associated with a single spin, might be used for spin-tronics applications.

The midgap state has been mapped out in Fig.3.8, where we report a contour map of the spin density at a constant height of 0.47 Å above the surface. It is clear from the figure that if adsorption occurs on an A lattice site the spin density (due mainly to the above occupied midgap state) localizes on B lattice sites. The

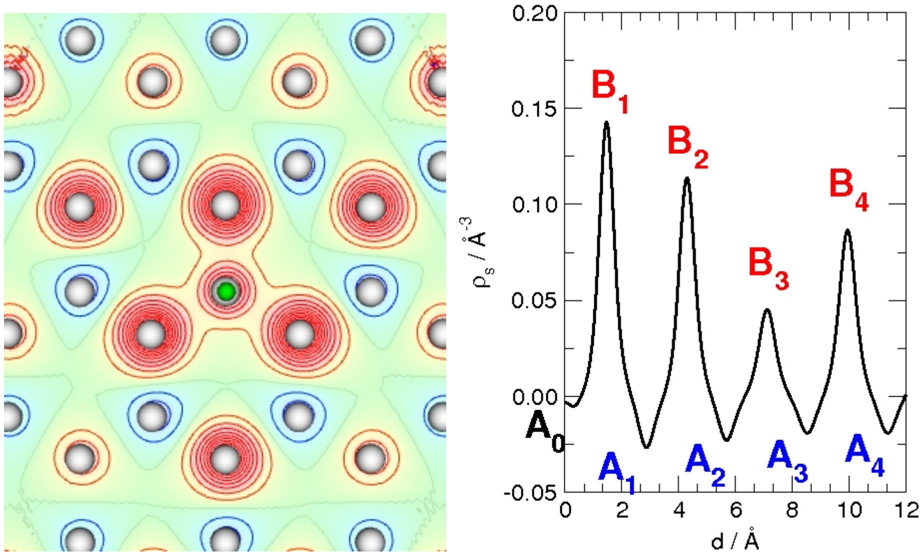

Figure 3.8: Spin density at 0.47 Å above the graphene surface after adsorption of a hydrogen atom. Left: Contour map with red/blue lines for spin-up/spin-down excess, respectively. Right: Spin density at the same height as on the left panel, along a path that moves away from the adsorbate joining C atoms. Atomic labels follow notation from fig.4.1

latter now contain most of the 1 μ_B magnetization previously carried by the H atom species, and a slight spin-down excess on A sites results as a consequence of the spin polarization of the lower-lying states[95]. The overall spin density reconstruction has a symmetry very similar to a $\sqrt{3}$x$\sqrt{3}$R30° pattern, the one seen in experiments for other π defects *e.g.* vacancies, voids, and also step edges such as in graphene nanoribbons [96].

This is made clearer in the right panel of fig.3.8 where we report the spin density at the same height above the surface as before along a rectilinear path joining a number of carbon atom sites away from the adsorption site. Note that the spin density decays only slowly with the distance from the adsorption site, in agreement with theoretical results that suggest for the case of two dimensional graphene a decay corresponding to a non-normalizable state with a $1/r$ tail [97].

From fig.3.8 is possible to see how the decay with the distance of the spin density due to the midgap state stops after few atoms from the adsorbate, where it starts to rise again. This is an effect of the periodic boundary conditions of the DFT calculations. Midgap states need an extremely large supercell in order to accommodate all the spin density they induce, and on smaller cells some interaction

unit cell	θ / ML	d_{puck} /Å		E_{chem} / eV	
		this work	others	this work	others
1x1	0.500	-	-	-	0.46[1]
2x2	0.250	-	-	-	0.56[1]
2x2	0.125	0.36	0.36[1]	0.75	0.67[2]
3x3	0.062	0.42	0.41[3]	0.77	0.76[3]
cluster	0.045	-	0.57[4]	-	0.76[4]
4x4	0.031	0.48	-	0.79	0.76[5], 0.85[6]
5x5	0.020	0.59	-	0.84	0.71[7], 0.82[8]
8x8	0.008	-	-	-	0.87[9]

Table 3.1: Chemisorption energy (E_{chem}) and equilibrium height of the C atom above the surface (d_{puck}) for H adsorption on top of a C atom, for a number of surface unit cells, corresponding to different coverages θ. Ref. 1 [92], Ref. 2 [90], Ref. 3 [98], Ref. 4 [99], Ref. 5 [100], Ref. 6 [101], Ref. 7 [102], Ref. 8 [103], Ref. 9 [104].

between periodic replica is unavoidable. We studied different surface coverages in order to compare our results with other known in literature. We have found that both the binding energy and the puckering height are strongly affected by the size of the unit cell (see table 3.1), and even the results of the 5x5 cell turn out to be in error of about 30 meV with respect to the isolated atom limit estimated by calculation at 0.008 ML coverage. With the setup showed in appendix.B, namely a 5x5 unit cell mapped by a 6x6x1 k-point mesh and a GGA functional, we obtained a puckering of 0.59 Å and a bonding energy of 0.84 eV. Our computational setup is then not optimal for the study of midgap states, but seems to give energies well converged respect to the cell size. The reason for this dramatic dependence on the cell size is probably again the slow spatial decay of the midgap state, that needs very large cells to minimize the interaction with its periodic neighbours. Experiments showed that indeed single H atoms on graphite {0001} surfaces induce long-range density perturbations up to a range of 35 Å[105, 106].

Very recently Šljivančanin *et al.* suggested that a very dense k-points grid can give converged chemisorption energies also for very small super-cells [107]. This is actually reasonable since the midgap state has a very oscillating density being localized onto one sublattice only. Anyway, our result is still very close to what they obtained (0.83 eV) with a very dense k-points meshes, up to 162x162x1 points, and fits well with experimental findings [92, 108, 109, 110, 111, 112].

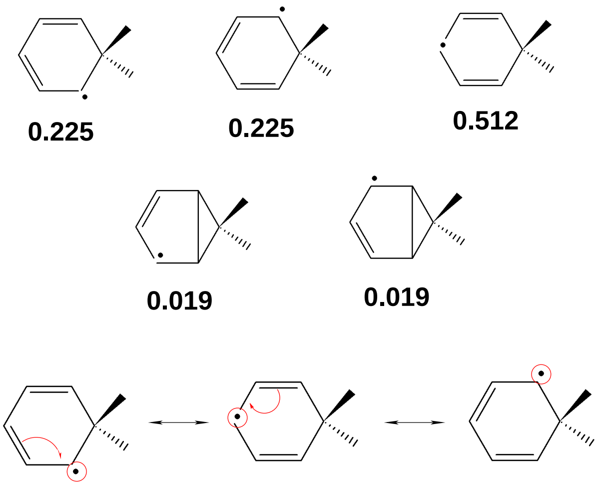

Figure 3.9: Valence Bond model for radical attack on a benzene molecule. The Rumer function's weigths have been computed with the SCVB method [113]. When two general substituent are connected to the same carbon one of the aromatic π bonds is broken and an electron is set free. This can move on ortho and para position by bond switching.

We also computed the activation energy for the chemisorption process. Our result is 0.14 eV, surprisingly lower in energy respect to the 0.2 eV of other studies [90], but still in good agreement with the experimental data (0.18 eV) for D atoms on graphite surfaces [92, 110].

3.4 The VB Interpretation

We now try to give a simple "chemical" picture of the processes occurring during hydrogen chemisorption onto graphene and graphite surfaces. This interpretation is based upon Lewis structures, that acquire a physical meaning when seen under the light of the Valence Bond theory, *i.e.* as Rumer functions (see sec.3.2 and sec.3.2.1).

From a chemical point of view the aromatic character of graphene π band comes from the resonance of the two Kekulé structures with the two possible single-double bond alternation. Restricting first the model to radical attack on a benzene molecule when a hydrogen atom chemisorbs it breaks the aromatic network localizing one electron on the lattice, that is the midgap state. The product of such process is then a molecule with 5 π electrons: its lowest-spin structures together with their weigths from spin coupled VB calculations are in fig.3.9 [113]. The largest contribution to the ground state wave function comes from the Rumer functions with a free electron in the so-called *ortho* and *para* position respect to the radical attachment site. The *meta* position involves a Dewar-like structure, with a spin coupling across the ring, and hence gives a very low contribution to the total ground state solution. This is well known from basic organic chemistry where this kind of mechanism is responsible for orientation effects in *e.g.* electrophilic aromatic substitutions. Using a naive but very effective picture used for organic reactions one might see the localization in ortho and para position as a "switching" of the double bonds as shown in the lower panel fig.3.9.

Exporting what we said for benzene onto graphene it then rather easy. Once a hydrogen atom has been adsorbed on the surface, an unpaired electron is localized on one of the neighboring C atoms, which can subsequently move in each of the carbon atoms belonging to the same sublattice by "bond switching". Note that such a switching allows the lone electron to lay on one sublattice only, namely the one that does *not* include the adsorption site. A picture of the mechanism is shown in fig.3.10 for a coronene model, that should represent the whole graphene lattice. Spin alternation arises from the resonant behavior of an unpaired electron in α position (the nearest neighbor one) with respect to a double bond: such a resonance can also be naively viewed as the spin re-coupling of the unpaired electron with the electron on the neighboring site, a process which sets free a second electron on the same sublattice. This gives another explanation of the midgap state spatial localization that involves one sublattice only.

We now analyze the reaction mechanism looking at the VB correlation diagram for this process. The elementary processes involved in the reaction are the following: first a spin excitation releases an electron from the π bonds, second this free electron localizes on a definite carbon atom inducing re-hybridization *i.e.* lattice distortion, and as third it couples to the hydrogen atoms one to form the bond. The first two steps require some energy, while the last one releases the C-H bond formation energy. In a diabatic picture (*i.e.*, when constraining the spin coupling to the Kekulé structures of fig.3.10a, the interaction between graphene and the incoming H atom is expected to be repulsive since no electron is available to form the C-H bond. On the other hand, a low-lying spin-excited state corresponding to a Dewar-like structure (which has necessarily two singlet-paired electrons on

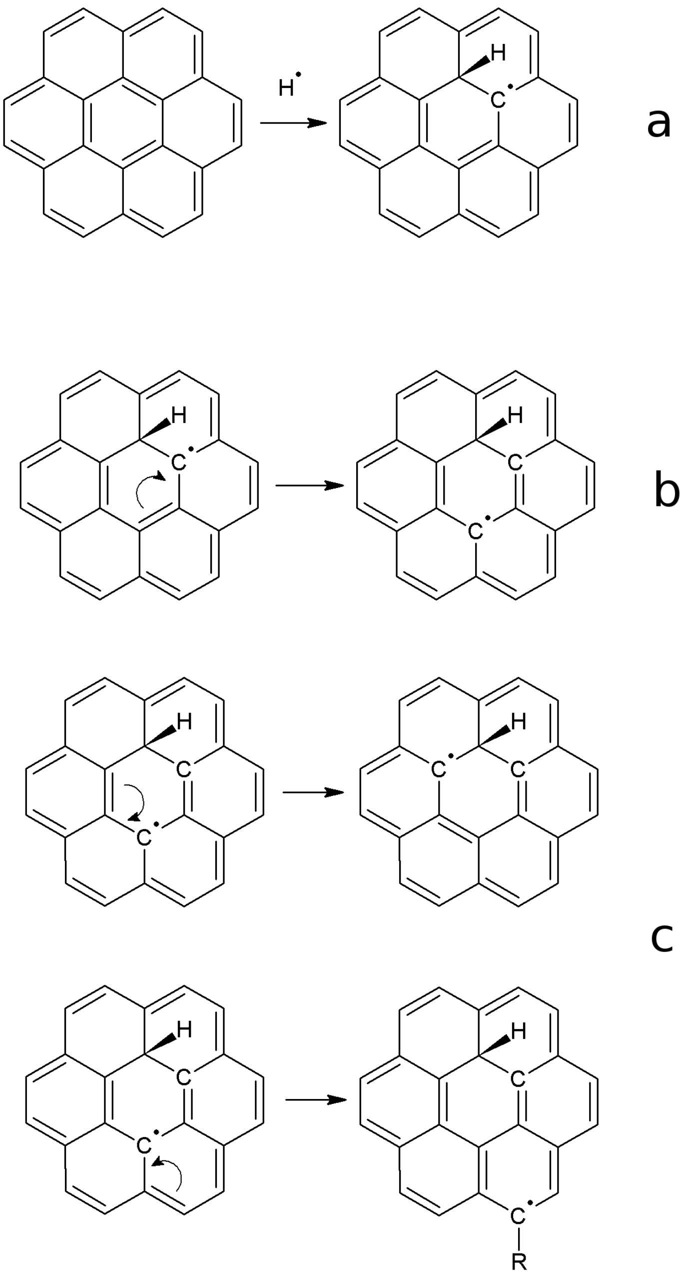

Figure 3.10: Hydrogen chemisorption reaction mechanism shown on a coronene molecule model. a) The radical attacks one carbon atom establishing a covalent bond by coupling its electron with carbon p_z one. One of the many double bonds of the aromatic network is broken, so an electron is set free on the ortho position. b) The lone electron can delocalized on the para position or c) on any other position on the sublattice that does not bear the adsorbate.

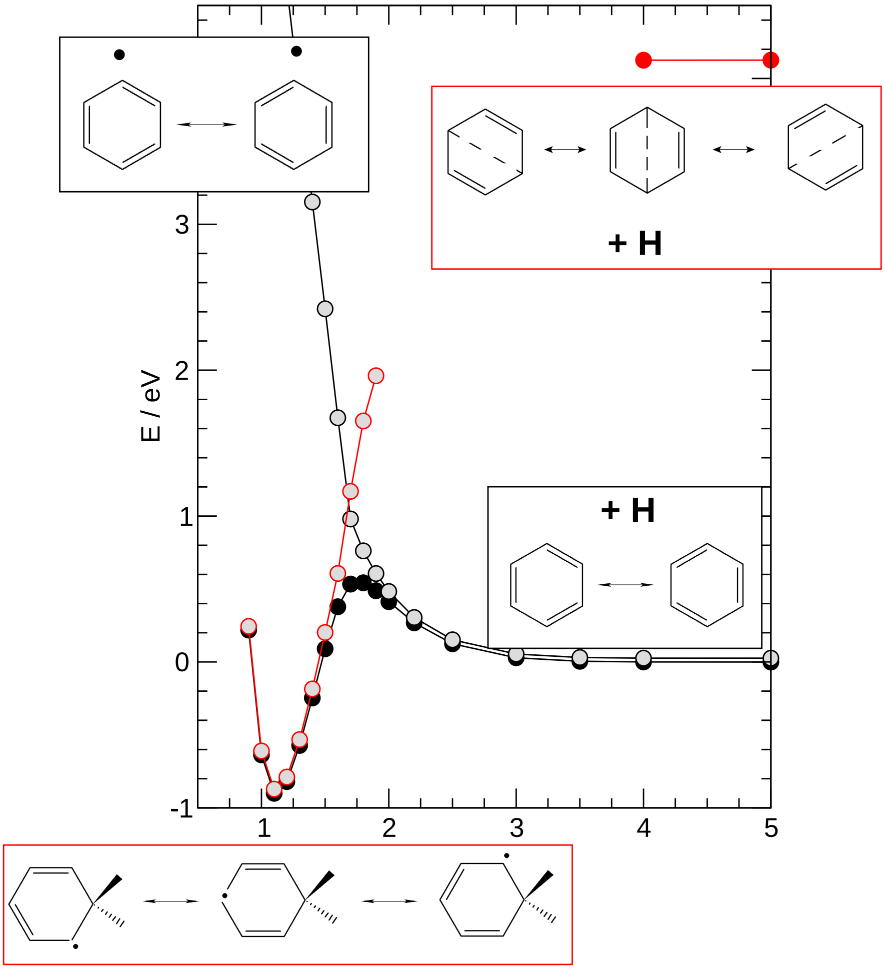

Figure 3.11: Correlation diagram for H attack on a benzene molecule obtained from spin coupled valence bond calculations. See text for details

opposite, no-overlapping end of a benzene ring) would give rise to an attractive barrierless interaction. At short range, then, an avoided crossing between the two doublet curves occurs which signals the spin transition leading to bond formation: note that this can lead only to a metastable state if surface reconstruction is not allowed, as indeed found in DFT calculations. The overall correlation diagram, with full geometrical relaxation, as obtained from spin coupled valence bond calculations on the H-benzene model system is shown in fig.3.11. Actually, in this case the situation is a bit more complicated since a slightly lowering state in the triplet manifold (obtained by spin flipping the above spin-excited Dewar-like structure) contributes to the same doublet manifold, but the general consideration on the reaction should still hold.

Chapter 4

Multiple Hydrogen Atoms Adsorption

In this chapter we consider the adsorption of a second, a third and a fourth hydrogen atoms in order to extract general considerations about the chemisorption of an arbitrary number of adsorbates. The adsorption process changes radically depending whether or not the second hydrogen impinges on the sublattice that supports the midgap state. In the first case the final structure is non-magnetic, while in the latter case the two midgap states couples ferromagnetically.
The second adsorption reaction shows high selectivity due to preferential sticking phenomena, induced by the spin density. Larger clusters have been found [114], and their formation might be important as nucleation step for graphene's full hydrogenation. Strangely no *meta* pairs, and more generally no clusters with all the adsorbate lying on the same sublattice have ever been noticed. This might have important implications in the preparation of graphene's fully hydrogenated phase known as graphane.

4.1 Second Atom Adsorption

We consider here the adsorption of a second hydrogen atom on the different sites belonging the two sublattices. The chosen sites are shown in fig.4.1, together with their numbering: the first adsorbed H atom sits on site $A(0)$, indicating the zeroth position of the A sublattice. Other carbon atoms are identified by a letter representing the sublattice and a progressive number. Following analogous notation recently introduced for defects by Palacios *et al.* [96], we use the 'chemical

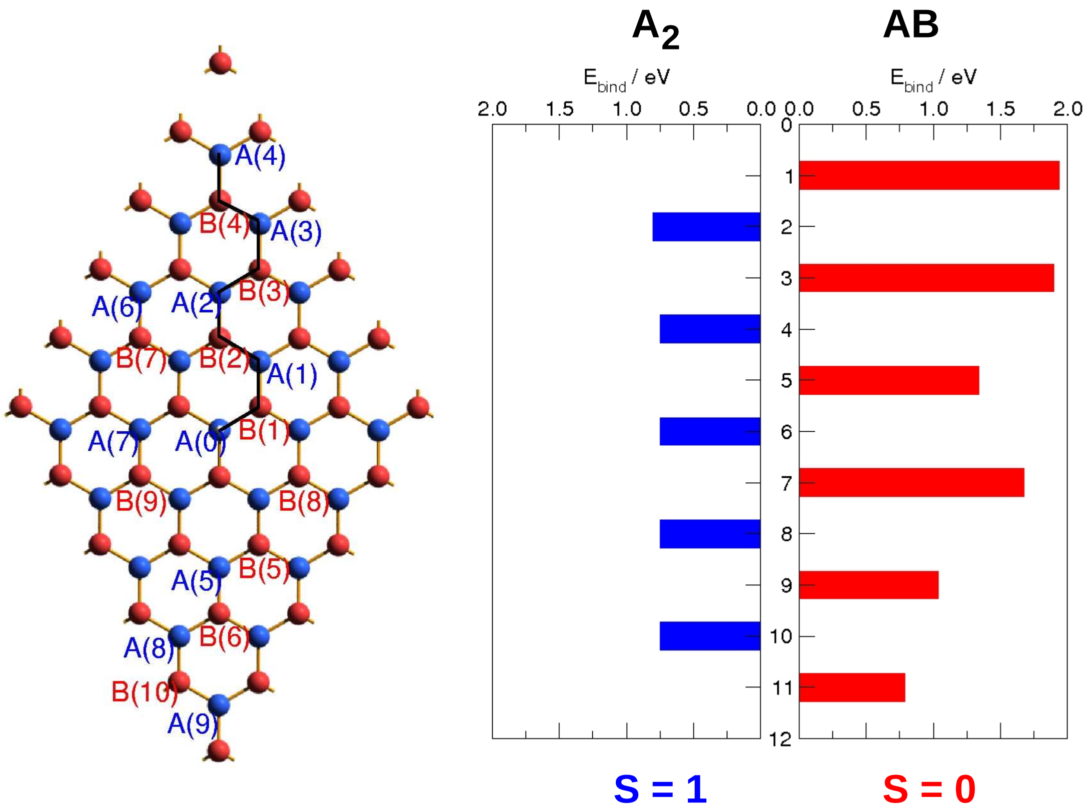

Figure 4.1: Right panel: The graphene 5x5 supercell used in DFT calculations. The first hydrogen atom is adsorbed at the cell central position. Here the A sublattice (blue) contains the first adsorbate while B (red) bears the midgap state. Each position in the cell is identified by the sublattice letter and a progressive number. Left panel: binding energies for A_2 and AB pairs as a function of the distance from the first hydrogen atom.

formula' A_nB_m to denote a cluster with n H atoms in the A lattice and m H atoms in the B lattice.

For each site we have investigated the ground state spin manifold by allowing full relaxation of the magnetization. In addition, in most of the cases, we have also performed magnetization-constrained calculations in order to get insights on both the singlet and the triplet states arising from the interaction between the doublet H-graphene ground-state and the second H atom. Every structure has been relaxed to its equilibrium geometrical structure.

The first hydrogen sits on an A sublattice site, hence the second hydrogen adsorption can occur an a B site to form an AB dimer, or on another A site to form an A_2 dimer. The results for the binding energies are reported in table 4.1

Position	M_{SI} / μ_B	E_{bind} / eV	M/μ_B	E^*_{bind} / eV
B(1)	0.109	1.934	0	0.933
A(1)	-0.019	0.802	2	0.575
B(2)	0.085	1.894	0	0.828
A(2)	-0.017	0.749	2	0.531
B(3)	0.040	1.338	0	0.646
A(3)	-0.016	0.747	2	0.570
B(4)	0.076	1.674	0	-
A(4)	-0.016	0.747	2	0.573
B(5)	0.023	1.033	0	0.590
A(5)	-0.014	0.749	2	0.531
B(6)	0.028	1.110	0	0.545
A(6)	-0.015	0.787	2	-

Table 4.1: Binding energies (E_{bind}) for secondary adsorption to form the H-pairs from H-graphene for sites as shown in fig.4.1, along with the site-integrated magnetizations (M_{SI}) before adsorption, and the total ground-state magnetization (M) after adsorption obtained when fully relaxing the magnetization. Also reported the binding energies (E^*_{bind}) obtained when the magnetization is constrained to $M = 0,\ 2\,\mu_B$ for A and B sites, respectively. See text for details.

and fig.4.1 along with the site-integrated (M_{SI}) and the total M magnetizations. Site-integrated magnetizations have been obtained by integrating the spin-density on a small cylinder (of radius half of the C-C distance in the lattice) centered on each site, and can be considered a rough measure of the total spin excess available on the site due to the midgap state. This quantity behaves very similar to the spin-density itself, decreasing in magnitude when increasing the distance from the adsorption site, *separately* for each sublattice. Some exceptions are worth noticing, namely the *A(0)-B(4)* pair, and are due to the cumulative effect of next-neighbors images. Notice, however, that despite their possible artificial nature,

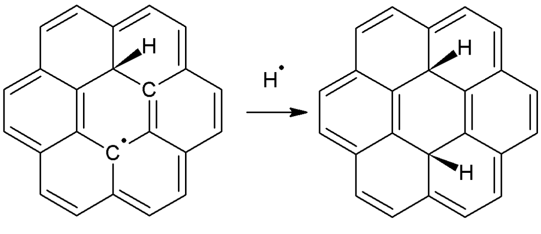

Figure 4.2: closure of the lone electron in the formation of AB dimer.

results corresponding to any lattice sites when viewed *as a function* of the site-integrated magnetization give insights into the adsorption process.
A quick look at the Table 4.1 and fig.4.1 reveals that the two sublattices A and B behave very differently from each other, as the spin-coupling picture of fig.3.10 (panels *b*,*c*) suggests. Roughly speaking, adsorption on B lattice is *preferred* over that on the A lattice. The binding energies are much larger than the first adsorption energy reported in Table 3.1 (they can be as large as twice the adsorption of the first atom), and give rise to a AB pair in a non-magnetized (singlet) state. In contrast, the binding energy for adsorption on a A lattice site is comparable to that of single-H adsorption (0.84 eV), and the ground-state of the A_2 H-pair on graphene is a triplet (M=2 μ_B).
These findings agree with Lieb's theorem 3 for the repulsive Hubbard model of a bipartite lattice and a half-filled band, which states that the ground-state of the system has $S = 1/2|n_A - n_B|$. The lattice imbalance created by hydrogen adsorption can then be filled with an AB dimer, restoring the balance $n_A = n_B$ to a singlet ground state, otherwise enhanced by an A_2 pair with a triplet $S = 1/2|n_A - n_B| = 1$ with triplet ground state.
The results are also consistent with the VB model introduced in section 3.4: with reference to fig.4.2, it is clear that when a H atom adsorbs on a B site its electron readily couples with the unpaired electron available on the B sublattice, whereas when adsorption occurs on an A site another of the double bond of graphene's π network has to break, in the same fashion as for the first adsorption. So, for A_2 hydrogen dimers *two* electrons are left in excess on the B sublattice, and they more favorably couple at high spin.

4.1.1 Spin-Density Dependent Adsorption

The relationship between the available unpaired electron density at a given site and the binding energy of the second H atom can be made clearer by reporting the energy data of Table 4.1 as a function of M_{SI}. This is shown in Fig.4.3, for both the singlet and triplet states of the dimers, along with the value for the first H adsorption (data point at M_{SI}=0). It is clear from the figure that a linear relationship between the binding energy and the site integrated magnetization well describes the situation, and the binding energy for single H adsorption also fits well to this picture.

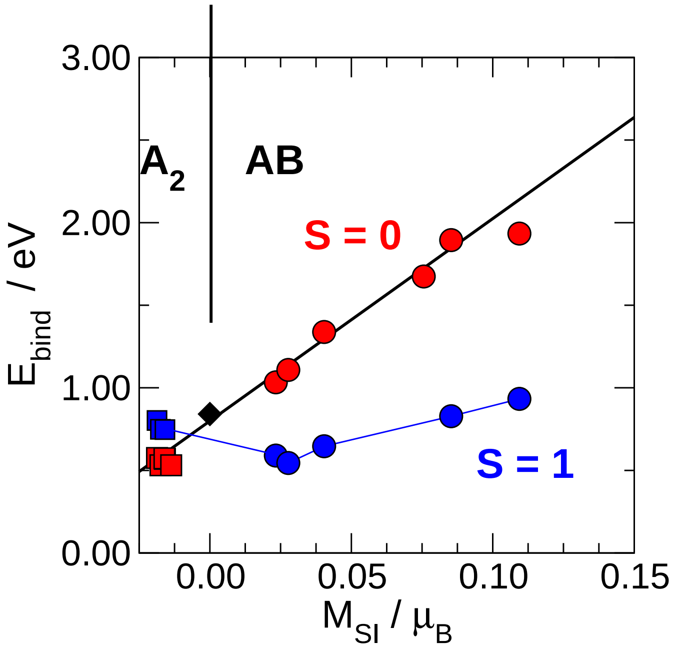

Figure 4.3: Right panel: Binding energies for secondary H adsorption as a function of the site-integrated magnetization (M_{SI}), for *AB* (circles) and A_2 (squares) dimers. Both singlet (red) and triplet (blue) solutions are shown in red and blue respectively. Also shown the data point for single H adsorption (black diamond) and a linear fit to the data set (solid line).

This is again consistent with the chemical model, as long as the site-integrated magnetization is a valid measure of the unpaired electron density available on each adsorption site. According to Section 3.4, adsorption of the first hydrogen atom arises from the energy balance between a 'localization energy' (the spin excitation needed to set free an unpaired electron on the given lattice site), the spin-pairing forming the bond, and the surface reconstruction energy. The same is true for adsorption of a second atom: localization energy takes only a slightly different form than before because an unpaired electron is already available in one of the two sublattices, but surface reconstruction energy is *not* expected to depend strongly on the adsorption site (at least out from the first few nearest neighbours positions, ortho, meta and para). Then, adsorption energies depend on the electronic properties only, and the linear behavior observed for singlet-state dimers in fig.4.3 suggests that the energy needed to localize the unpaired electron on a given site decreases *linearly* when increasing the unpaired electron density available. Notice that negative values of M_{SI} (as found at *A* sites), correspond to a spin excess *parallel* to that of the incoming H electron, and for these sites

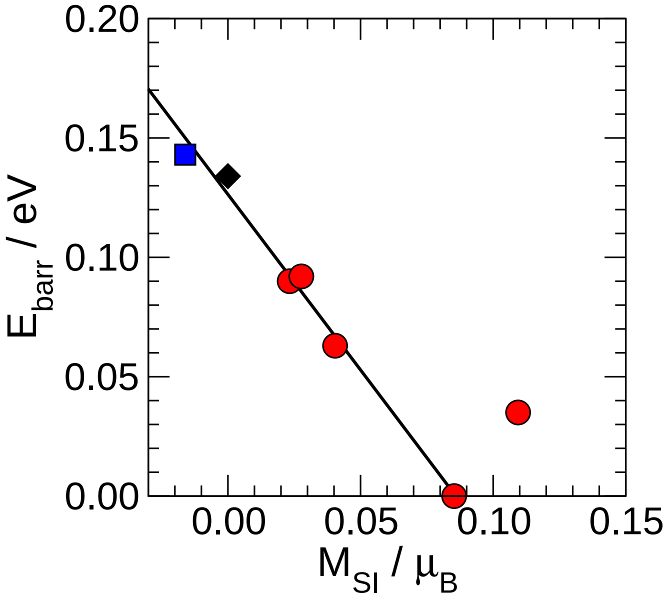

Figure 4.4: Barrier energies for secondary atom adsorption as a function of the site-integrated magnetization. Linear regression (solid line) includes all data, with the exception of the value of the *ortho* dimer (rightmost point in the graph). Data point at M_{SI}=0 is for single H adsorption. Color codes follow fig.4.3.

localization of an unpaired electron with an *anti-parallel* spin requires increasingly more energy when the (magnitude of the) spin-density increases, since this can only be achieved by adding one electron to the site. On the other hand, when a triplet dimer is formed upon adsorption the H electron does *not* make use of the unpaired electron available, and adsorption energies are all around ~0.8 eV, *i.e.* of the order of the first H adsorption. A significant effect of surface relaxation is only seen in forming the $(A(0)B(1))$ *ortho*-dimer, where few tenths of eV more than the single H relaxation energy are required because of the closeness (hence the steric hindrance) of the two hydrogen atoms and of the lattice strain given by two neighbouring sp^3 carbons (see fig.4.5). As result it deviates from the linear trend to lower binding energies as it can be noticed from fig.4.3.

Analogous linear behavior can be found when considering the computed energy barrier to sticking as a function of the site-integrated magnetization, as shown in fig.4.4 for a number of dimers (in their ground electronic state). This agrees with the above localization energy and with the common tendency for a linear relationship between the binding and the barrier energies for activated chemical reactions (Brønsted-Evans-Polayni rule), the only exception being the *ortho*-dimer

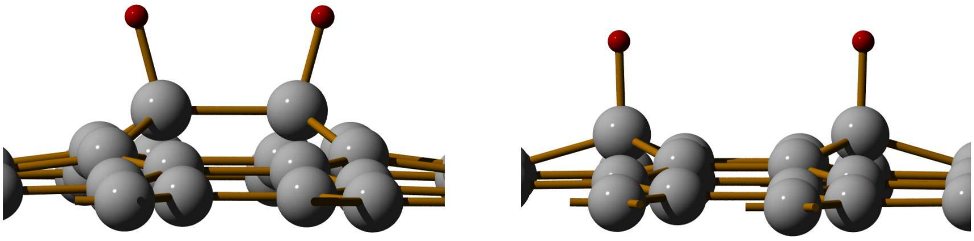

Figure 4.5: Equilibrium geometry for ortho (left) and para (right) dimer structures

considered above. In agreement to previous theoretical studies we find that the *para*-dimer ($A(0)B(2)$) shows no barrier to adsorption thereby supporting a preferential sticking mechanism. This mechanism was first suggested by Hornekær *et al.* [101] who looked at the STM images formed by exposing Highly Oriented Pyrrolitic Graphite (HOPG) samples to a high-energy (1600-2000 K) H atom beam and observed formation of stable pairs, confirmed by *first-principles* calculations [115, 101].

We therefore find that formation of AB dimers is both thermodynamically *and* kinetically favored over formation of A_2 dimers and single atom adsorption. This agrees with current experimental observations which show evidence for clustering of hydrogen atoms at all but very low ($< 1\%$) coverage conditions. In addition, we notice that the dimers experimentally identified so far [116, 101, 114, 107] are all of the AB type.

4.1.2 Facial Selectivity: Syn vs. Anti Adsorption

Recent studies suggested that respect to the second hydrogen atom adsorption the two faces of graphene show a different reactivity. This would be a situation similar to π facial selectivity known in some organic reactions in which preferential attack on one of reactant's "faces" drives towards a given product diastereoisomer. The two isomers are known as *syn*- or *anti*- if respectively the same or the opposite face is preferred: here we will follow the same nomenclature addressing hydrogen pairs sitting on the same graphene face as syn-dimers and as anti-dimers otherwise.

Boukhvalov and Katsnelson [117] studied this problem using *first principles* cal-

Position	E_{bind} / eV	M/μ_B	E^*_{bind} / eV
B(1)	2.430	0	1.371
A(1)	0.738	2	0.551
B(2)	1.668	0	0.604
A(2)	0.784	2	0.560
B(3)	1.343	0	0.590
B(5)	1.208	0	0.716
B(6)	1.230	0	0.637

Table 4.2: Binding energies (E_{bind}) for secondary adsorption to form *anti* H pairs together with the ground state magnetization M and the binding energies (E^*_{bind}) obtained when the magnetization is constrained to $M = 0$, 2 μ_B for A and B sites, respectively.

culations and found a significant difference in the binding energies of syn and anti dimers on graphene: according to them the latter should be more stable then the former for both AB and A_2 pairs. We then performed calculations to check whether or not graphene's faces show different reactivity and the results are shown in fig.4.6 and in table 4.2. Overall our calculations confirm that generally anti dimers are more stable respect to syn ones. At short range syn-dimers are more favorable, hence the H-H steric repulsion cannot be the dominant effect. Probably here is the lattice strain induced by the puckering of the first adsorption that influences the most the dimer formation, contrary to what said for syn dimers, where reconstruction energy is almost site-independent.

This can be better understood looking at the geometry of the cyclohexane molecule. Cyclohexane minimum geometry is the so-called chair configuration: very similar to carbon backbone structure in the syn-meta dimer. Starting from a planar structure the chair is obtained by puckering in opposite out-of-plane directions two groups of carbons in meta position to each other. In this geometry all the sp^3 carbons are perfectly tetrahedral, minimizing the structural stress, and the axial hydrogens of the two groups point in opposite directions lowering their repulsion. In the same fashion the syn-para dimer is analogous to the boat geometry, another situation of minimal angular strain in cyclohexane, hence syn-dimers are favorite for short range dimers. An exception is the syn-ortho pair where the two hydrogens are very close to each other and their steric repulsion is quite strong. The anti-ortho pair does not show any unfavorable steric effect, so it turns to be more stable.

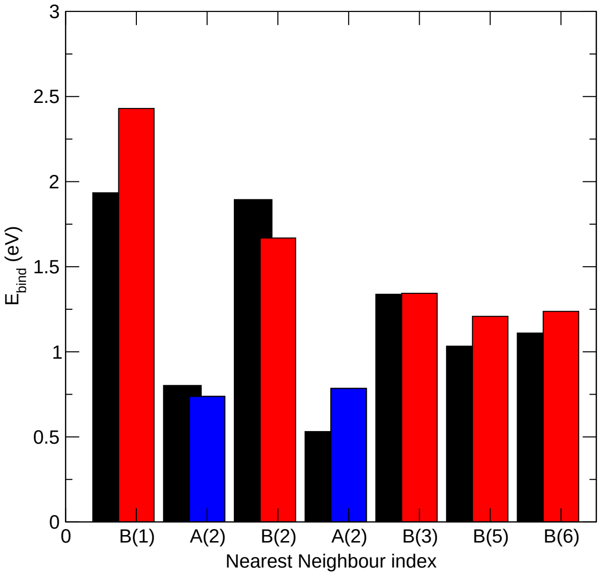

Figure 4.6: Binding energies comparison for hydrogen dimers formation on graphene: *syn*-dimers (black bars) are generally less stable then *anti*-dimers (red bars) with exception of the *meta* and *para* geometries.

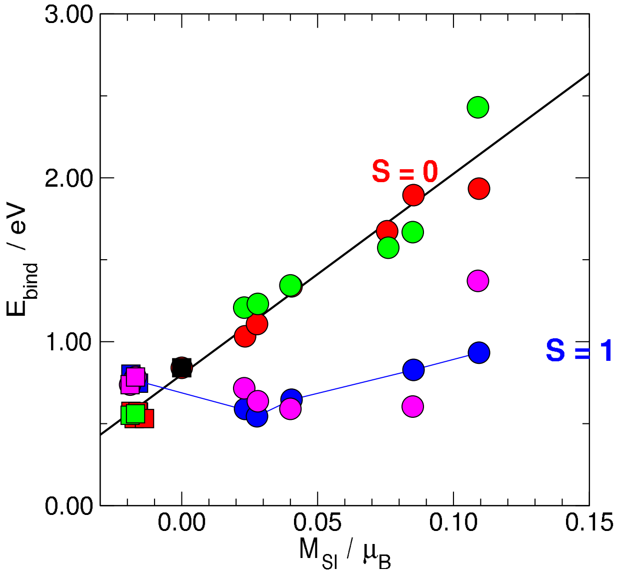

Figure 4.7: Binding energies for *syn* and *anti* dimers as a comparison with fig.4.3 Circles are *AB* while squares are A_2 dimers: red (green) are syn (anti) dimers with a singlet ground state while blue (magenta) are syn (anti) dimers with triplet ground state.

The stress induced by the first chemisorption puckering fades away with the distance, so the H-H repulsion becomes dominant and anti-dimers are preferred for longer range pairs; the crossover between this two regimes takes place at the $AB(3)$ dimer. Note that the preferential adsorption on the anti- face should disappear with the increase of the hydrogen - hydrogen distance since the two cases, syn and anti, should have the same energy: strangely this preference is still effective up to the $AB(6)$ pair (dHH=5.6 Å). This suggest that some other adsorbate mediated effect might take place and that further investigation is then needed.
Comparing syn and anti dimers binding energies is possible to notice form fig.4.7 how they both follow the same linear trend respect to the local magnetization as shown before in section 4.1, moreover their density of states are practically identical [118]. This suggests that the electronic (valence bond) arguments and preferential chemisorption to form AB pairs, applied before for syn-dimers hold also for the anti configuration.

4.2 Density of States for Hydrogen Dimers Structures

The density of states for AB and A_2 dimers on graphene are of course very different. Magnetized A_2 dimers have, of course, two sublattices imbalances and so, according to theorem 1 two midgap states. This two flat bands should lay at zero (Fermi) energy but being of the same spin projection they are split due to exchange interaction. When considering A_2 pairs at larger and larger H-H separation the two midgap states tend to coalesce into a single one, situation achieved when the two adsorbate are so far to be considered as isolated (fig4.9).

For AB pairs the DOS are more complex to interpret. Generally there is a band gap but in some cases the band structure turns to be again semi-metallic as in pure graphene. Is also possible to notice two broad features close to the Fermi energy: they also tend to detach from the rest of the valence (conduction) band to coalesce and give rise to a midgap state in the limit of isolated defects. We believe that these features come from the interaction between midgap states. This is shown in fig.4.8. Using a simple qualitative picture the two flat-bands act as two orbitals, one for each adsorbate state that in this case can interact together forming a sort of bonding-anti bonding molecular orbitals. The result

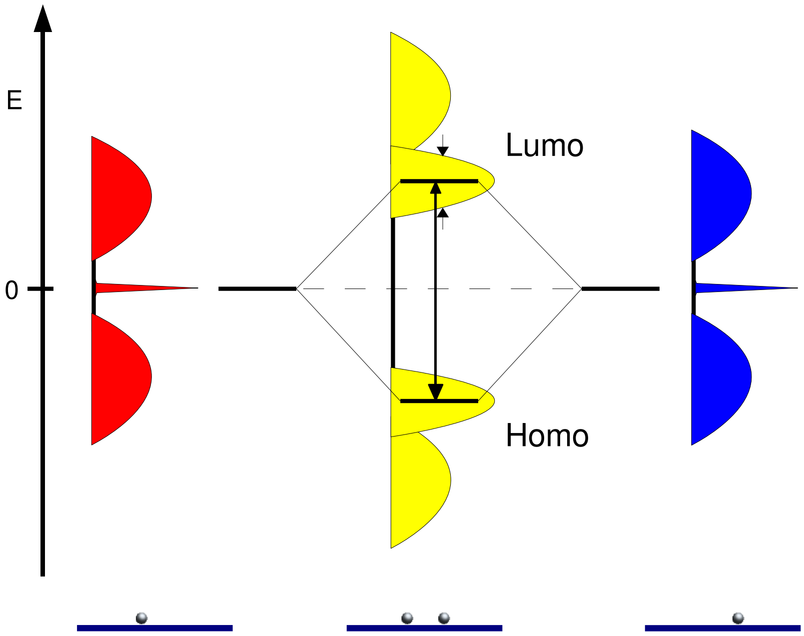

Figure 4.8: Model DOS for AB dimers. Two midgap states coming from two separate hydrogen defects interacts restoring the aromaticity on graphene. The sharp state splits and broaden proportionally to the interaction between the midgap states.

are π-π^* bands that restore sublattice balance and aromaticity of graphene, so for semiconducting dimers structure this two states act as the HOMO-LUMO pair in benzene. As a consequence, the HOMO-LUMO levels broadens and splits in energy proportionally with the interaction strength, that reasonably scales as the midgap states decay in space. Indeed the charge density associated with this feature has the same symmetry of the HOMO and LUMO orbitals of the benzene molecule.

In order to understand what makes a dimers structure semi metallic, we used a tight-binding approach that allows to check the band structure of a large number of AB dimers using super-cells with hundreds of atoms.

Our calculations show how only the symmetric dimers arrangements have a semimetallic density of states, due to the shift of the Dirac cones away from $\mathbf{K}$ and $\mathbf{K}'$, as shown in fig.4.10 for $AB(1)$ (ortho) and fig.4.11 for $AB(2)$ (para) dimers. The degeneracy that produces the conical intersection at the Fermi energy in graphene is a direct consequence of graphene symmetry: a general arrangement of hydrogen dimers would destroy most of the symmetry elements, so the Dirac cones. When the dimers are arranged along some of these elements *e.g.* a mirror

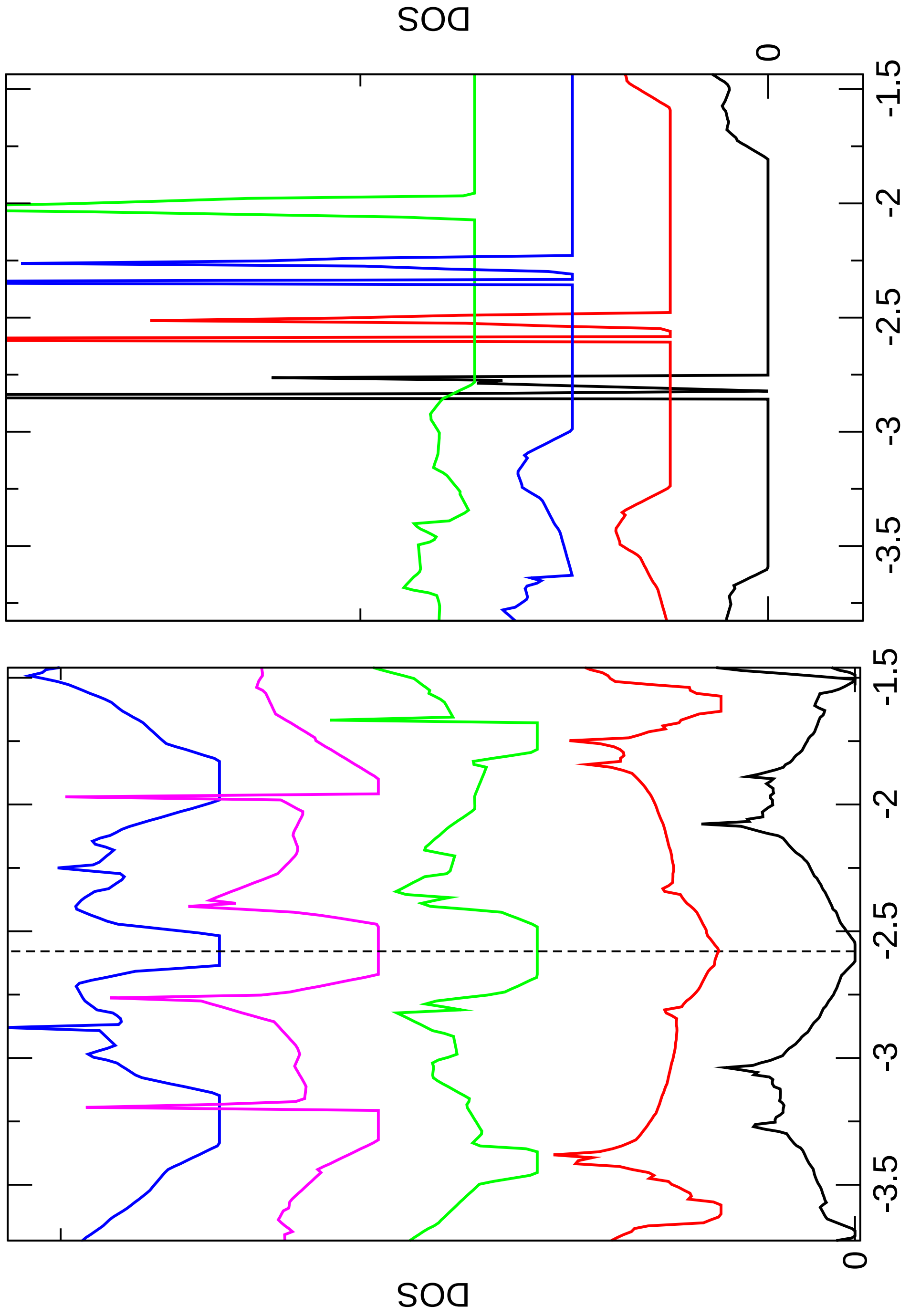

Figure 4.9: Density of states for selected AB (left) and A_2 dimers at crescent H-H distance (along the y axis). Note how ony some of the AB ones show a band gap, while the ortho and para (black and red curves) being symmetrical are semi-metallic

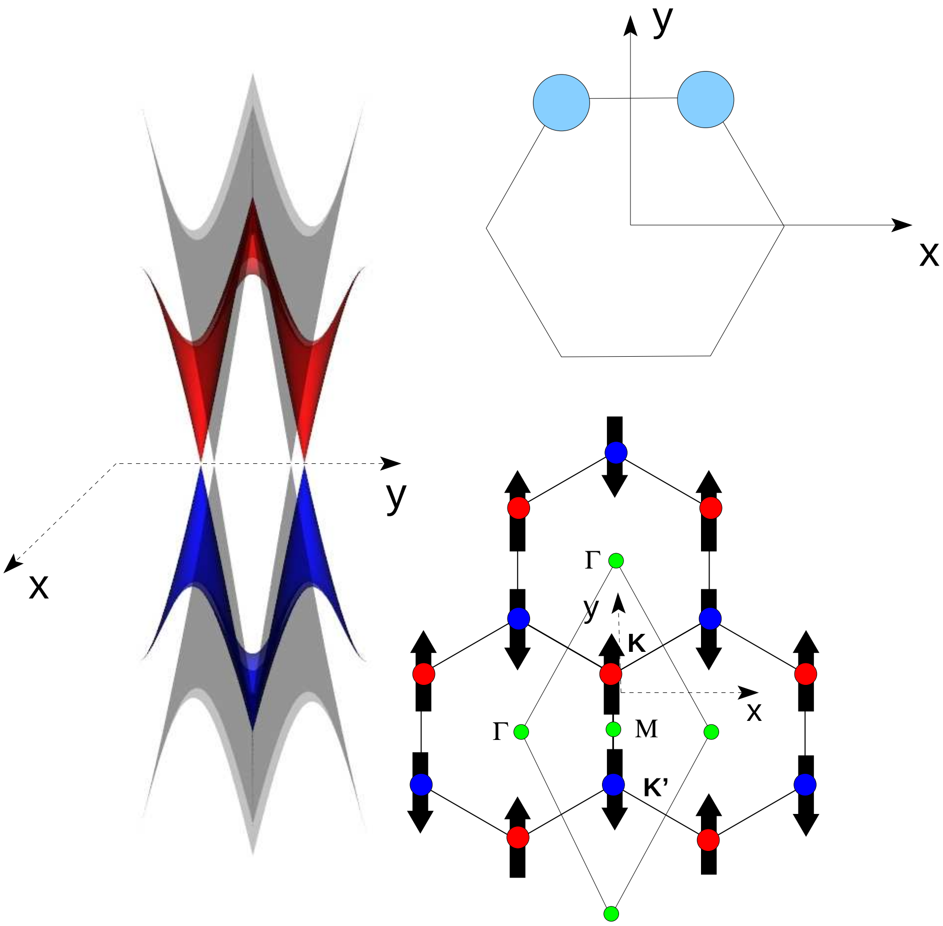

Figure 4.10: Band structure for $AB(1)$ (ortho) dimer superimposed to the $\pi - \pi^*$ bands of pure graphene (red and blue). The shift of the Dirac points in the Brillouin zone is also shown.

plane, this is be preserved perturbing the cones, but not destroying them. In the case of ortho and para dimers, adsorbates lays along σ_v planes, elements of the D_{6h} point group, that are not modified by them. Indeed looking at the band structure (fig.4.10 and fig.4.11) the Dirac cones shifts away symmetrically from $\mathbf{K}$ according to this mirror plane. To support this result is worth mentioning that this effect on the Dirac cones is actually very similar to the shift induced in graphene by the transverse phonon with the same symmetry [11].

4.3 Further Adsorptions

We consider in this section results concerning formation of clusters of three and four atoms. From the interpretation of STM images it has been noticed the

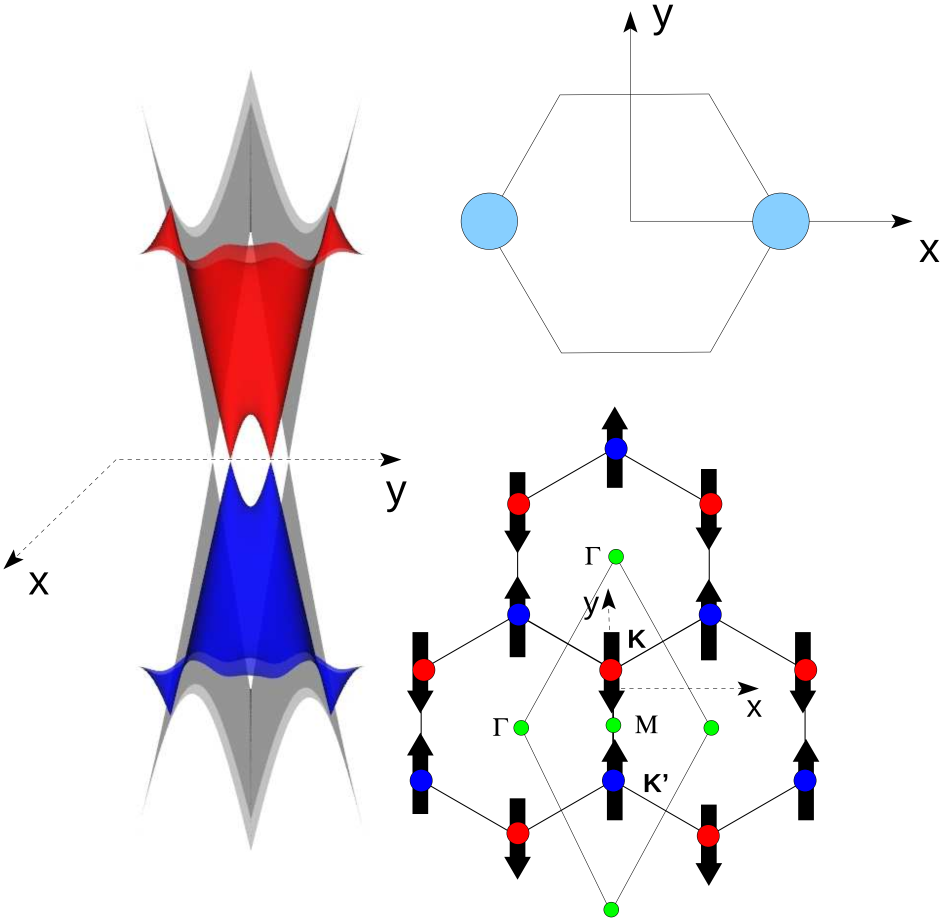

Figure 4.11: Band structure for $AB(2)$ (para) dimer superimposed to the $\pi - \pi^*$ bands of pure graphene (red and blue). The shift of the Dirac points in the Brillouin zone is also shown.

Position	E_{bind} / eV
A(2)	1.516
B(3)	0.847
A(3)	0.727
B(4) (≡A(5))	0.971
A(4) (≡B(6))	0.821
B(7)	0.727
B(8)	1.301

Table 4.3: Binding energies (E_{bind}) for addition of a third H atom to the AB *para* dimer structure $A(0)B(2)$ on the sites indicated in the first column (labels from fig.4.1).

	M_{SI} / μ_B	E_{bind} / eV	M/μ_B
$B(9)$	-0.0180	1.103	2
$A(7)$	0.0471	1.331	0
$B(6)$	-0.0151	0.727	2
$A(8)$	0.0325	1.210	0
$B(10)$	-0.0134	0.723	2
$A(9)$	0.0326	1.201	0

Table 4.4: Binding (E_{bind}) energies for adsorption to form H-quadruples from the $A(0)B(2)B(8)$ cluster, along with the site-integrated magnetizations (M_{SI}) and the total ground-state magnetization (M), before and after adsorption, respectively. See Fig.4.1 for atom labels.

presence of clusters up to six atoms H atoms on graphite surfaces, although this is still a matter of debate [119, 120]. With more and more hydrogen atoms to arrange on graphene or graphite the number of possible arrangements grows quickly, therefore we limit our analysis to a few important geometries. According to theorems 1 and 3 and to the π resonance picture, we expect that the ground electronic state of a generic A_nB_m cluster has $|n-m|$ unpaired electrons, each of them lying in a midgap state. We have considered a number of A_2B_2, A_2B, A_3B_1 and A_3 clusters, and found that their ground-state has 0, 1, 2 and 3 μ_B of magnetization, respectively, in agreement with the expectation. Three atom clusters have been obtained by adding one hydrogen atom either to a *para* dimer or to a *meta* dimer, i.e. $A(0)B(2)$ and $A(0)A(1)$ following labels of fig.4.1, respectively. The binding energies of a third hydrogen atom to a *para* dimer structure are reported in Tab.4.3; since they all are of A_2B (or AB_2) type, the total magnetization for the resulting structures is 1 μ_B. A look at Tab.4.3 reveals that adsorption to a third hydrogen atom parallels that of the first H. This is consistent with the π resonance picture, since AB dimers do not have unpaired electrons, and therefore show no preference towards any specific sublattice position. There are of course exceptions, notably the values for adsorption onto $A(2)$ and $B(8)$ lattice sites, and these can be reasonably ascribed to the effect of surface relaxation. Indeed, relaxation energies per atom in 'compact' clusters may considerably differ from the value of the single H atom, being always of the order of the binding energies themselves ($\sim$ 0.8 eV). Similar conclusions hold when adding a third H atom to the (magnetic) *meta* dimer $A(0)A(1)$: adsorption on B lattice sites is strongly favored ($E_{bind} = 1.2-1.9$ eV) and produces doublet structures ($M = 1\,\mu_B$), whereas

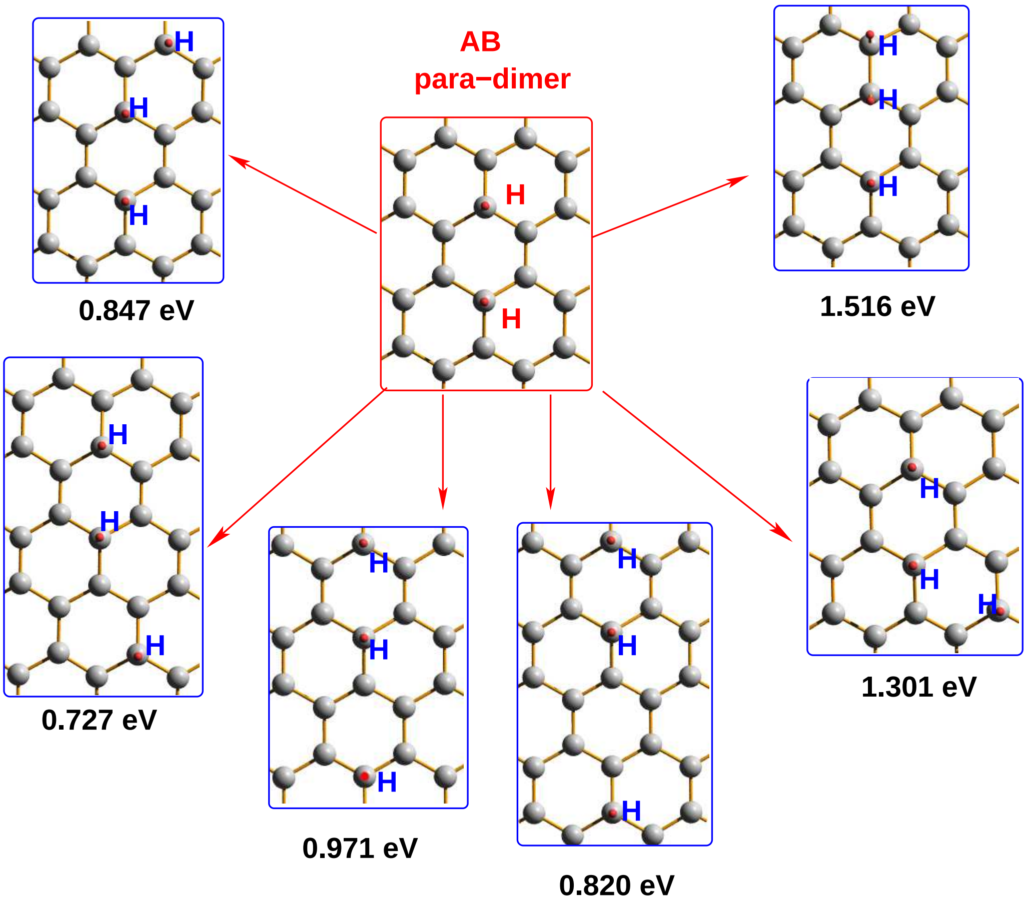

Figure 4.12: Some of the possible hydrogen trimers structures obtainable from theAB para dimer. Binding energies are also shown.

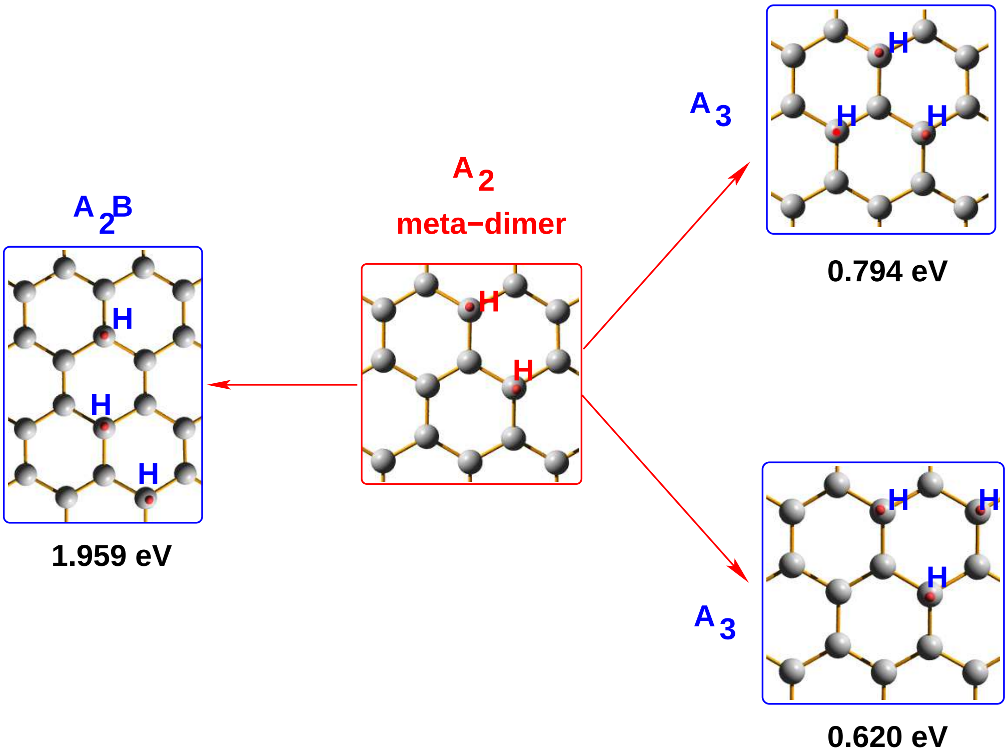

Figure 4.13: Some of the possible hydrogen trimers structures obtainable from the A_2 meta dimer. Binding energies are also shown

H atoms bind to A lattice sites with an energy $\sim 0.7 - 0.8$ eV and produce highly magnetic structures ($M = 3\,\mu_B$).

Energy barriers to adsorption follow the same trend: calculations show that, with few exceptions, barriers to sticking a third H atom compare rather well with that for single H atom adsorption for the processes $AB \rightarrow A_2B$ and $A_2 \rightarrow A_3$, and may be considerably smaller for $A_2 \rightarrow A_2B$ ones. In addition, and again consistently with π resonance picture, we found that all the considered 3-atom structures, with one or three unpaired electrons, show an alternation pattern in their spin-density maps. As an example, fig.4.14 reports the spin-density maps for an A_2B (left panel) and an A_3 (right panel) cluster. Analogously to subsection 4.1 we find that analysis of these spin-density maps gives insights to the adsorption properties of a fourth hydrogen atom. Table 4.4, for example, reports binding energies to form some 4-atom clusters from the stable $A(0)B(2)B(8)$ one, the final total magnetization of the resulting structures and the values of the corresponding site-integrated magnetization before adsorption. The computed binding and barrier energies compare rather well with the dimer values, as can be seen in fig.4.15

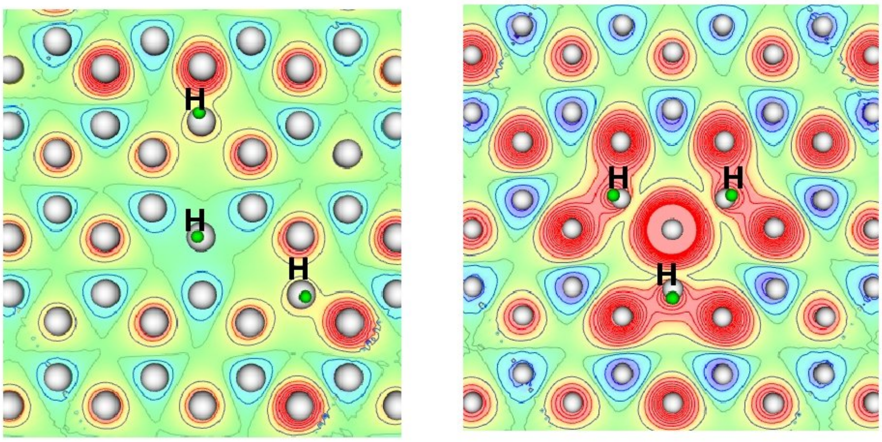

Figure 4.14: (Color online) Spin-density 0.40 Å above the surface for two three-atom clusters. Contour map with red/blue lines for spin-up/spin-down excess respectively. Left and right panel for an A_2B and a A_3 cluster, respectively.

where it is clear that the results fit well to the *same* linear trends obtained before. Few exceptions are for compact clusters where substrate relaxation does play some role. With such exceptions in mind, our results suggest that adsorption of hydrogen atoms on magnetic graphitic substrates (such as those obtained by adsorbing any odd number of H atoms), for a given final spin-state, depends on the local spin-density only.

4.4 A Route to Graphane?

Graphane is a novel two-dimensional material, namely the fully hydrogenated graphene sheet as shown in fig.4.16. The structure is still a bipartite lattice in which each sublattice bears hydrogens all on the *same* side of the lattice plane, and overall it has show a chair-like structure as in cyclohexane.

Graphane is an insulating material with no π electrons [121], that has been recently obtained by simply exposing graphene to cold hydrogen plasma [122]. This result is very interesting at the light of what shown in the previous sections: in order to produce graphane by simple hydrogen plasma exposure it is necessary either that H atoms adsorb selectively on *only* one sublattice for a given graphene face or that hydrogen diffuses to occupy these sites.

We showed in section 4.1.2 that after a first chemisorption on a given sublattice,

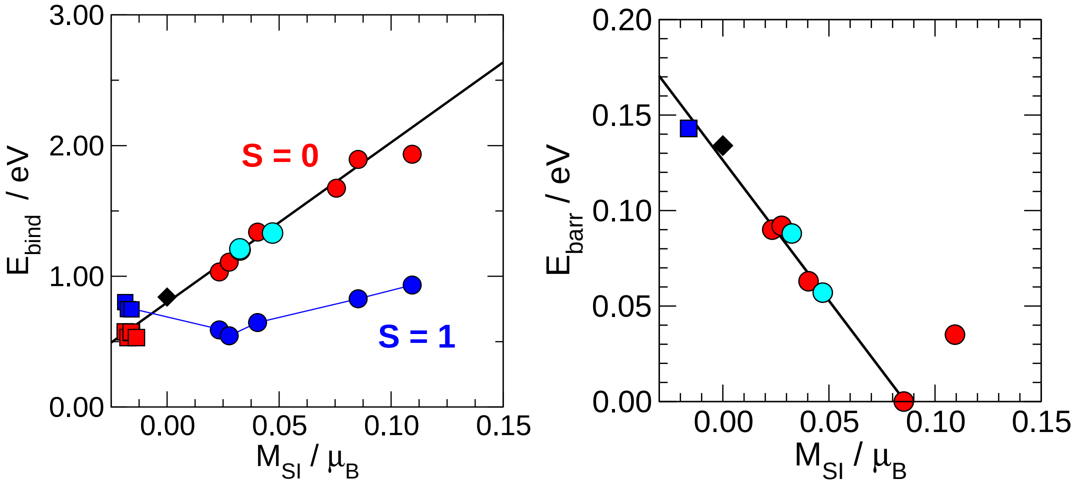

Figure 4.15: Same as in fig.4.3 for binding energies and in fig.4.4 for barrier energies for the formation a non-magnetic (A_2B_2) four atoms cluster from the three atoms cluster $A(0)B(2)B(8)$ (cyan circles).

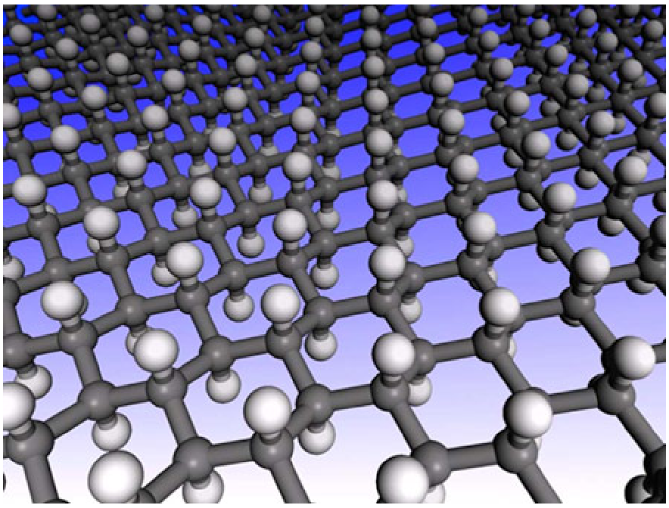

Figure 4.16: Graphane lattice structure from [121]. Hydrogen atoms are bonded to carbon on both sides of the plane in an alternating manner.

preferential sticking occurs on the opposite sublattice both for syn- and anti-dimers. The syn-meta formation is not very probable process but the anti-para dimer formation is barrierless and it may be a good first step for graphane formation. Unfortunately after para dimer formation there is no more spin-density on graphene, hence no preferential sticking. Being now adsorption on any other site more or less equally probable, it will be very difficult that all the other hydrogens will chemisorbed in the correct sites. Moreover it is known that hydrogen surface diffusion is highly inefficient since is competitive with desorption, that has a lower activation energy [116]: for this reasons we believe that some other effect has to play a role in thermal graphane synthesis from graphene. Other recent *first principles* and molecular dynamics studies seems to confirm our findings: that formation of disordered hydrogenated domains should be favored respect to graphane [123].

Curved graphene areas might help this process. Graphene is a very elastic membrane that naturally exhibit ripples that tend naturally to lay down along steps and kinks of the support surface on which it was grown. Indeed recent experimental findings suggested that hydrogen chemisorbs more efficiently on the ridges of the silicon carbide substrate surface onto which graphene usually lays [124]. Moreover, it has been also shown that hydrogenation of single-layer graphene is much easier that for the many-layer graphene, whereas the first is much more corrugated then the latter (see sec.1.1.1)[125, 126]. This is reasonable, as for nanotubes the curvature reduces the p_z-p_z overlap, *i.e.* aromaticity, lowering both barrier and binding energy for H chemisorption[127, 128]. Still, there is not any evidence that local curvature plays a role in graphane formation, and more investigations in this direction are needed.

Chapter 5

Eley-Rideal Hydrogen Recombination on Graphite

After the study of the hydrogen - graphene interaction in this chapter we show the results of a quantum wave packet dynamical study of the recombination of hydrogen atoms on graphene and graphite surfaces to give H_2 molecules via the Eley-Rideal mechanism. This approach uses DFT potential energy surfaces to represent the gas-surface interaction, and a fully quantum approach to the dynamical simulation. Here we assumed that the hydrogen-sp^2 carbon for rather flat surfaces is universal, hence a graphene surface will be used also as a model for graphite's Bernal surface($\{0001\}$).
In particular this study focuses on the low collision energy regime, a range of energies particularly difficult to study with standard approaches. For this reason we used a novel scheme that allows simulations down to very low collision energies, although here we will not stress the technical side, but rather the results and their implication for the interstellar medium (ISM) chemistry.

5.1 Introduction

In recent years, there has been an increased interest in studying atomic hydrogen recombination on graphitic surfaces. This interest is largely due to the relevance of hydrogen-graphite systems for understanding hydrogen formation in the interstellar medium (ISM), as introduced in sec.1.5.2. Depending on the physical conditions of interest and on the actual morphology of the surface, a number of formation processes are possible, but usually only the prototypical Eley-Rideal and Langmuir-Hinshelwood mechanisms are taken into account. Both this pathways require that at least one hydrogen atom adsorbs on the graphitic surface. The Eley-Rideal mechanism can involve both chemi- of physisorbed atoms on the surface, while the Langmuir-Hinshelwood one implies the diffusion of strongly bonded (thermalized) adsorbates. Unfortunately the presence of the activation barrier to chemisorption shown in sec.3.3 essentially prevents (direct) hydrogen sticking in the chemisorption well at temperatures typical of the ISM clouds. However, hydrogen chemisorption is needed to explain molecular formation in photon-dominated and shocked regions of ISM, where the temperature is much higher than the desorbing temperature of physisorbed species.

At temperatures high enough for first H adsorption to occur, hydrogen dimers can be formed through barrierless sticking of a H atom close to a previously adsorbed one, to form the *para* dimer (sec.4.1) [116, 115]. In this way, molecular formation may follow recombination of hydrogen pairs in the para position of a hexagonal ring, in addition to direct (Eley-Rideal) abstraction. At low temperature, however, not much is known but it is expected that formation of hydrogen molecules from chemisorbed species cannot occur. Even if a hydrogen atom is already chemisorbed on the surface, direct Eley-Rideal recombination would hardly occur in the temperature range 1-100 K. On the other hand, physisorption of hydrogen atoms may occur at very low energy and leads to formation of weakly bound species far apart from the surface (at about 4 Å). In this case, DFT calculations are not accurate enough to describe the interaction and the physisorption binding energy has been estimated to be ∼40 meV by selective adsorption experiments [129], in good agreement with recent correlated calculations [89]. Thus, H_2 formation in diffuse clouds probably involves physisorbed species, and may occur through any of the main gas-surface mechanisms: namely the Langmuir-Hinshelwood, or an Eley-Rideal, or a hot-atom mechanism, or a combination of them.

The Eley-Rideal (ER) reaction mechanism consists in an atom coming from the gas phase that impinges on another atom adsorbed on the surface, reacting to form a diatomic product molecule that desorbes back to the gas phase. This mechanism has been recently studied in laboratory for H recombination on graphite surfaces [130, 131], and product ro-vibrational excitation has been found. Although no data are available at the low temperatures of the ISM, for this reason in our study we will focus on this particular mechanism at low collision energies. We will also present results about other non-dynamical processes, such as trapping of the projectile on the surface.

5.2 Theoretical Methods

In order to simulate the dyanamics of hydrogen recombination on Bernal graphite and graphene surfaces we used the quantum wave packet approach. Within this model a projectile atom is represented by a wave packet which propagates in time onto a potential energy surface that maps out the atoms-surface interaction. At the end of the dynamics the wave packet is analyzed by a flux operator to extract reaction cross sections, and absorbed by proper imaginary potentials. This method is very useful since it gives state-to-state cross sections for a given reaction at several energies with a single calculation, having a wave packet many different energetic components.

Hydrogen atom is a very good candidate for wave packet dynamics, because a quantal approach can in principle include effects such as tunneling and interference, quite probable when light atoms are involved, moreover the packet can be arranged to represent any definite initial state. Then, after some propagation time, a final analysis stage projects the wave packet onto bound products states, functions giving the state resolved cross sections.

Special care has to be used to the low collision energy regime. The mathematical condition for the the final analysis to be correct requires to have no negative momentum components in the initial wave packet, then the lower the average momentum, the larger will the packet spreading in the coordinates. For this reason it gets more complicated to handle the packet on the numerical grid on which its propagated. To overcome this inconvenient we used a recent technique that allows the use of initial wave packets with arbitrary component and then subtract out the negative momentum part.

5.2.1 The Wave Packet

Wave function is the cornerstone of any theoretical calculation in condensed matter physics, both in electronic structure and in dynamics. In quantum dynamics the wave packet, is a guess function made of a plane waves superposition localized in a point in space. In order to build such a function in one dimension

$\psi(x)$ one chooses the combination coefficients from the inverse Fourier transform[1]

$$\psi(x) = \frac{1}{\sqrt{2\pi}} \int_{-\infty}^{+\infty} \phi(p) e^{ipx} dp \tag{5.1}$$

$$\phi(p) = \frac{1}{2\pi} \int_{-\infty}^{+\infty} \psi(x) e^{-ipx} dx \simeq \tag{5.2}$$

$$\simeq \frac{1}{2\pi} \int_{-L/2}^{+L/2} e^{-i(p-p_0)x} dx = \frac{L}{2\pi} \frac{\sin((p-p_0)L/2)}{(p-p_0)L/2} \tag{5.3}$$

where a cutoff length L has been introduced. More generally it is chosen to use a simple Gaussian function with center in x_0 and width δ, times a plane wave [132]

$$\psi(x_0) = \left(\frac{1}{2\pi\delta^2}\right)^{1/4} e^{-\frac{(x-x_0)}{4\delta^2}} e^{-ip_0x} \tag{5.4}$$

$$\phi(p_0) = \left(\frac{2\delta^2}{\pi}\right)^{1/4} e^{-\delta^2(p-p_0)-i(p-p_0)x} \tag{5.5}$$

The projectile particle is then represented by a wave packet with a finite width: to retrieve the classical limit the wave packet in eq.5.4 has to be shrunk in space in order to localize a particle. Meanwhile its Fourier transform in momentum space will broaden, according to uncertainty principle, but it will still keep its Gaussian shape. Note also that for each momentum component this kind of wave function satisfied the time dependent Schrödinger's equation: in a dynamical simulation is then possible to extract from each component the cross sections for the corresponding momentum p.

5.2.2 The DVR grid

The wave packet is a continuous object that needs to be represented within a numerical procedure in order to simulate the dynamics. A natural choice is to use discrete grids, *i.e.* to expand the wave function on a basis of functions extremely localized on grid points: such a basis, takes the name of Discrete Variable Representation (DVR).

In order to build a generic DVR it is necessary to define a projection operator that maps the wave packet on a finite set of orthogonal functions (grid points)

---

[1] the wave packet's Fourier transform it always exists since any physically reasonable wave function has to be a part of $\mathcal{L}^2$

$\Delta_\alpha(x)$,

$$\hat{P} = \sum_{n=0}^{N-1} |n\rangle \langle n| \tag{5.6}$$

$$|\Delta_\alpha\rangle = \hat{P}\,|x_\alpha\rangle \qquad \Delta_\beta(x_\alpha) = K_\alpha \delta_{\alpha\beta} \tag{5.7}$$

in this way, one can define a normalization

$$\langle \Delta_\alpha | \Delta_\beta \rangle = \langle x_\alpha | P^\dagger P | x_\beta \rangle = \langle x_\alpha | P | x_\beta \rangle = \langle x_\alpha | \Delta_\beta \rangle = K_\alpha \delta_{\alpha\beta}$$

$$|F_\alpha\rangle = \frac{1}{\sqrt{K_\alpha}} |\Delta_\alpha\rangle \tag{5.8}$$

and so is possible to use the grid to represent the wave function as

$$|\psi\rangle = \sum_\alpha |F_\alpha\rangle \langle F_\alpha | \psi \rangle = \sum_\alpha \frac{1}{\sqrt{K_\alpha}} \psi(x_\alpha) |F_\alpha\rangle$$

$$\psi_\alpha^{DVR} = \frac{1}{\sqrt{K_\alpha}} \psi(x_\alpha) \tag{5.9}$$

Here we focus on two important consequences of the choice of a DVR basis, that turn to be computationally very convenient. First, is possible to note that when computing scalar products on a DVR grid, a Gaussian quadrature - like rule is obtained in which the DVR normalization factor plays the role of a (uniform) quadrature weight.

$$\langle \psi | \phi \rangle = \int \psi^*(x)\phi(x)dx = \sum_\alpha \langle \psi | F_\alpha \rangle \langle F_\alpha | \phi \rangle = \sum_\alpha \frac{1}{K_\alpha} \psi^*(x_\alpha)\phi(x_\beta)$$

Several different DVR sets might be built choosing different basis for the projector in eq.5.6. A simple choice is to use a set of plane waves, so momentum eigenfunctions.

$$P = \int_{-p_{max}}^{+p_{max}} |p\rangle \langle p|\, dp \tag{5.10}$$

that, being limited to a certain momentum window they turn to be only *improper* eigenstates. Following the procedure above one gets

$$|\Delta_\alpha\rangle = \int_{-p_{max}}^{+p_{max}} |p\rangle \langle p | x \rangle\, dp = \int_{-p_{max}}^{+p_{max}} |p\rangle \frac{e^{-ipx_\alpha}}{\sqrt{2\pi}} dp$$

$$\langle \Delta_\alpha | \Delta_\beta \rangle = \int_{-p_{max}}^{+p_{max}} |p\rangle \frac{e^{-ip(x_\alpha - x_\beta}}{\sqrt{2\pi}} dp = \frac{p_{max}}{\pi} \delta_{\alpha\beta}$$

$$F_\alpha(x) = \frac{1}{\sqrt{\pi p_{max}}} \frac{\sin(p_{max}(x - x_\alpha))}{(x - x_\alpha)} \tag{5.11}$$

The maximum momentum component representable as $x_\alpha = \pi\alpha/p_{max}$ usually defines the total number of points on a grid (their spacing).

5.2.3 The Propagator

The time evolution of a state vector $|\Psi(\mathbf{x}, t_0)\rangle$ is described by the time dependent Schrödinger's equation

$$H\,|\Psi(\mathbf{x}, t)\rangle = i\frac{\partial}{\partial t}\,|\Psi(\mathbf{x}, t)\rangle \tag{5.12}$$

from which is possible to introduce the time evolution operator that connects the state at time t_0 to its evolution at time t.

$$|\Psi(\mathbf{x}, t)\rangle = U_t(t, t_0)\,|\Psi(\mathbf{x}, t_0)\rangle \tag{5.13}$$

$$H\;U_t(t, t_0) = i\frac{\partial}{\partial t}U_t(t, t_0) \tag{5.14}$$

solving the ordinary differential equation under the initial condition $U_t(t_0, t_0) = 0$ one gets the time-evolution operator

$$U_t(t, t_0) = e^{-iH(t-t_0)} \tag{5.15}$$

Applying the time evolution operator on a state at time t_0 one evaluates exactly such vector at time t whichever is the time interval (t_0, t). In this way to know U_t means to be able to compute *exactly* the outcome of a dynamical event, such as atomic collisions *i.e.* a chemical reaction. This is of course not possible in practice, since $\hat{H}$ is a sparse infinite dimensional matrix and then some approximation has to be done. The several approaches developed to carry on a time evolution are known as propagators. Among them I will show below only the one employed in the quantum scattering code used for this study. More details on the different propagator approaches can be found in [133]

5.2.4 Split Operator Method

This method turns to be very useful in order to evaluate the time evolution for short time steps, and it is based on a particular expansion of U_t[134, 135]. Among the different expansions of non-commuting exponential operators, such as the kinetic $\hat{H}_0$ and the potential V terms, it is possible to use the Suzuki-Trotter formula[136, 137].

$$e^{A+B} = \lim_{n\to\infty}\left(e^{A/n}e^{B/n}\right)^n \tag{5.16}$$

that is equivalent to[138]

$$e^{\lambda(A+B)} = \lim_{\lambda\to 0}\left(e^{\lambda A}e^{\lambda B}\right) \tag{5.17}$$

For the time evolution this reads:

$$e^{-iH\Delta t} = e^{-iH_0\Delta t}e^{-iV\Delta t} + \mathcal{O}(\Delta t^2) \tag{5.18}$$

that at the second order is

$$e^{-iH\Delta t} = e^{-i\frac{H_0}{2}\Delta t}e^{-iV\Delta t}e^{-i\frac{H_0}{2}\Delta t} + S(\Delta t^3) + \mathcal{O}(\Delta t^4) \tag{5.19}$$

in which the reminder $S(t^3)$ follows the expression[2] $[H_0 + 2V, [H_0, V]]t^3/24$. This can be better understood from another point of view, for which is more convenient to use the interaction picture

$$|\Psi_S(t)\rangle = e^{-iH_0\Delta t}\,|\Psi_I(t)\rangle \tag{5.21}$$

$$i\frac{\partial}{\partial t}\,|\Psi_I(t)\rangle = V_I\,|\Psi_I(t)\rangle \tag{5.22}$$

Integrating eq.5.22 on a time interval $[t, t+\Delta t]$

$$\Psi_I(t+\Delta t) = \Psi_I(t) - i\int_t^{t+\Delta t} V_I(t')\Psi_I(t')dt' \tag{5.23}$$

and solving it iteratively, with $\Psi_I(t') = \Psi_I(t+\Delta t)$

$$\Psi_I(t+\Delta t) = \Psi_I(t) - i\int_t^{t+\Delta t} V_I dt' \left(\Psi_I(t) - i\int_t^{t'} dt''V_I(t'')\Psi_I(t'')\right) = \tag{5.24}$$

$$= \Psi_I(t)\left\{1 - i\int_t^{t+\Delta t} dt'V_I(t') + (-i)^2\int_t^{t+\Delta t} dt'V_I(t')\int_t^{t'} dt''V_I(t'')\right\} + \mathcal{O}(\Delta t^3) \tag{5.25}$$

Now expanding around $t = \bar{t} + \Delta t/2$ up to the second order

$$V_I(t') = V_I(\bar{t}) + (t-\bar{t})V_I'(\bar{t}) + \mathcal{O}(\Delta t^2) \tag{5.26}$$

and knowing that $\int_t^{t+\Delta t}(t'-\bar{t})dt' = 0$ one reaches the final form

$$\Psi_I(t+\Delta t) \simeq \left[1 - i\Delta t V_I(\bar{t}) + \frac{1}{2}\left(-i\Delta t\right)^2 V_I^2(\bar{t})\right]\Psi_I(t) \tag{5.27}$$

---

[2] S is obtained trough the Taylor expansion of both the exact and approximated form of the time evolution operator, or directly from the Baker-Campbell-Hausdorff formula

$$e^A e^B = e^C \qquad C = A + B + \tfrac{1}{2}[A,B] + \tfrac{1}{12}[A,[A,B]] + \tfrac{1}{12}[B,[B,A]] + ... \tag{5.20}$$

$$\Psi_I(t+\Delta t) \simeq e^{iV_I(\bar{t})\Delta t}\Psi_I(t) = \tag{5.28}$$

$$= e^{-iH_0\bar{t}}e^{-iV_I(\bar{t})\Delta t}e^{-iH_0\bar{t}}\Psi_I(t) \tag{5.29}$$

This last expression turned back in Schrödinger picture gives the final form in eq.5.19.
The convenience of this explicitly unitary approach becomes evident when applied to a particular configurations space. The kinetic operator is indeed diagonal in momentum space while a local potential is by definition diagonal in the coordinates space: by fast Fourier transforming form a space to the other will then be possible to use each exponential part of the split operator in their diagonal form, minimizing the computational effort.

5.2.5 Final Analysis

Once the wave packet has been propagated onto the potential energy surface for a time sufficient to consider as concluded the dynamical process, it is necessary to extract from it the cross sections. In scattering theory usually one computes the S matrix from initial and final wave function (taken in regions where the interaction potential is negligible) and its poles represent the resonances. Here we rather analyze the flux of the wave packet passing through a given line (plane) placed at a given position x_0 in the potential asymptotic region. This observable is associated to the flux operator

$$J_{x_0} = \langle\Psi|F|\Psi\rangle \tag{5.30}$$

that has the form

$$\langle\psi|F|\psi\rangle = \frac{1}{m}\mathrm{Im}\left(\langle\psi|x_0\rangle \left.\frac{d\langle x'|\psi\rangle}{dx'}\right|_{x'=x_0}\right) \tag{5.31}$$

State to state (ν, j) reaction probability comes from the flux in eq.5.31 when projecting the wave packet onto bound state wave functions for each partial wave component m

$$P^m_{\nu j} = \frac{\hbar}{\mu G(E)^2}\mathrm{Im}\left[\Phi^{m*}_{\nu j}(x_0, E)\left(\frac{d\Phi^m_{\nu j}(x', E)}{dx'}\right)_{x'=x_0}\right] \tag{5.32}$$

where $G(E)$ is the Gaussian intensity of the wave packet, for the energy component E; μ is the reduced mass, and $\Phi^m_{\nu j}(x_0, E)$ is the projection on a given product ν, j state

$$\Phi^m_{\nu j}(x_0, t) = \langle x_0 | \langle \phi_{\nu,j} | \psi_m(t) \rangle \tag{5.33}$$

Here $\Phi^{m*}_{\nu j}(r_0, E)$ comes from the so - called *time-energy mapping.*

$$\Phi^m_{\nu j}(x_0, E) = \int_0^\infty \Phi^m_{\nu j}(x_0, t) e^{iEt} dt \tag{5.34}$$

Probabilities can then be converted into cross sections.
The force of this approach is in the projection scheme. While projection on the molecular product ro-vibrational states gives state-to-state reactive cross sections, projecting on reagent bound states one can get the elastic and anelastic scattering information.

5.2.6 Absorbing Potentials

When the wave packet reaches the end of a numerical grid during the propagation, because of the periodic properties of the Fourier transform it re-enters in the grid from the opposite end. This is of course an unphysical effect that introduces artifacts in the dynamics: one way to avoid it to use of very long grids, *i.e.* very large basis set (DVR points). Another more practical solution is the use of imaginary potentials the absorb the wave packet at the grid ends.
From Heisenberg equation for a generic operator A

$$\dot{A} = \frac{\partial A}{\partial t} + i[H, A] \tag{5.35}$$

and defining the time derivative of an operator as

$$\langle \psi_t | \dot{A} | \psi_t \rangle = \frac{d}{dt} \langle \psi_t | A | \psi_t \rangle \tag{5.36}$$

is possible to see how, adding a purely imaginary potential to the system Hamiltonian one gets a non-hermitian operator for which eq.5.35 turns into

$$\dot{A} = \tfrac{\partial A}{\partial t} + i \left(H^\dagger A - AH \right) \qquad H = H^R + iV^{abs} \tag{5.37}$$

$$\dot{A} = \frac{\partial A}{\partial t} + i \left[H^R, A \right] - i \left[V^{abs}, A \right]_+ \tag{5.38}$$

In this way the norm of the wave function is no more conserved during the time evolution since U_t is no more unitary. According to eq.5.38 its decay proportional to the applied potential magnitude

$$\frac{d}{dt}\langle\psi_t|\psi_t\rangle = -2\langle\psi_t|V^{abs}|\psi_t\rangle \tag{5.39}$$

Is then possible to use an extra imaginary potential term in the Hamiltonian to damp out the wave packet at the grid's ends. Is also possible to choose the potential shape in order to minimize the reflection of some packet components. These potentials are designed to reduce wave packet transmission ans reflection and are known as *transmission free* [139]. They are efficient dealing with low energy components up to a certain minimum De Broglie wave length, that depends on their thickness on the DVR grid.

5.2.7 The Two Wave Packets Approach

In order to extract state-to-state cross sections from the final wave packet using a flux operator approach, the time-energy mapping (eq.5.34) is essential. Under two assumptions: (i) the initial wave packet is localized in the asymptotic region and (ii) it contains *incoming* components only, Such a form can also be written as s

$$\int_0^\infty \langle\mathbf{x}|\Psi_t\rangle\, e^{iEt}dt \simeq \tag{5.40}$$

$$\simeq 2\pi\sum_\alpha \langle\mathbf{x}|E\alpha+\rangle\,\langle E\alpha+|\Psi_0\rangle = 2\pi\sum_\alpha \langle\mathbf{x}|E\alpha\rangle\,\langle E\alpha|\Psi_0\rangle \tag{5.41}$$

where $|\Psi\rangle$ is the initial, $|E\alpha+\rangle$ a scattering eigenstate and $|E\alpha\rangle$ the final wave packet component of energy E in the scattering channel α. This is true only at the conditions (i) the initial wave packet is localized in the asymptotic region and (ii) it contains *incoming* components only, are both fulfilled. If so the time-energy mapping is as in5.41 the necessary matrix elements easily computable.

Instead, when outgoing (negative) momentum components are included in the initial wave packet, the equivalence in eq.5.41 does not hold and the flux operator approach cannot be used to extract reaction cross sections. For this reason when sampling the cold energy regime one shrinks the wave packet close to zero energy, not to include negative momenta, but its large spread in coordinates implies the use of very large DVR grids to handle it.

We instead adopted another recently proposed approach, never applied before for gas-surface dynamics[140]. This consists in re-writing the time-energy mapping using time reversal invariance of the initial state and the asymptotic expansion of $|E\alpha+\rangle$. Then *two* linearly independent wave packets are propagated one with even and one with odd symmetry respect to the energy origin. At the end of the dynamics the two are properly combined the negative momentum components and retrieve a correct result. The only condition necessary to this approach is (i) that the initial wave packet has still to lay in the asymptotic region, if not it would not be time-reversal invariance anymore.

5.3 Computational setup

Quantum scattering calculations have been performed within the scheme developed by Persson and Jackson[141], following the approach of Jackson and Lemoine[142] and the of Martinazzo [140] (as in sec.5.2.7) for the low energy regime. This consists in propagating one (two for low energies) wave packet on a DVR grid, following a potential energy surface (PES) at whose edge are applied transmission-free adsorbing potentials.

They considered the surface as flat and rigid and the lattice role has been taken into account by considering only two extreme situations [90]: in the first, 'adiabatic' case the carbon atom involved in the bond relaxes instantaneously at each hydrogen atoms position and ends up in the equilibrium (flat) position when the molecule leaves the surface. In the second, 'diabatic' case hydrogen formation is supposed to occur so fast that the same carbon atom remains fixed at its puckered position up to molecule formation, thereby transferring *de facto* part of the reaction exothermicity into phononic degrees of freedom.

In this approximation the dynamics is reduced to a three-dimensional one involving the coordinates of the two atoms above the surface and their mutual distance taken parallely to the surface, as shown in fig.5.1. Within the above approximations, two different sets of coordinates have been used: "product" and "reagent" coordinate sets, the choice depending on the state-to-state information one is interested in. Reagent set $\{z, Z, \rho\}$, can be used to compute ER cross sections only, while the product set for $\{z_i, z_t, \rho\}$ also allows to compute projectile trapping and, eventually, collision induced dissociation (CID). Most of the results in this chapter were obtained in this last coordinates set. In these calculations wavepacket

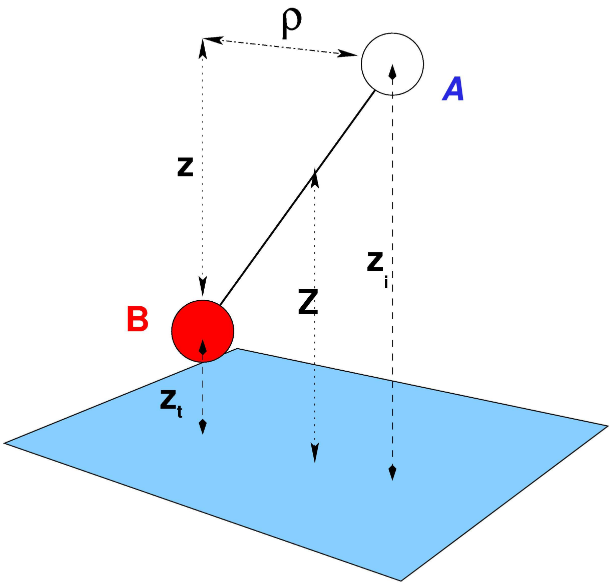

Figure 5.1: the coordinate sets used in Eley-Rideal reactive dynamics simulations. The projectile atom (A) is shown in white, while the target atom (B) in red. The "product" set include the projectile and target atom height above the surface, respectively z_i and z_t, while in the "reagent" set the mutual distance z and the center of mass height Z are considered. In both cases the AB distance taken parallel to the surface ρ is considered.

dynamics has been followed for rather long time ($25 - 30$ ps but in same cases up to 80 ps), and a reasonably large absorbing potential has been used in the entrance channel, with strength $E_{min} \sim 0.1$ meV to prevent spurious results at low energies.
The *first-principles* potential energy surfaces used here is the one of computed and Sha *et al.* [90] and fitted according to the London-Eyring-Polanyi-Sato (LEPS) functional form. In the case of a chemisorbed atom the adopted potential treats adiabatically the motion of the carbon atom involved in the reaction, while the incoming H atom only feels a physisorbed interaction (apart, of course, from the H-H interaction). Both these approximations are quite realistic at low energy, even when the possibility of dimer formation on the surface is taken into account. Indeed, low-energy H atom projectiles can hardly overcome the barrier to chemisorption, and are thus confined to the physisorption tail of the interaction potential. The only exception is the *para* dimer mentioned in Section **??**, whose formation is truly barrierless. If this possibility is taken into account the computed reaction cross-sections can (at worse) be considered a reasonable *upper* bound to the true ones.

5.4 Eley-Rideal Results

Results for the H_2 formation cross-sections from a chemisorbed target atom are reported in fig.5.2, for different values of the vibrational quantum number of the target atom lying on the surface $\nu = 0 - 2$, even though only the ground-state data are relevant for the chemistry of diffuse interstellar clouds being the excitation energy for $\nu = 1$ already too high for typical cloud temperatures.

It is evident from the fig.5.2 that, with the exception of highest initial vibrationally excited species considered, the computed cross-sections decrease steadily as the collision energy drops below $\sim$ 1000 K. We suppose this comes from a quantum effect. When a wave packet has a de Broglie wavelength is comparable with the potential well width it is partially reflected back by *quantum reflection*. On the PES we used for chemisorbed species this condition is fulfilled at an energy corresponding to few Kelvins. The relevant wavelength for H atoms impinging at 10 meV (~ 3 Å) is already larger than the order of the range of the H-H potential, hence the projectile can indeed be scattered back by this effect. This does not happen for vibrationally excited chemisorbed atoms or, as it will be shown, for

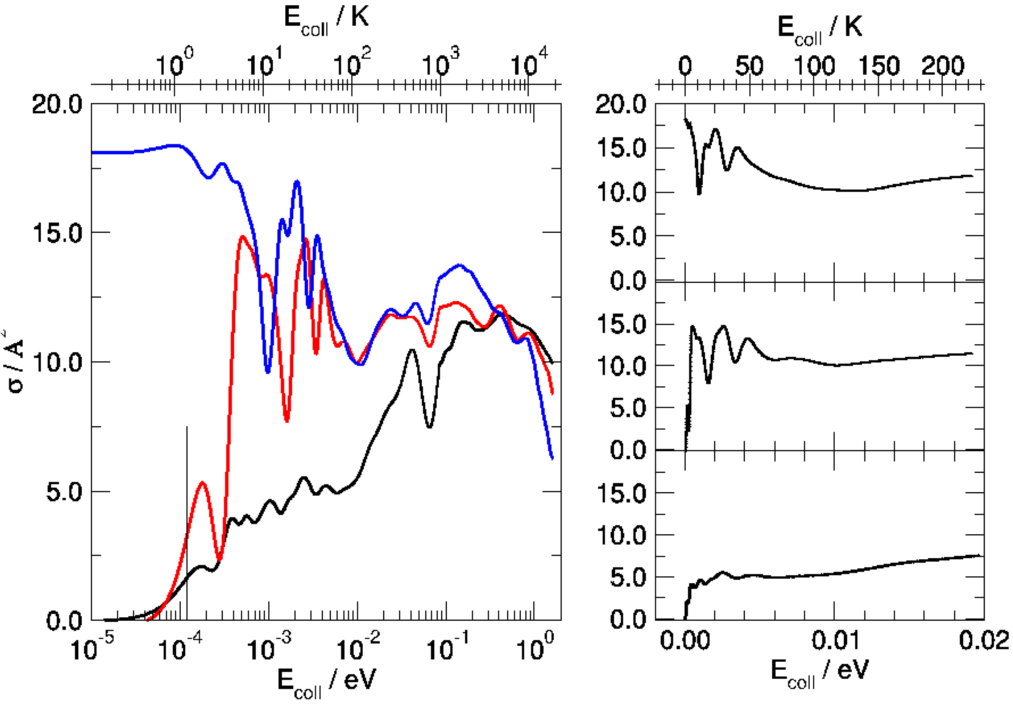

Figure 5.2: Total Eley-Rideal reaction cross-sections for chemisorbed species, as functions of the collision energy. Left panel: results on a logarithmic scale with black, red and blue curves for target atoms initially in the $\nu = 0, 1$ and 2 vibrational state, respectively. Vertical bar marks the strength of the absorbing potential in the entrance channel. Right panels: from bottom to top for $\nu = 0, 1, 2$.

weakly bound physisorbed ones whose potential well have a much larger width. Furthermore, collinear test calculations (here not reported) using an artificially cut H-H potential show that the onset of this behaviour shifts monotonically at higher energies as the cutoff distance is decreased. This phenomenon is indeed ascribed to the purely quantum reflection of a particle by a potential well.
A closer look at the reaction dynamics can be obtained by looking at the ro-vibrational distributions of the product H_2 molecules, as reported in fig.5.3 for 1 meV collision energy, results are unchanged for lower energies. The figure reveals that the reaction dynamics proceeds almost *collinearly* since the resulting rotational angular momentum j is quite small: $j \sim 0 - 1$. Moreover,as a consequence of the almost collinear mechanism the incident atom would bounce back to the gas phase rather that bound to the surface, so projectile trapping is very limited in this case.
The vibrational excitation is peaked at $\nu' = 8, 9$ and 10 for targets initially in the $\nu = 0, 1$ and 2 states respectively, in agreement with experiments that predict a vibrationally hot products. These values are close to the highest possible, and H_2 molecules leave the surface with only a small fraction of reaction exoergicity released as translational energy ($E_T \sim 0.4 - 0.3$ eV for $\nu = 0 - 2$), suggesting that the reaction proceeds in a vibrationally adiabatic way. In addition, the widths of the ro-vibrational distributions increase as the target atoms are vibrationally more excited, with larger fraction of product molecules appearing with vibrational quantum numbers lower than their most probable value. This suggests that some vibrationally relaxation occurs in the entrance channel, thereby allowing the projectile to get rid of quantum reflection when $\nu > 1$, at least in the energy regime considered here. At lower energies, any cross-sections is expected to decrease linearly with the speed v of the projectile, in agreement with Wigner's law which predicts a linearly vanishing *probability* for any exoergic process.

The results for Eley-Rideal cross-sections from physisorbed species, obtained with similar grid/propagation parameters as mentioned in the previous case, are shown in fig.5.4. They are only qualitatively similar to those shown in fig.5.2 and, in particular, they start to decrease only below E_{coll} =0.1 meV, where our results could be not well converged because for such low energies one should use both a propagation time and an AP length beyond our computational capabilities. However, in the astrophysically relevant energy range E_{coll} = 10-0.1 meV, reactive cross sections are quite large, considerably larger than those previously found at

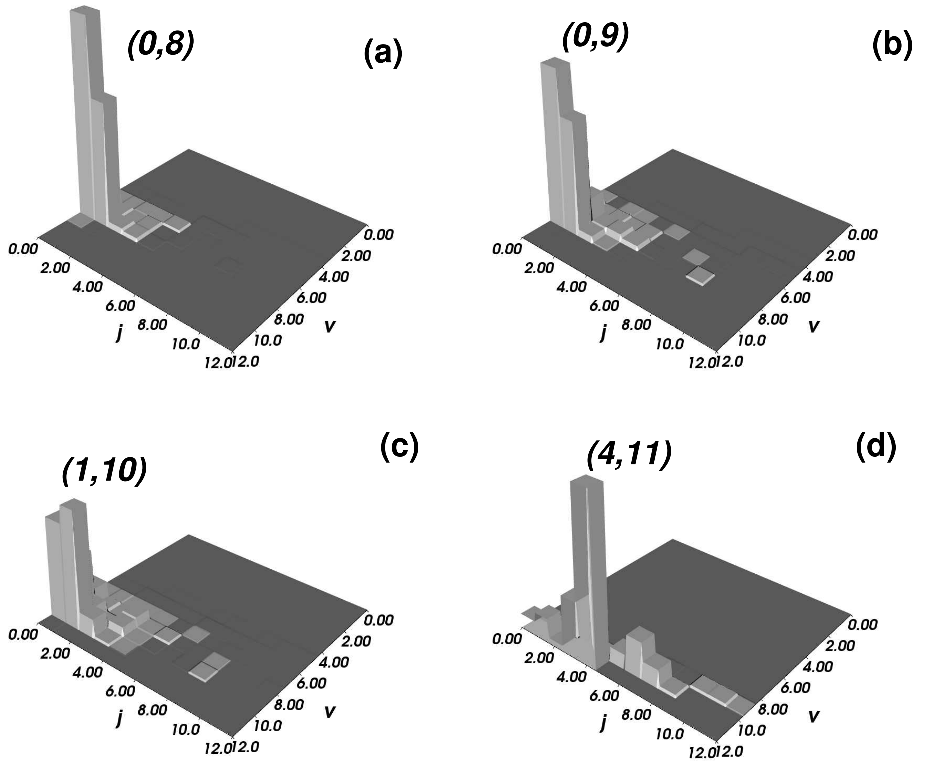

Figure 5.3: ro-vibrational distributions of product H_2 molecules formed at a collision energy of 10^{-3} eV, with the most probable (j, ν) values indicated. Panels (a)-(c) for chemisorbed target species with $\nu = 0 - 2$, respectively. Panel (d) for an initially physisorbed H atom in its ground vibrational state.

higher energies [90, 143], with peaks ~ 20 Å^2 high. The essential difference with the previous chemisorbed case is the larger *mobility* of the target atom allowed by the physisorption potential: when the projectile gets closer to the adsorbate, the latter has room to rearrange in such a way to increase the effective range of the H-H potential and to shift the onset of the quantum reflection to lower energies. This leads to some rotational excitation of the product molecules (see fig.5.3, panel (d)) which, consistently with the large values of the reaction cross-section, suggests that non-collinear collisions play an important role in this case. Furthermore, formation of trapped species is greatly enhanced when the gas-phase H atom scatters off a physisorbed species, and cross-sections as large as ~ 30 Å^2 are found for forming two atoms bound to the surface, moving parallelly to it (see fig.5.4, top panel on the right). These species might be important at non-zero coverage conditions, since they may recombine with further adsorbed H atoms far away from the site where they formed. For larger energies ($\sim$1000 K) collision induced desorption of the physisorbed target is very effective and becomes soon an overwhelming phenomenon in the overall dynamics. Its effect is visible in fig.5.5. Before concluding this section it is worth noticing that the cross-sections reported in fig.s5.2 and 5.4 have not been corrected for the electronic spin factor (1/4 for unpolarized H atom beams). This accounts for spin angular momentum conservation: when the reaction involves a chemisorbed species this is a subtle effect, as such a correction factor does *not* appear when different substrates (e.g. metals) are considered. Indeed, differently from metals, when the hydrogen atom is initially chemisorbed on the graphitic surface the unpaired spin is *not* quenched into the substrate, but it is still present in form of midgap state. Thus, the second (projectile) hydrogen atom has only 1/4 of chance of being in the overall singlet state needed for H_2 formation to occur. Note also that the corrected trapping cross-sections are expected to be similar to or larger than those shown in fig.5.4 (top right panel) as trapping can occur both in the singlet and in the triplet state (though in the latter case it would profit of the absence of any reactive competing channel). The cross-sections for all the processes taken into account corrected for spin angular momentum conservation are shown in fig.5.5 for the case in which the target atom is its vibrational ground state.

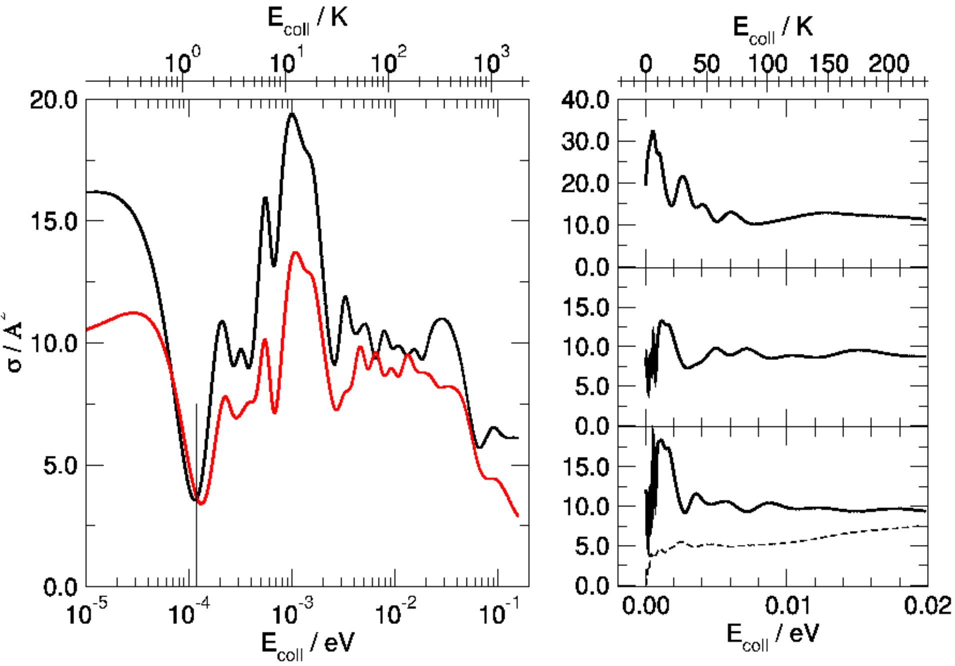

Figure 5.4: Total Eley-Rideal reaction cross-sections for physisorbed species, as functions of the collision energy. Left panel: black and red curves for target atoms initially in the $\nu = 0$ and 1 vibrational state. Vertical bar marks the strength of the absorbing potential in the entrance channel. Right panels: ER cross-sections for $\nu = 0 - 1$ in the two bottom panels, trapping cross-section for $\nu = 0$ in the top panel. Also reported the results for a chemisorbed atom ($v = 0$) as dashed line in the lower right panel.

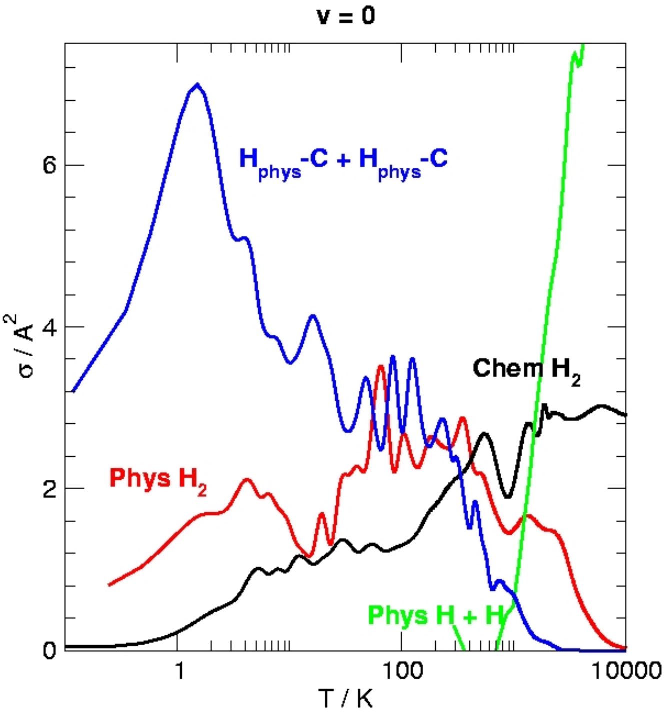

Figure 5.5: Total cross-sections for all the surface processes considered, for the target atom in the vibrational ground state. ER reaction from chemisorbed species (black line),ER reaction (red), trapping (blue) and collision induced desorption (green) from physisorbed species. All the data have been corrected by the proper spin factor.

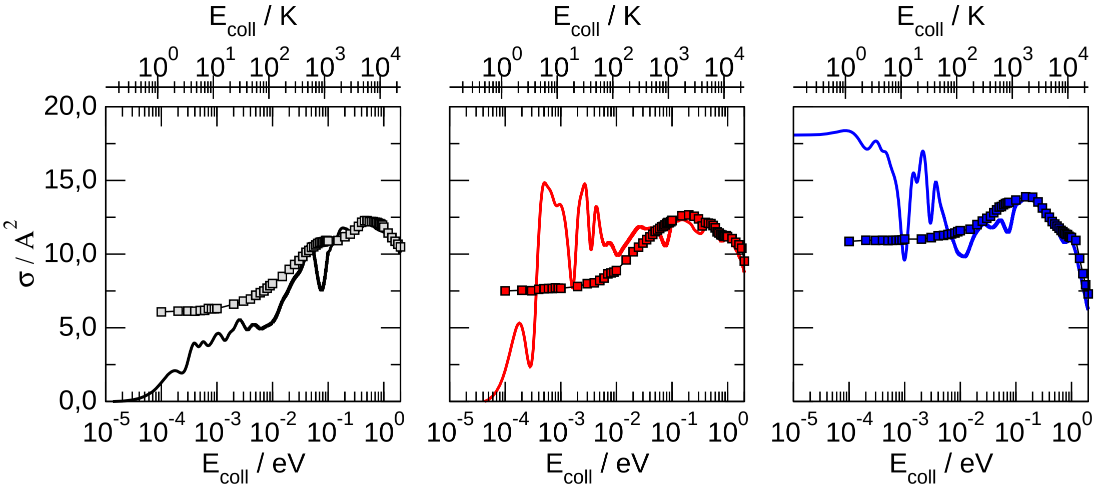

Figure 5.6: Comparison between classical (symbols) and quantum (lines) results for the Eley-Rideal reaction cross-sections of fig. 5.2. From left to right for $v = 0, 1, 2$ respectively.

5.5 Discussion

As many previous studies dealt with the Eley-Rideal hydrogen recombination on graphite[90, 144, 145, 146, 147, 148, 149, 150, 151, 152, 153, 154, 155], in this Section we analyze our results in deeper details by critically examining both the approximations introduced and the results of similar studies available in the literature. We only focus on the reaction involving chemisorbed H atoms, as this has been subjected to intense research activity in search of reaction pathways involving stable species and able to explain hydrogen formation at ISM conditions.

5.5.1 Classical vs. Quantum Dynamics

We start testing whether or not a quantal approach was really necessary for simulating this system in the energy range relevant for the ISM. We then performed a quasi-classical dynamical study on exactly the same potential energy surface used in the quantum calculations outlined in sec.5.4. In this framework, instead of using the time dependent Schrödinger's equationwe integrated the Newton's classical equations of motion for a number of trajectories, in order to sample different initial conditions for each energy. "Quasi"-classical means that quantization of the target vibrational motion is handled by properly sampling the initial conditions of the classical trajectories in such a way to reproduce the classical phase space density corresponding to the relevant quantum level [156]. Results are shown in fig.5.6, along with the results of fig.5.2 for comparison. As it is evident from the figure, classical mechanics does a pretty good job in reproducing the cross-section at high energies (apart from some undulations discussed in some recent paper[157, 156]) but fails in reproducing both the low energy resonances and the correct low energy behaviour. In particular, classical cross-sections start to diverge considerably from the quantum ones in the astrophysically relevant energy range $T < 100$ K and have a wrong limiting behaviour, tending towards non-zero values. This behaviour parallels known, marked differences between the classical and the quantum description of the sticking of atoms to surfaces. It is worth noticing at this point that the used potential energy surface is barrierless, that is the observed differences do not arise from simple tunneling phenomena, rather they are entirely due to quantum reflection. It follows that, even *without* a reaction barrier, classical studies of the title reaction have a limited value in the astrophysically relevant energy range, and then a quantal approach is necessary to retrieve realistic results.

5.5.2 Adiabatic vs. Diabatic Models

As in section 5.4 we considered, for H chemisorbed species, only one of the two possible limiting ways to implicitly include the important carbon atom in the dynamical model, namely the adiabatic picture of a relaxed substrate geometry in every point of the dynamics. we focus here on the case of a (substrate) diabatic dynamics, in which the carbon atom is kept puckered during the whole process. Only the case of a target atom initially in its ground vibrational state is considered, the results for v >0 behave very similarly. Results of these quantum calculations with the diabatic potential energy surface developed by Sha *et al.* [90] are shown in fig.5.7 where it is clear that, apart from a difference in magnitude $\lesssim$4 Å^2 over the whole energy range, the cross-section behaviour is similar in the two cases. This suggests that the same is true when including dynamically the carbon atom motion, and then that our general conclusion on the low energy behaviour of the Eley-Rideal cross-section should not be affected by a more exact treatment of the reaction dynamics. There are, of course, expected differences in the reaction energy partitioning as the way the carbon atom relaxes towards to the (bare) surface equilibrium position determines both the amount of energy left to the substrate and the energy going to internal excitation of the product molecules. We only note here that, even with the above two rigid-surface models, there are

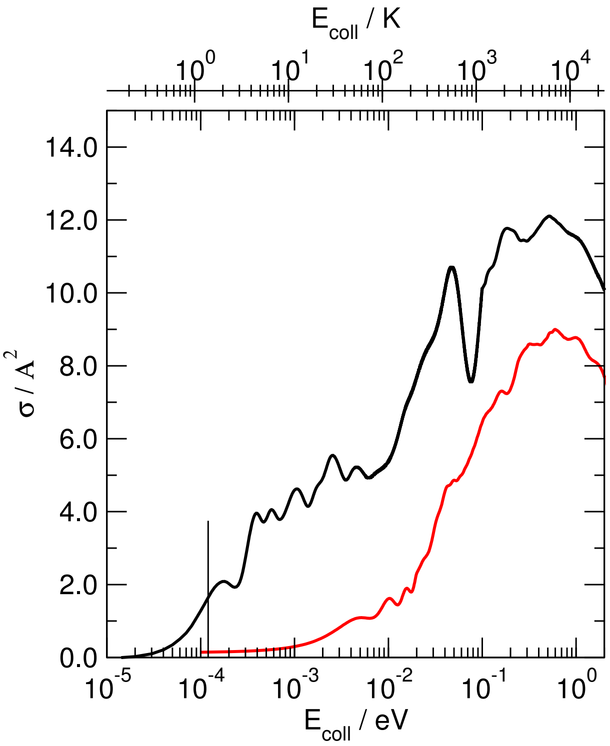

Figure 5.7: Eley-Rideal cross-sections in the diabatic (red) and adiabatic (black) models for $v = 0$.

quantitative differences in the vibrational excitation of the H_2 molecules. However, we do not attempt to compare these results with experimentally measured ro-vibrational distributions as the description of the H_2 potential energy curve of the adopted PES (analogously to many others in the literature) differs substantially from the exact one. Finally, it is not obvious that the studied adiabatic model is better than the diabatic one in describing the dynamics even at low energies, as the product molecule forms early in the collision process and leaves the surface with sizable translational energy that the carbon atom hardly has time to relax [149, 150].

5.5.3 The Role of the Substrate Model

A direct comparison between present and previous results from different groups is hard to perform as different researcher adopted different potential and/or dynamical models. Furthermore, the used potential energy surfaces (PESs) are not always publicly available and this prevents one to perform dynamical calculations under similar conditions. There are however global differences which might persist at any level of description: one of them is the behaviour of the reaction probability in the collinear (2D) approximation. Indeed, some potential energy surfaces used by others, give rise to a very high reaction probability and to a resonant behaviour in the whole energy range $0 - 0.5$ eV, while others (including the present ones) give rise to a smooth (almost free of resonances) decreasing probability as the energy decreases in the same range.

We therefore focus here on the results reported in refs.[148, 149] and ref.[150]); since the PES used in these works are not publicly available we re-computed the relevant 2D cuts with similar electronic structure means, namely DFT with an atom-centered basis set, using coronene as a substrate model. Electronic structure calculations have been performed with the help of GAUSSIAN code[158] both for the adiabatic and diabatic models and fitted to the same functional form used by Sha *et al.* [90]. Furthermore, plane-wave based DFT calculations of the same reaction have been performed using graphene as a model substrate and for different sizes of the unit cell.

The potential energy surfaces computed on the cluster model surface looks qualitatively similar to the periodic DFT one used in our study in sec.**??** (see fig.5.8 left panel). Both of them show a simple downhill route from reagent to product, but the *shape* of the PES in the corner region is different for the two substrate

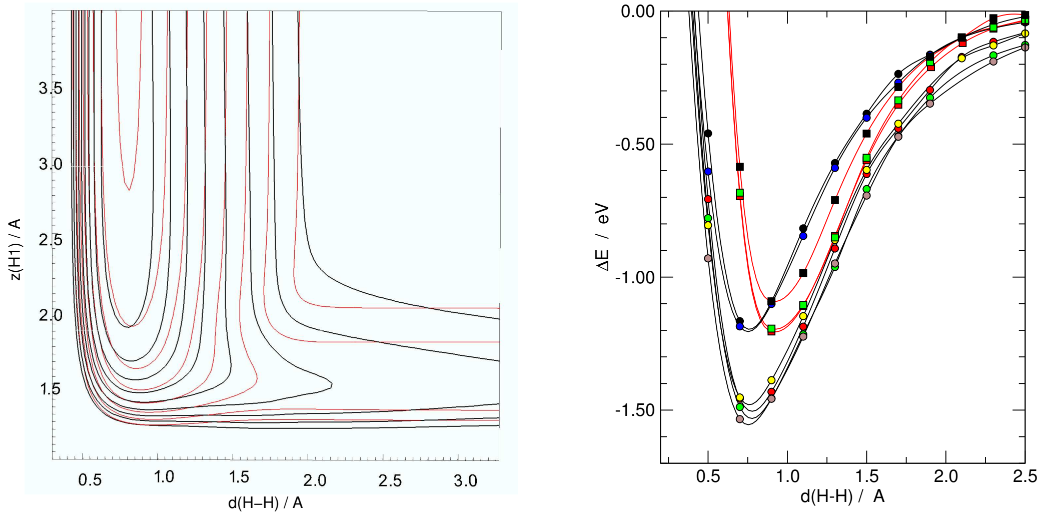

Figure 5.8: Results of *first principles* electronic structure calculations on the reaction energetics performed using different models for the surface. Left panel: contour lines (black) for the diabatic collinear PES computed at the DFT/ PW91-VWN/ cc-pVDZ level using coronene as substrate model. Also shown as red lines the diabatic PES of Sha *et al.*[90], corresponding to a periodic graphitic model. Right panel: energy as a function of the projectile H atom height for fixed heights of both the target hydrogen and the underneath carbon atoms, in collinear geometry. Circles for the coronene model (black for B3LYP/cc-pVDZ, red for PB86/cc-pVDZ, green for PW91VWN/cc-pVDZ, blue for B3LYP/cc-pVTZ, yellow for PB86/cc-pVTZ, brown for PW91VWN/cc-pVTZ), squares for a periodic graphene model (plane-wave based DFT/PBE for a 2x2 cell in black, 3x3 in red, 4x4 in green).

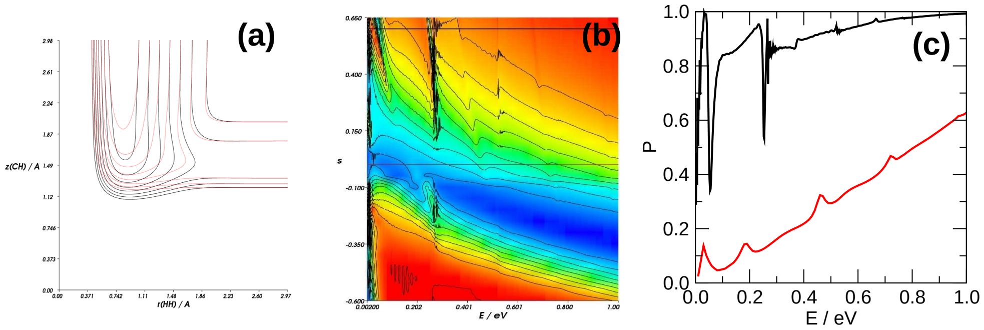

Figure 5.9: Results of model calculations in which the target-atom Sato parameter s defined in the diabatic PES of Sha *et al.*[90] has been changed in the interval $[-0.6, 0.7]$. (a) Contour lines of the PESs with $s = 0.6$ (black) and $s = 0.035$ (red). (The latter value corresponds to that optimized in Ref. [90]). (b) Reaction probability as function of both the energy and s (x and y axes, respectively). Horizontal lines mark the values $s = 0.60$, 0.035. (c) Reaction probability for $s = 0.60$, 0.035 (black and red line, respectively).

models considered and also for different level of theory. This is shown in fig.5.8, right panel, where the different curves reported refer to the same cut in the entrance channel, namely with the target H atom fixed at its equilibrium position. Strangely we note how the curve computed with B3LYP functional on coronene looks quite similar to periodic DFT results.

This seemingly small dependence of the PES features on the choice of the substrate model leads to significant differences in the computed reaction probabilities, as a consequence of purely classical effects. This is best seen in model calculations using the same modified London-Eyring-Polanyi-Sato (LEPS) functional form defined by Sha *et al.* [90] and varying one of the Sato parameter, while keeping all other parameters at their optimal values defined in ref.[90]. When changing the Sato parameter for the target H atom in the range 0.0-0.8 we smoothly modify the PES along the entrance channel, as observed when going from graphene to coronene, without introducing any undesired artifacts (see fig.5.9, left panel. The same is not true for negative values of this parameter as they lead to the appearance of a well in the exit channel). Correspondingly, the reaction probabilities drastically change, and show an almost uniform unit value at the higher end of the interval (Fig.5.9, center and right panels).

It is reasonable to expect that similar dependence on the substrate model has to be found in more realistic dynamical models at least for near-collinear collisions.

The question then arises whether the coronene model (or similar model based on small PAHs) is realistic enough to describe Eley-Rideal hydrogen formation on graphite.

5.5.4 The Role of an Eventual Energy Barrier to Reaction

In previous studies [148] it has been found that density functional theory calculations of the potential energy surface shows a tiny barrier ($\sim$ 10 meV) in the reaction profile. As this value is too small for being accurately predicted by DFT techniques, we decided to neglect it by using the analytical PESs defined in ref.[90]. Its possible presence is currently hard to assess, for more accurate quantum chemistry techniques apply to cluster models only but, according to the discussion above, these might not be realistic enough to describe hydrogen recombination on graphite. This is quite unpleasant as its influence on the low-energy dynamics would be enormous, as already emphasized by Morisset *et al.* [148, 149]. If this were the case, our computed cross-sections for the reaction involving chemisorbed species would be further reduced for energies below barrier by the corresponding tunneling probability and our main conclusion that Eley-Rideal reaction is more efficient if it involves physisorbed atoms would be enforced. The main point here is that this is true even when such a barrier is absent. Incidentally, we note here that analogous problems appear for other regions of the configuration space (e.g. the asymptotic region of the entrance channel) which too have a strong influence on the low energy dynamics. The result is that such exothermic surface reactions (the only one which are possible in the extreme conditions of the ISM) present a challenge as they require an accuracy on the potential energy surface ($\sim$ 10 meV) which is currently impossible to obtain.

5.6 Summary

We performed a quantum study of the hydrogen recombination using single-layer graphene as a model for graphite basal plane, *i.e.* {0001} surface. Results show that chemisorbed and physisorbed H atoms behave differently respect to the Eley-Rideal reaction at typical interstellar cloud conditions (fig.5.4). The first undergo a collinear-dominated reaction mechanism which becomes increasingly inefficient when the energy decreases below $\sim 10^{-2}$ eV, probably because of the quantum reflection of the incident wave packet from the strong, short-range potential characterizing the exit (reaction) channel. Under these conditions trapping of the incident atom is negligible, with cross-sections vanishing in the same energy range. These dynamical results likely hold independently on the fact that the chemisorbed atom is an isolated one or is part of a cluster, thereby suggesting the chemisorbed species play a minor role in hydrogen formation at interstellar cloud conditions, even when a barrierless chemisorption process occurs.

In contrast, physisorbed species are weakly bound to the surface and may promptly release hydrogen molecules or form trapped species even at low energies, with cross-sections which are $2-3$ times larger than the previous ones in the relevant energy range. As already mentioned in the Introduction, taking also into account the tight kinetic constraints in chemisorbing H atoms, we are tempted to conclude, based on present results, that hydrogen formation in diffuse clouds either involves physisorbed species only (and sufficiently low surface temperature to limit desorption) or cannot be explained by a simple graphitic model. There remain, however, several open questions concerning both the accuracy of the potential and the dynamics, and they still represent challenging problems.

Chapter 6

Summary and Conclusions

In this thesis we addressed the chemisorption, clustering and reaction dynamics of hydrogen atom on graphene. First, we showed how an hydrogen atom can bind to a graphene surface and the the effects it induces on the substrate that, in contrast with metals or other semiconductors, shows midgap states and magnetic structures. Then, we addressed hydrogen atoms clustering on graphene. This is a complex phenomenon driven by a subtle balance between electronic effects, and relaxation energies. A simple Valence Bond model gave us the possibility not only to understand the clustering, but also to predict stability and magnetism of a general arrangements of adsorbates, that can be of great importance for the design of graphene-based materials for electronics.

At last, we studied the Eley-Rideal recombination dynamics of H atoms to give molecular hydrogen, showing the importance of quantum effects in low energy reactivity of the H-graphene system. This process is very important for astrochemistry, and our results prove that H_2 production form physisorbed hydrogen on graphite can be an efficient process even at temperatures lower than 10 Kelvins.

Appendix A

Graphene Electronic Structure

A.1 Tight-Binding Model for Graphene

Here will be shown in details how the tight-binding Hamiltonian for graphene in the nearest-neighbours approximation leads to the linear bands dispersion and to the Dirac equation close to the Fermi energy.

In building up a π model we write the wave function as a linear combination of two basis functions made of the p_z orbitals of the two sublattices [159]

$$\psi(\mathbf{r}) = c_A \psi^A(\mathbf{r}) + c_B \psi^B(\mathbf{r}) \tag{A.1}$$

$$\psi^A(\mathbf{r}) = \sum_{\mathbf{k}\in BZ} \frac{1}{\sqrt{N}} e^{i\mathbf{k}\cdot\mathbf{r}} p_z(\mathbf{r}-\mathbf{r}_A) \qquad \psi^B(\mathbf{r}) = \sum_{\mathbf{k}\in BZ} \frac{1}{\sqrt{N}} e^{i\mathbf{k}\cdot\mathbf{r}} p_z(\mathbf{r}-\mathbf{r}_B) \tag{A.2}$$

The Hamiltonian expressed in second quantization is the following:

$$\hat{H} = \sum_{<i,j>} \sum_{\sigma=\uparrow,\downarrow} -t \left(\hat{a}^\dagger_{i,\sigma} \hat{b}_{j,\sigma} + h.c. \right) \tag{A.3}$$

where $\hat{a}^\dagger_{i,\sigma}$ creates an electron with spin σ on the ith lattice site, part of the A sublattice and its conjugate will annihilate it. In the same fashion $\hat{b}^\dagger_{j,\sigma}$ ($\hat{b}_{j,\sigma}$) will create (annihilate) an electron on the jth site of the B sublattice. This interaction mimics the hopping between sites and it is limited in the sum only over each site nearest neighbours and for graphene costs an energy of $t \simeq 2.7$ eV. Longer range hoppings can be considered, although here already the second nearest neighbours hopping t' is an order of magnitude smaller than t, so does not change much the overall band structure.

The most natural choice is then to switch to a Bloch's functions basis by Fourier transforming the operators in Hamiltonian A.3. Note that Bloch's functions are not in general eigenfunctions of the number operator, but in the momentum space this basis vectors are the occupation numbers for linear combinations of plane waves (Bloch's function) centered on a single sublattice $|A\rangle$ or $|B\rangle$. In the coordinates space, the new of basis is [1]

$$\hat{a}_{\mathbf{r_A}} = \frac{1}{\sqrt{N}} \sum_{\mathbf{k} \in BZ} e^{-i\mathbf{k}\cdot\mathbf{r_A}}\, \hat{a}_{\mathbf{k}} \quad \Longrightarrow \quad \hat{a}_{\mathbf{k}} = \frac{1}{\sqrt{N}} \sum_{\mathbf{r}_A \in BK} e^{i\mathbf{k}\cdot\mathbf{r_A}}\, \hat{a}_{\mathbf{r_A}} \tag{A.4}$$

$$\hat{b}_{\mathbf{r_B}} = \frac{1}{\sqrt{N}} \sum_{\mathbf{k}' \in BZ} e^{i\mathbf{k}'\cdot\mathbf{r_B}}\, \hat{b}_{\mathbf{k}'} \quad \Longrightarrow \quad \hat{b}_{\mathbf{k}'} = \frac{1}{\sqrt{N}} \sum_{\mathbf{r}_B \in BK} e^{-i\mathbf{k}'\cdot\mathbf{r_B}}\, \hat{b}_{\mathbf{r_B}} \tag{A.5}$$

where BZ refers to the first Brillouin zone and BK to the Born- von Karman cell, that defines the boundary conditions in real space. Restricting the sum to the sublattice A sites only and using the nearest neighbour vectors to identify B sites as $\mathbf{r}_B = \mathbf{r}_A + \delta_j$ the Hamiltonian reads:

$$\hat{H} = -t \sum_{\mathbf{r_A}} \sum_{j=1}^{3} \sum_{\mathbf{k},\mathbf{k}'} \frac{1}{N} \left(\hat{a}^{\dagger}_{\mathbf{k}} e^{-i\mathbf{k}\cdot\mathbf{r_n}} \hat{b}_{\mathbf{k}'} e^{i\mathbf{k}'\cdot(\mathbf{r_n}+\delta_j)} \right) + h.c. \tag{A.6}$$

$$\hat{H} = -t \sum_{\mathbf{r_A}} \sum_{j=1}^{3} \sum_{\mathbf{k},\mathbf{k}'} \frac{1}{N} \left(\hat{a}^{\dagger}_{\mathbf{k}} \hat{b}_{\mathbf{k}'} e^{-i(\mathbf{k}-\mathbf{k}')\cdot\mathbf{r_n}} e^{i\mathbf{k}'\cdot\delta_j} \right) + h.c. \tag{A.7}$$

$$\hat{H} = -t \sum_{j=1}^{3} \sum_{\mathbf{k},\mathbf{k}'} \left(\hat{a}^{\dagger}_{\mathbf{k}} \hat{b}_{\mathbf{k}'} \delta_{\mathbf{k},\mathbf{k}'} e^{i\mathbf{k}'\cdot\delta_j} \right) + h.c. \tag{A.8}$$

$$\hat{H} = -t \sum_{\mathbf{k} \in BZ} \left(f(\mathbf{k}) \hat{a}^{\dagger}_{\mathbf{k}} \hat{b}_{\mathbf{k}} \right) + h.c. \tag{A.9}$$

where we have introduced the complex factor

$$f(\mathbf{k}) = \left\{ e^{i\mathbf{k}\cdot\delta_1} + e^{i\mathbf{k}\cdot\delta_2} + e^{i\mathbf{k}\cdot\delta_3} \right\} \tag{A.10}$$

The Hamiltonian matrix has only off-diagonal elements since the action of an operator on a basis function owing to to different sublattice will give zero.

$$\hat{b}_{\mathbf{k}} |A(\mathbf{k})\rangle = 0 \qquad \hat{a}_{\mathbf{k}} |B(\mathbf{k})\rangle = 0 \qquad \hat{a}_{\mathbf{k}} |\ldots 1^{A}_{\mathbf{k}'} \ldots\rangle = \delta_{\mathbf{k},\mathbf{k}'} |0\rangle \tag{A.11}$$

$$\begin{pmatrix} 0 & H_{AB} \\ H_{BA} & 0 \end{pmatrix} \begin{pmatrix} c_A \\ c_B \end{pmatrix} = E(\mathbf{k}) \begin{pmatrix} c_A \\ c_B \end{pmatrix} \tag{A.12}$$

---

[1] From now on we will drop the spin index σ for the sake of simplicity.

Then, the matrix elements are $H_{AB} = -t\ f(\mathbf{k})$ and so the eigenvalues for the secular determinant:

$$E(\mathbf{k})_{\pm} = \pm\sqrt{|H_{AB}|^2} = \pm t\,|f(\mathbf{k})| \tag{A.13}$$

$$= \pm t\sqrt{3 + 2\cos(\mathbf{k}\cdot(\delta_1 - \delta_2)) + 2\cos(\mathbf{k}\cdot(\delta_2 - \delta_3)) + 2\cos(\mathbf{k}\cdot(\delta_1 - \delta_3))} \tag{A.14}$$

To obtain the explicit expression for the eigenvalues one have to use the lattice vectors coordinates $\{\mathbf{a}_{1,2}\}$ and the nearest neighbour positions $\{\delta_{1,2,3}\}$ defined as in fig.1.1 [11]

$$\mathbf{a}_1 = d\left(\frac{3}{2};\frac{\sqrt{3}}{2}\right) \qquad \mathbf{a}_2 = d\left(\frac{3}{2};-\frac{\sqrt{3}}{2}\right) \tag{A.15}$$

where d is the carbon-carbon distance, equal to about 1.42 Å.

$$\delta_1 = d\left(-\frac{1}{2};\frac{\sqrt{3}}{2}\right) \qquad \delta_2 = d\left(-\frac{1}{2};-\frac{\sqrt{3}}{2}\right) \qquad \delta_3 = d\,(-1;0) \tag{A.16}$$

so, the final results is

$$E(\mathbf{k})_{\pm} = \pm t\sqrt{3 + 2\cos\left(\sqrt{3}k_y d\right) + 4\cos\left(\frac{3}{2}k_x d\right)\cos\left(\frac{\sqrt{3}}{2}k_y d\right)} \tag{A.17}$$

where the minus sign solution correspond to the π and the plus to the π^* band[159, 11]. The energy dispersion in eq.A.17 along the high symmetry direction in the two dimensional graphene lattice is shown in fig.1.2 and fig.A.1.

From the bands plot it is visible the linear dispersion that forms a conical intersection between conduction and valence bands in $\mathbf{K}$ and $\mathbf{K}'$: this feature occurs here due to symmetry reasons. Indeed, graphene at the Γ point belongs to the D_{6h} point group, that contains two-dimensional representations: in the basis of Bloch functions of the two sublattices these can be decomposed in two one-dimensional representations. Instead, in $\mathbf{K}$ and $\mathbf{K}'$ the symmetry is lowered down to the D_{3h} group which contains the irreducible representations A_2'' and E'. The latter is also two-dimensional but in this basis cannot be decomposed any further, hence it supports a two fold degeneracy that here occurs exactly at the Fermi energy. Under another perspective one might focus on the matrix element $f(\mathbf{k})$ in eq.A.12 and look for its zeroes.

$$f(\mathbf{k}) = \left\{e^{i\mathbf{k}\cdot\boldsymbol{\delta_1}} + e^{i\mathbf{k}\cdot\boldsymbol{\delta_2}} + e^{i\mathbf{k}\cdot\boldsymbol{\delta_3}}\right\} = 0 \tag{A.18}$$

The sum three complex number in $f(\mathbf{k})$ has to sum to zero: among the infinite ways to achieve this result there is only one in which the three have the same

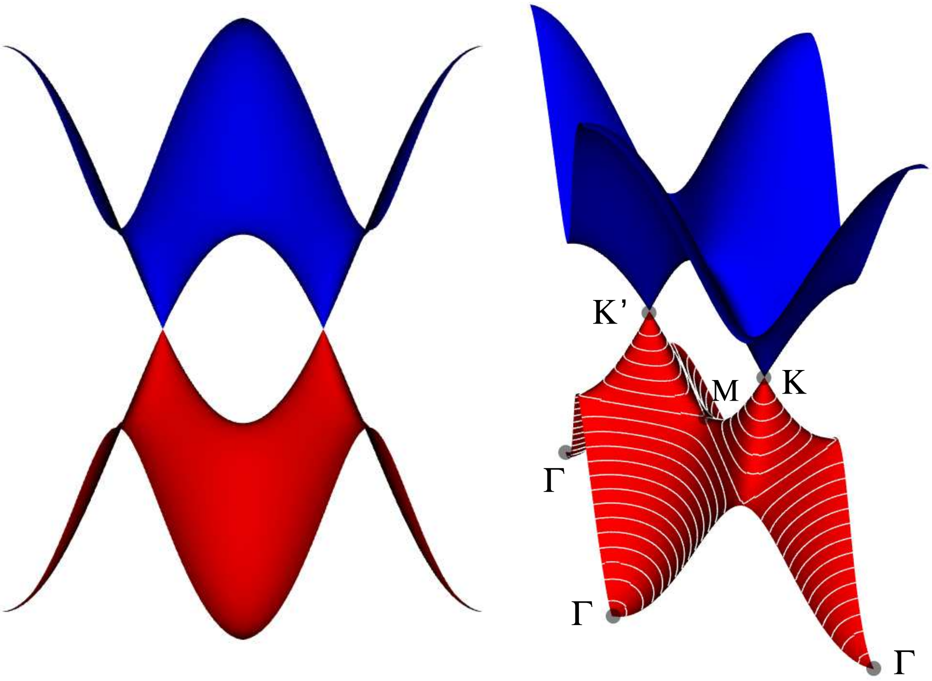

Figure A.1: Graphene band structure plot in the reciprocal unit cell obtained with the tight binding method. Left: front view of the Dirac cones at **K**,**K′** , Right: a side view with special points labels from which is possible to notice the linearity of bands part of the two cones.

absolute value (that here is one) that is when they are the well known three roots of unity in the complex plane: $e^{i\pi/3}$, $e^{i\pi 2/3}$, $e^{2i\pi}$. This occurs in graphene only $\mathbf{K}$ and $\mathbf{K}'$ and it can be easily seen by using the δ vectors coordinates into eq.A.10. Substituting in eq.A.12 the eigenvalues $E = st|f(\mathbf{k})|$, (where $s = \pm$) one retrieves the two eigenvectors

$$\begin{pmatrix} E & tf(\mathbf{k}) \\ tf^*(\mathbf{k}) & E \end{pmatrix} \begin{pmatrix} c_A^k \\ c_B^k \end{pmatrix} = 0 \tag{A.19}$$

following the first equation

$$Ec_A^k + tf(\mathbf{k})c_B^k = 0 \tag{A.20}$$

$$\frac{c_B^k}{c_A^k} = \frac{-st|f(\mathbf{k})|}{t\ f(\mathbf{k})} = \frac{-st|f(\mathbf{k})|}{t\ |f(\mathbf{k})|e^{i\phi}} = -\frac{1}{se^{i\phi}} \tag{A.21}$$

$$\begin{pmatrix} c_A^k \\ c_B^k \end{pmatrix} = \begin{pmatrix} 1 \\ -se^{i\phi} \end{pmatrix} \tag{A.22}$$

Where the argument of the complex factor $f(\mathbf{k})$ has been separated by its phase. The normalized eigenvectors in the Bloch form are then:

$$\psi_{\pm\mathbf{k}}(\mathbf{k}) = \frac{1}{\sqrt{2}} \begin{pmatrix} 1 \\ -se^{i\phi} \end{pmatrix} e^{i\mathbf{k}\cdot\mathbf{r}_i} \tag{A.23}$$

A.2 The Dirac Hamiltonian at K

Close to zero, *i.e.* to the Dirac points, it is possible to expand the band structure according to **k**=**K**+**q**, so that $f(\mathbf{k})$ turns into

$$f(\mathbf{K}+\mathbf{q}) = e^{i\mathbf{K}\cdot\delta_1}e^{i\mathbf{q}\cdot\delta_1} + e^{i\mathbf{K}\cdot\delta_2}e^{i\mathbf{q}\cdot\delta_2} + e^{i\mathbf{K}\cdot\delta_3}e^{i\mathbf{q}\cdot\delta_3} \tag{A.24}$$

and using the coordinates of $\mathbf{K}$ in eq.1.4

$$= e^{i\frac{2}{3}\pi}e^{i\mathbf{q}\cdot\delta_{\mathbf{1}}} + e^{i\mathbf{q}\cdot\delta_{\mathbf{2}}} + e^{-i\frac{2}{3}\pi}e^{i\mathbf{q}\cdot\delta_{\mathbf{3}}} = \tag{A.25}$$

$$f(\mathbf{K}+\mathbf{q}) = e^{i\mathbf{q}\cdot\delta_{\mathbf{2}}} + \cos\left(\frac{2\pi}{3}\right)\left(e^{i\mathbf{q}\cdot\delta_{\mathbf{1}}} + e^{i\mathbf{q}\cdot\delta_{\mathbf{3}}}\right) + i\sin\left(\frac{2\pi}{3}\right)\left(e^{i\mathbf{q}\cdot\delta_{\mathbf{1}}} - e^{i\mathbf{q}\cdot\delta_{\mathbf{3}}}\right) \tag{A.26}$$

using the series expansion of the exponential up to first order

$$= 1 + i\mathbf{q}\cdot\delta_2 - \frac{1}{2}\left(2 + \mathbf{q}\cdot(\delta_1 + \delta_3)\right) + i\sin\frac{\sqrt{3}}{2}\left(1 + \mathbf{q}\cdot(\delta_{\mathbf{1}} - \delta_{\mathbf{3}})\right) \tag{A.27}$$

Noticing that $\delta_1 + \delta_3 = -\delta_2$ one can introduce a new set of coordinates

$$\hat{\mathbf{q}}_x = \tfrac{1}{d}\delta_2 \qquad \hat{\mathbf{q}}_y = \tfrac{1}{\sqrt{3}d}(\delta_1 - \delta_3) \tag{A.28}$$

the matrix elements can be re-written as

$$f(\mathbf{K} + \mathbf{q}) = i\frac{3d}{2}\mathbf{q} \cdot \hat{\mathbf{q}}_x + i\frac{3d}{2}\mathbf{q} \cdot \hat{\mathbf{q}}_y = \frac{3d}{2}\left(q_x + iq_y\right) \tag{A.29}$$

In this way the matrix form of the Hamiltonian is equivalent to the one of two-dimensional Dirac's equation in momentum space where the speed of light c is replaced by the Fermi velocity that for graphene is $\sim c/300$ [11]

$$\hat{H}_{\mathbf{K}} = \nu_F\ \sigma \cdot \mathbf{q} = \nu_F \begin{pmatrix} 0 & q_x + iq_y \\ q_x - iq_y & 0 \end{pmatrix} \tag{A.30}$$

And where σ is a vector made of the Pauli matrices

$$\sigma = \begin{pmatrix} \sigma_x & \sigma_y \end{pmatrix} \tag{A.31}$$

Following eq.A.13 the eigenvalues are

$$E(\mathbf{q}) = \pm \nu_F q \tag{A.32}$$

where we introduced the Fermi velocity $\nu_F = 3td/2$.
The corresponding eigenvectors in **k**=**K** are

$$\psi_{\pm,\mathbf{K}}(\mathbf{q}) = \frac{1}{\sqrt{2}} \begin{pmatrix} 1 \\ s\ e^{i\theta} \end{pmatrix} e^{i\mathbf{q}\cdot\mathbf{r}} \tag{A.33}$$

where now the phase θ is referred to the q_x, q_y vectors

$$\theta = \arctan(q_x/q_y) \tag{A.34}$$

Carrying on the same procedure for $\mathbf{K}'$ one gets similar results but with the opposite eigenvector phase θ. The eigenvector in eq.A.33 has the form of a two-components spinor in which the two components are the probability amplitude of the wave function on each sublattice.

Spinors when integrated along a closed path surrounding a singular point acquire a phase known as the Berry phase. When moving adiabatically one eigenvector along a closed path the state vector gains a phase at each infinitesimal move. After a complete turn the phase factor should be equal to one ($e^{2\pi i}$), so that the eigenvector gains back its initial value. When the integration path encloses a

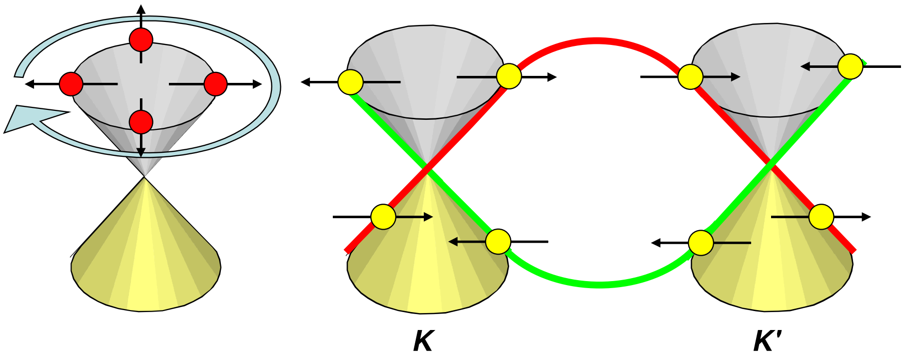

Figure A.2: Left: in graphene the adiabatic transport of the wave function along a closed path that surrounds the cones axis induces a Berry phase of π. Right: Relation between the pseudospin (black arrows) in the two cones at $\mathbf{K}$ and $\mathbf{K}'$. Same band branches bear the same pseudospin direction.

singularity, such as the Dirac point in graphene, the acquired phase is not zero for a closed loop. In the case of the circular path as in fig.A.2 that encloses the Dirac point one finds a Berry's phase of π, hence the eigenvector changes sing after being adiabatically moved along a closed loop. A phase change of π is indeed a typical feature of spinor functions.

Another important consequence of having spinorial eigenvectors is the existence of a pseudospin.

$$\langle\psi_K|\hat{\sigma}|\psi_K\rangle = \langle\psi_K|\sigma_x|\psi_K\rangle\,\hat{\mathbf{q}}_x + \langle\psi_K|\sigma_y|\psi_K\rangle\,\hat{\mathbf{q}}_y = \tag{A.35}$$

When using the eigenvectors in eq.A.33

$$= \frac{1}{2}\left(se^{i\theta} + se^{-i\theta}\right)\cdot\hat{\mathbf{q}}_x + \frac{1}{2}\left(ise^{i\theta} + ise^{-i\theta}\right)\cdot\hat{\mathbf{q}}_y = \tag{A.36}$$

$$\hat{\mathbf{q}}_x s\cos\theta + \hat{\mathbf{q}}_y s\sin\theta = s\hat{\mathbf{q}} \tag{A.37}$$

This spin projection is known as pseudospin and it is defined for each eigenvalue at every $\mathbf{q}$ ($\mathbf{q}$). In graphene this vector is purely two-dimensional and lays normally to the cones axis because of the equivalence between the two sublattices. In the polar representation of spin allowed by $SU(2)$-$SO(3)$ correspondence it is possible to map the pseudospin on a spherical surface. Pseudospin has the same properties but, since the two basis functions (sublattices) here are equivalent, the sphere equatorial plane alone is enough to identify a given pseudospin state. The cone cuts at the energy E and $-E$ are shown in fig. 1.5: the pseudospin vector for electrons at energy E (π^* band) is oriented along with the momentum vector, so inwards, while for holes (π band) is directed in the opposite way, outwards the cones axis. Note that an electron with energy E propagating following the momentum $\mathbf{q}$ has the same pseudospin as a hole with energy $-E$ propagating in the opposite direction $-\mathbf{q}$. This yields that electrons and holes belonging to the same branch of the band structure have pseudospins pointing in the same direction, which is parallel to the momentum $\mathbf{q}$ for electrons and anti-parallel for holes (fig.1.5 left panel). The pseudospin projection operator onto the momentum direction is usually known as helicity operator and its two possible eigenvalues $s = \pm 1$ as chirality: in this fashion different cones bear carriers with different chirality. It is also worth noticing that $\mathbf{K}$ and $\mathbf{K}'$ are related each other by time reversal symmetry (fig.A.2): so from the bands branch crossing the pseudospin is reversed in the two cones respect to $\mathbf{K}$. Nevertheless the overall chirality does not change since under time reversal both the momentum and pseudospin direction are inverted.

Appendix B

Computational Details and DFT Settings

Density functional theory calculations included in this thesis were done using the VASP code [160, 161]. This program use a plane wave basis for the Kohn-Sham (pseudo) wvae function expansion of the valence electrons while the atomic core is considered as frozen and treated using with the projector augmented wave (PAW) approach [162, 163].

Periodic boundary conditions forces to uses a supercell approach to represent a two dimensional structure such as graphene. From table 3.1 it is easy to recognize that both the binding energy and the height of the puckered carbon atom are sensitive respect to the supercell choice, hence to the surface coverage. Probably this comes from the very long-ranged nature of the midgap state that forms upon H chemisorption, which might need a very large cell to accomodate its spin density. We then opted for a 5x5 graphene supercell, with 50 carbon atoms per cell, as a good compromise between size and compututation cost. This is indeed not enough to give well converged results, as evident in table 3.1, but the difference in binding energies respect to much larger cells is still acceptable (few meV respect to a 8x8 supercell with 128 atoms [104]).

The interaction among graphite planes is van der Waals dominated. It is well known that this kind of interaction is very poorly represented within the framework of standard DFT [164]. Our tests showed that the attractive well for two graphene planes is only about 2 meV deep, while the experimental one should be of and located at about twice the experimental distance. This is in agreement with other studies [165], that exploited several approaches. For this reason we can extend the results obtained for graphene to graphite, since the inclusion of other layers will not effect the energetics of adsorption at this level of theory. Of course in the real system some differences must be expected. Then, in the work unit cell, we chose to add 20 Å of vacuum space along the c axis to separate the different graphene layers to guarantee no interlayer interaction.

About the other settings for the plane wave DFT simulation, several tests agreed in defining as optimal an energy cutoff of 500 eV, and a 6x6x1 Γ-centered k-points mesh for all the calculations. This ensures the inclusion of all the special points in the unit cell (M, K and K'), that are crucial to represent correctly the Dirac cones of graphene.The linear tetrahedron method with Blöchl corrections was used for all the band structure calculations: this is indeed the only interpolation scheme available in VASP to give a correct density of states for graphene. This is probably due to the fact that tetrahedra in their two-dimensional limit become triangles, that map well the hexagonal graphene structure, while other methods such as the Methfessel-Paxton fail for purely 2D structures.

In presence of hydrogen the use of GGA functionals is recommended. We adopted the PBE[166, 167] functional throughout, but it is worth notice that other GGA functionals such as PW91[168] gives almost identical results. Spin polarization (unrestricted DFT) was used in every calculation, being determinant to describe correctly midgap states and bond formation.

All the atomic positions have been fully relaxed until the Hellmann - Feynman forces dropped below 10^{-2} eV Å^{-1}, while convergence of the electronic structures has been ensured by forcing the energy difference in the self-consistent cycle to be below 10^{-6} eV. Note that the linear tetrahedron method give spurious forces when applied to structural relaxations: for this reason a gaussian smearing of 0.05 eV was used for all the geometrical optimizations.

To compute energy barriers for hydrogen chemisorption on graphene is particularly challenging. The activation barrier arises from the avoided crossing of two potential energy curves, as shown in fig.3.11. along one of the two potential curves the lone electron is localized on the H atom, while along the other it lays on the surface. Along the adsorbate descend towards the surface, when approaching the crossing the two electronic solutions become almost degenerate and often the algorithm follows the excited state curve, folling back on the ground state as soon as the curves are again well separates in energy. The result is a sharp

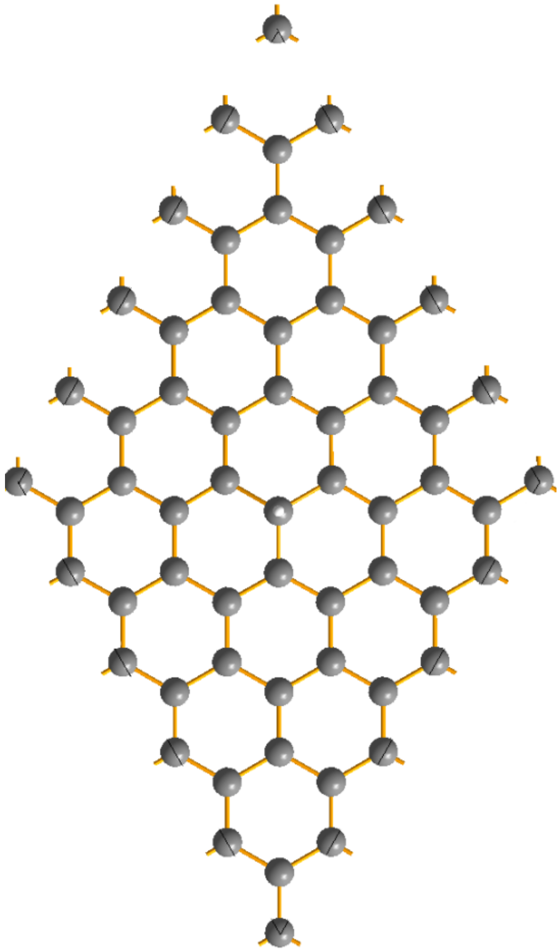

Figure B.1: View of the graphene 5x5 supercell adopted for most of the DFT calculations included in chapters 3 and 4.

barrier with an error of many meV. The nudged elastic band method gives the same spourious result. We then built the activation barrier by the crossing of the curve obtained by moving an H atom toward the surface and by pulling it out from graphene. At each step the carbon atom involved in the CH bond, and its first nearest-neighbours were fully relaxed.

Bibliography

[1] Avouris, P., Chen, Z., and Perebeinos, V. *Nat. Nanotech.* **2**, 605 (2007).

[2] Peierls, R. E. *Helv. Phys. Acta* **7**, 81 (1934).

[3] Hohenberg, P. *Phys. Rev.* **158**, 383 (1967).

[4] Mermin, N. D. and Wagner, H. *Phys. Rev. Lett.* **17**, 1133 (1966).

[5] Mermin, N. D. *Phys. Rev.* **176**, 250 (1968).

[6] Gelfert, A. and Nolting, W. *J. Phys.: Condens. Matter* **13**, R505–R524 (2001).

[7] Novoselov, K. S., Jiang, D., nad T. J. Booth, F. S., Khotkevich, V. V., Morozova, S. V., and Geim, A. K. *Proc. Natl. Acad. Sci. U.S.A.* **102**, 10451 (2005).

[8] Novoselov, K. S., Geim, A. K., Morozov, S. V., Jiang, D., Zhang, Y., Dubonos, S. V., Gregorieva, I. V., and Firsov, A. A. *Science* **306**, 666 (2004).

[9] Mohr, M., Maultzsch, J., Dobardžić, E., Reich, S., Milošević, I., Damnjanović, M., Bosak, A., Krisch, M., and Thomsen, C. *Phys. Rev. B* **76**, 035439 (2007).

[10] Wirtz, L. and Rubio, A. *Solid State Commun.* **131**, 141 (2004).

[11] Castro Neto, A. H., Guinea, F., Peres, N. M. R., Novoselov, K. S., and Geim, A. K. *Rev. Mod. Phys.* **81**, 109 (2009).

[12] Doussal, P. L. and Radzihovsky, L. *Phys. Rev. Lett.* **69**, 1209 (1992).

[13] Geim, A. and Novoselov, K. *Nat. Phys.* **6**, 183 (2007).

[14] Peres, N. M. R. *Vacuum* **83**, 1248 (2009).

[15] Katsnelson, M. I. and Novoselov, K. S. *Solid State Commun.* **143**, 3 (2007).

[16] Katsnelsons, M. I., Novoselov, K. S., and Geim, A. K. *Nat. Phys.* **2**, 620 (2006).

[17] Dombey, N. and Calogeracos, A. *Phys. Rep.* **315**, 41 (1999).

[18] Young, A. and Kim, P. *Nat. Phys.* **5**, 222 (2009).

[19] Stander, N., Huard, B., and Goldhaber-Gordon, D. *Phys. Rev. Lett.* **102**, 026807 (2009).

[20] Messiah, A. *Quantum mechanics*, chapter III. Dover Publications, Mineola, New York (1999).

[21] Viana Gomes, J. and Peres, N. M. R. *J. Phys.: Condens. Matter* **20**, 325221 (2008).

[22] Beenakker, C. W. J. *Rev. Mod. Phys.* **80**, 1337 (2008).

[23] Messiah, A. *Quantum mechanics*, chapter XX. Dover Publications, Mineola, New York (1999).

[24] Peres, N. M. R., Castro Neto, A. H., and Guinea, F. *Phys. Rev. B* **73**, 241403 (2006).

[25] Latil, S. and Henard, L. *Phys. Rev. Lett.* **97**, 036803 (2006).

[26] Latil, S., Meunier, V., and Henard, L. *Phys. Rev. B* **76**, 201402 (2007).

[27] Hass, J., Varchon, F., Millán-Otoya, J. E., Sprinkle, M., Sharma, N., de Heer, W. A., Berger, C., First, P. N., Magaud, L., and Conrad, E. H. *Phys. Rev. Lett.* **100**, 125504 (2008).

[28] Charlier, J., Gonze, X., and Michenaud, J. *Phys. Rev. B* **43**, 4579 (1991).

[29] Novoselov, K. S., Geim, A. K., Morozov, S. V. S. V., Jiang, D., Katsnelson, M. I., Gregorieva, I. V., Dubonos, S. V., and Firsov, A. A. *Nature* **438**, 197 (2005).

[30] Zhang, Y., Tan, Y.-W., Stormer, H. L., and Kim, P. *Nature* **438**, 201 (2005).

[31] Chen, J. H., Jang, C., Xiao, S., Ishigami, M., and Fuhrer, S. *Nat. Nanotech.* **3**, 206 (2008).

[32] Lin, Y.-M., Jenkins, K. A., A. Valdes-Garcia, J. P. S., Farmer, D. B., and Avouris, P. *Nano Lett* **9**, 422 (2009).

[33] Peres, N. M. R. *J. Phys.: Condens. Matter* **21**, 323201 (2009).

[34] Tworzydlo, J., Trauzettel, B., Titov, M., Rycerz, A., and Beenakker, C. W. J. *Phys. Rev. Lett.* **96**, 246802 (2006).

[35] Miao, F., Wijeratne, S., Zhang, Y., Coskun, U. C., Bao, W., and Lau, C. N. *Science* **317**, 1530 (2007).

[36] Cresti, A., Nemec, N., Biel, B., Niebler, G., Triozon, F., Cuniberti, G., and Roche, S. *Nano Res.* **1**, 361 (2008).

[37] Barone, V., Hod, O., and Scuseria, G. E. *Nano Lett* **6**, 2748 (2006).

[38] Han, M. Y., Özyilmaz, B., Zhang, Y., and Kim, P. *Phys. Rev. Lett.* **98**, 206805 (2007).

[39] Tapaszto, L., Dobrik, G., Lambin, P., and Biro, L. P. *Nat. Nanotech.* **3**, 397 (2008).

[40] Casolo, S., Løvvik, O. M., Martinazzo, R., and Tantardini, G. F. *J. Chem. Phys.* **130**, 054704 (2009).

[41] Mattausch, A. and Pankratov, O. *Phys. Rev. Lett.* **99**, 076802 (2007).

[42] Otha, T., El Gabaly, F., Bostwick, A., McChesney, J., Emstev, K. V., Schmidt, A. K., Seyller, T., and Horn, K. *New J. Phys.* **10**, 023034 (2007).

[43] Zhou, S. Y., Gweon, G.-H., Fedorov, A. V., de Heer, A. W., Lee, D.-H., Guinea, F., Castro Neto, A. H., and Lanzara, A. *Nat. Mater.* **6**, 770 (2007).

[44] Otha, T., Bostwick, A., McChesney, J., Seyller, T., horn, K., and Rothenberg, E. *Phys. Rev. Lett.* **98**, 206803 (2007).

[45] Pedersen, T., Flindt, C., Pedersen, J., Mortensen, N., Jauho, A. P., and Pedersen, K. *Phys. Rev. Lett.* **100**, 136804 (2008).

[46] Fürst, J. A., Pedersen, J. G., Flindt, C., Mortensen, N. A., Brandbyge, M., Pedersen, T. G., and Jauho, A. P. *New J. Phys.* **11**, 095020 (2009).

[47] Vanević, M., Stojanović, V. M., and Kindermann, M. *Phys. Rev. B* **80**, 045410 (2009).

[48] Schedin, F., Geim, A. K., Morozov, S. V., Hil, E. W., Blake, P., Katsnelson, M. I., and Novoselov, K. S. *Nat. Mater.* **6**, 652 (2007).

[49] Park, C. H., Lee, Y. H., Yang, L., Cohen, M. L., and Louie, S. G. *Nano Lett* **8**, 2920 (2008).

[50] Blake, P., Brimicombe, P. D., Nair, R. R., Booth, T. J., Jiang, D., Schedin, F., Ponomarenko, L. A., Morozov, S. V., Gleeson, H. F., Hill, E. W., Geim, A. K., and Novoselov, K. S. *Nano Lett* **8**, 1704 (2008).

[51] Geim, A. K. *Science* **324**, 1530 (2009).

[52] Küppers, J. *Surf. Sci. Rep.* **22**, 249 (1995).

[53] Schlapbach, L. and Zuttel, A. *Nature* **414**, 353 (2001).

[54] Shevlin, S. A. and Guo, Z. X. *Chem. Soc. Rev.* **38**, 211 (2009).

[55] Sandrock, G. *J. Alloys Comp.* **293**, 877 (1999).

[56] Sims, I. and Smith, I. W. M. *Annu. Rev. Phys. Chem.* **46**, 109 (1995).

[57] van Dishoeck, E. F. and Blake, G. A. *Annu. Rev. Astron. Astrophys.* **36**, 317 (1998).

[58] Kaiser, R. I. *Chem. Rev.* **102**, 1309 (2002).

[59] Herbst, E. *Chem. Soc. Rev* **30**, 168 (2001).

[60] Ehrenfreund, P., Irvine, W., Becker, L., Blank, J., Brucato, J., Colangeli, L., Derenne, S., Despois, D., Dutery, A., Fraaji, H., Lanczano, A., Owen, T., and Robert, F. *Rep. Prog. Phys.* **65**, 1427 (2002).

[61] Gould, R. J. and Salpeter, E. E. *Astrophys. J.* **138** 393 (1963).

[62] Hollenbach, D. and Salpeter, E. E. *J. Chem. Phys.* **53**, 79 (1970).

[63] Greenberg, J. M. *Surf. Sci.* **500**, 793 (2002).

[64] Parr, R. G. and Yang, W. *Density functional theory of atoms and molecules.* Oxford Univ. Press, (1989).

[65] Gritsenko, O. V. and Baerends, E. J. *Theoret. Chim. Acta* **96**, 44 (1997).

[66] von Barth, U. and Hedin, L. *J. Phys C.* **5**, 1629 (1972).

[67] Ceperley, D. M. and Adler, B. J. *Phys. Rev. Lett.* **45**, 566 (1980).

[68] Kümmel, S. and Kronik, L. *Rev. Mod. Phys.* **80**, 3 (2008).

[69] Perdew, J. P. and Kurth, S. In *A primer in density functional theory,* Fiolhais, C., Nogueira, F., and Marques, M., editors, Lecture notes in physics. Springer, Heidelberg (2003).

[70] Martin, R. M. *Electronic Structure.* Cambridge Univ. Press, (2004).

[71] Dreizler, R. M. and Gross, E. K. U. *Density Functional Theory.* Springer, Heidelberg, (1990).

[72] Perdew, G. B., Parr, R. G., Levy, M., and Balduz Jr., J. L. *Phys. Rev. Lett.* **49**, 1691 (1982).

[73] Cohen, A. J., Mori-Sanchez, P., and Yang, W. *Science* **321**, 792 (2008).

[74] Cohen, A. J., Mori-Sanchez, P., and Yang, W. *J. Chem. Phys.* **129**, 121104 (2008).

[75] Inui, M., Trugman, S. A., and Abrahams, E. *Phys. Rev. B* **49**, 3190 (1994).

[76] Lieb, E. H. and Mattis, D. *Phys. Rev.* **125**, 164 (1962).

[77] Lieb, E. H. *Phys. Rev. Lett.* **62**, 1201 (1989).

[78] Shen, S., Qiu, Z., and Tian, G. *Phys. Rev. Lett.* **72**, 1280 (1994).

[79] Stefanucci, G. and Cini, M. *Phys. Rev. B* **66**, 115108 (2002).

[80] Heitler, W. and London, F. *Zeit. fur Phys.* **44**, 455 (1927).

[81] Pauling, L. and Wilson, E. B. *Introduction to quantum mechanics with applications to chemistry.* McGraw-Hill Book Company, (1935).

[82] Tantardini, G. F., Raimondi, M., and Simonetta, M. *Int. J. of. Quant. Chem.* **7**, 893 (1973).

[83] Goddard, W. A., Dunning, T. H., Hunt, W. J., and Hay, P. J. *Acc. Chem. Res.* **6**, 368 (1973).

[84] Cooper, D. L., Gerratt, J., and Raimondi, M. In *Ab initio methods in quantum chemistry II,* Lawley, K. P., editor. John Wiley & Sons Ltd. (1987).

[85] Cooper, D. L., Gerratt, J., and Raimondi, M. *Chem. Rev.* **91**, 929 (1991).

[86] Gerratt, J., Cooper, D. L., Karadakov, P. B., and Raimondi, M. *Chem. Soc. Rev.* **26**, 87 (1997).

[87] Raimondi, M., Simonetta, M., and Tantardini, G. F. *Comp. Phys. Rep.* **2**, 171 (1985).

[88] Tantardini, G. F., Raimondi, M., and Simonetta, M. *J. Am. Chem. Soc.* **99**, 2913 (1977).

[89] Bonfanti, M., Martinazzo, R., Tantardini, G. F., and Ponti, A. *J. Phys. Chem. C* **111**, 5825 (2007).

[90] Sha, X. and Jackson, B. *Surf. Sci.* **496**, 318 (2002).

[91] Jeloaica, L. and Sidis, V. *Chem. Phys. Lett.* **300**, 157 (1999).

[92] Zecho, T., Güttler, A., Sha, X., Jackson, B., and Küppers, J. *J. Chem. Phys.* **117**, 8486 (2002).

[93] Gavardi, E., Cuppen, H. M., and Hornekær, L. *Chem. Phys. Lett.* **477**, 285 (2009).

[94] Cuppen, H. M. and Hornekær, L. *J. Chem. Phys.* **128**, 174707 (2008).

[95] Yazyev, O. V. and Helm, L. *Phys. Rev. B* **75**, 125408 (2007).

[96] Palacios, J. J., Fernandez-Rossier, J., and Brey, L. *Phys. Rev. B* **77**, 195428 (2008).

[97] Pereira, V. M., Guinea, F., Lopes dos Santos, J., Peres, N., and Castro Neto, A. *Phys. Rev. Lett.* **96**, 036801 (2006).

[98] Kerwin, J. and Jackson, B. *J. Chem. Phys.* **128**, 084702 (2008).

[99] Ferro, Y., Marinelli, F., and Allouche, A. *Chem. Phys. Lett.* **368**, 609 (2003).

[100] Duplock, E. J., Scheffler, M., and Lindan, P. J. D. *Phys. Rev. Lett.* **92**, 225502 (2004).

[101] Hornekær, L., Rauls, E., Xu, W., Šljivančanin, Ž., Otero, R., Stensgaard, I., Læegsgaard, E., Hammer, B., and Besenbacher, F. *Phys. Rev. Lett.* **97**, 186102 (2006).

[102] Roman, T., Diño, W. A., Nakanishi, H., Kasai, H., Sugimoto, T., and Tange, K. *Carbon* **45**, 203 (2007).

[103] Chen, L., Cooper, A. C., Pez, G. P., and Cheng, H. *J. Phys. Chem. C* **111**, 18995 (2007).

[104] Lethinen, P. O., Foster, A. S., Ma, Y., Krasheninnikov, A. V., and Nieminen, R. M. *Phys. Rev. Lett.* **93**, 187202 (2004).

[105] Ruffieux, R., Gröning, O., Schwaller, P., and Schlapbach, L. *Phys. Rev. Lett.* **84**, 4910 (2000).

[106] Buchs, G., Krasheninnikov, A. V., Ruffieux, P., Gröning, P., Foster, A. S., Nieminen, R. M., and Gröning, O. *New J. Phys.* **9**, 275 (2007).

[107] Šljivančanin, Ž., Rauls, E., Hornekær, L., Xu, W., Besenbacher, F., and Hammer, B. *J. Chem. Phys.* **131**, 084706 (2009).

[108] Güttler, A., Zecho, T., and Küppers, J. *Surf. Sci.* **570**, 218 (2004).

[109] Güttler, A., Zecho, T., and Küppers, J. *Chem. Phys. Lett.* **395**, 171 (2004).

[110] Zecho, T., Güttler, A., and Küppers, J. *Carbon* **42**, 609 (2004).

[111] Allouche, A., Ferro, Y., Angot, T., Thomas, C., and Layet, J.-M. *J. Chem. Phys.* **123**, 124701 (2005).

[112] Ruffieux, P., Melle-Franco, M., Gröning, O., Bielmann, M., Zerbetto, F., and Gröning, P. *Phys. Rev. B* **71**, 153403 (2005).

[113] Bonfanti, M. unpublished.

[114] Andree, A., Le Lay, M., Zecho, T., and Küppers, J. *Chem. Phys. Lett.* **425**, 99 (2006).

[115] Rogeau, N., Teillet-Billy, D., and Sidis, V. *Chem. Phys. Lett.* **431**, 135 (2006).

[116] Hornekær, L., Šljivančanin, Ž., Xu, W., Otero, R., Rauls, E., Stensgaard, I., Lægsgaard, E., Hammer, B., and Besenbacher, F. *Phys. Rev. Lett.* **96**, 156104 (2006).

[117] Boukhvalov, D. W., Katsnelson, M. I., and Lichtenstein, A. I. *Phys. Rev. B* **77**, 035427 (2008).

[118] Denis, P. A. and Iribane, F. *J. Mol. Struc. THEOCHEM* **907**, 93 (2009).

[119] Hornekær, L., Xu, W., Otero, R., Zecho, T., Lægsgaard, E., and Besenbacher, F. *Chem. Phys. Lett.* **446**, 237 (2007).

[120] Ferro, Y., Morisset, S., and Allouche, A. *Chem. Phys. Lett.* **478**, 42 (2009).

[121] Sofo, J. O., Chaudhari, A. S., and Barber, G. D. *Phys. Rev. B* **75**, 153401 (2007).

[122] Elias, D. C., Nair, R. R., Mohiuddin, T. M. G., Morozov, S. V., Blake, P., Halsall, M. P., Ferrari, A. C., Boukhvalov, D. W., Katsnelson, M. I., Geim, A. K., and Novoselov, K. S. *Science* , 5914 (2009).

[123] Flores, M. Z. S., Autreto, P. A. S., Legoas, S. B., and Galvao, D. S. *Nanotechnology* **20**, 465704 (2009).

[124] Balog, R., Jørgensen, B., Wells, J., Lægsgaard, E., Hofmann, P., Besenbacher, F., and Hornekær, L. *J. Am. Chem. Soc.* **131**, 8744 (2009).

[125] Luo, Z., Yu, T., Kim, K., You, Y., Lim, S., Shen, Z., Wang, S., and Lin, J. *ACS Nano* **3**, 1781 (2009).

[126] Jung, N., Kim, N., Jockusch, S., Turro, N. J., Kim, P., and Brus, L. *Nano Lett.* **8**, 4597 (2009).

[127] Ruffieux, P., Gröning, O., Bielmann, M., Mauron, P., Schlapbach, L., and Gröning, P. *Phys. Rev. Lett.* **66**, 245416 (2002).

[128] Ruffieux, P., Gröning, O., Bielmann, M., Mauron, P., Schlapbach, L., and Gröning, P. *Phys. Rev. B* **66**, 245416 (2002).

[129] Ghio, E., Mattera, L., Salvo, C., Tommasini, F., and Valbusa, U. *J. Chem. Phys.* **73**, 556 (1980).

[130] Creighan, S. C., Perry, J. S., and Price, S. D. *J. Chem. Phys.* **124**, 114701 (2006).

[131] Islam, F., Latimer, E. R., and Price, S. D. *J. Chem. Phys. 127* **127**, 064701 (2007).

[132] Tannor, D. J. *Introduction to Quantum Mechanics: A Time-Dependent Perspective.* University Science Books, (2006).

[133] Balakrishnan, N., Kalyanaraman, C., and Sathyamurty, N. *Phys. Rep.* **280**, 79 (1997).

[134] Fleck, J. J. A., Morris, J. R., and Feit, M. D. *Appl. Phys.* **10**, 129 (1976).

[135] Feit, M. D. and Fleck Jr., J. A. *J. Chem. Phys.* **78**, 301 (1983).

[136] Trotter, H. F. *Proc. Am. Math. Soc.* **10**, 545 (1959).

[137] Suzuki, M. *Commun. Math. Phys.* **51**, 183 (1976).

[138] Suzuki, M. *J. Math. Phys.* **34**, 4892 (1993).

[139] Manolopoulos, D. E. *J. Chem. Phys.* **117**, 9552 (2002).

[140] Martinazzo, R. and Tantardini, G. F. *J. Chem. Phys.* **122**, 094109 (2005).

[141] Persson, M. and Jackson, B. *J. Chem. Phys.* **102**, 1078 (1995).

[142] Lemoine, D. and Jackson, B. *Comput. Phys. Commun.* **137**, 415 (2001).

[143] Martinazzo, R. and Tantardini, G. F. *J. Chem. Phys.* **124**, 124703 (2006).

[144] Jackson, B. and Lemoine, D. *J. Chem. Phys.* **144**, 474 (2001).

[145] Meijer, A., Farebrother, A., and Clary, D. *J. Phys. Chem. A* **105**, 2173 (2001).

[146] Meijer, A., Farebrother, A., and Clary, D. *J. Phys. Chem. A* **106**, 8996 (2002).

[147] Meijer, A., Fisher, A., and Clary, D. *J. Phys. Chem. A* **107**, 10862 (2003).

[148] Morisset, S., Aguillon, F., Sizun, M., and Sidis, V. *Phys. Chem. Chem. Phys.* **5**, 506 (2003).

[149] Morisset, S., Aguillon, F., Sizun, M., and Sidis, V. *J. Chem. Phys.* **121**, 6493 (2004).

[150] Bachellerie, D., Sizun, M., Anguillon, F., Teillet-Billy, D., Rougeau, N., and Sidis, V. *Phys. Chem. Chem. Phys.* **11**, 2715 (2009).

[151] Rutigliano, M., Cacciatore, M., and Billing, G. *Chem. Phys. Lett.* **340**, 13 (2001).

[152] Rutigliano, M. and Cacciatore, M. *Chem Phys Chem* **9**, 171 (2008).

[153] Ko, Y., Ree, J., Kim, Y., and Shin, H. *Bull. Kor. Chem. Soc.* **23**, 1737 (2002).

[154] Ree, J., Kim, Y., and Shin, H. *Chem. Phys. Lett.* **353**, 368 (2002).

[155] Ree, J., Kim, Y., and Shin, H. *Bull. Kor. Chem. Soc.* **28**, 635 (2007).

[156] Martinazzo, R. and Tantardini, G. F. *J. Chem. Phys.* **124**, 124702 (2006).

[157] Martinazzo, R. and Tantardini, G. F. *J. Phys. Chem. A* **109**, 9379 (2005).

[158] Frisch, M. J., Trucks, G. W., Schlegel, H. B., Scuseria, G. E., Robb, M. A., Cheeseman, J. R., Zakrzewski, V. G., Jr., J. A. M., Stratmann, R. E., Burant, J. C., Dapprich, S., Millam, J. M., Daniels, A. D., Kudin, K. N., Strain, M. C., Farkas, O., Tomasi, J., Barone, V., Cossi, M., Cammi, R., Mennucci, B., Pomelli, C., Adamo, C., Clifford, S., Ochterski, J., Petersson, G. A., Ayala, P. Y., Cui, Q., Morokuma, K., Malick, D. K., Rabuck, A. D., Raghavachari, K., Foresman, J. B., Cioslowski, J., Ortiz, J. V., Baboul, A. G., Stefanov, B. B., Liu, G., Liashenko, A., Piskorz, P., Komaromi, I., Gomperts, R., Martin, R. L., Fox, D., Keith, T., Al-Laham, M. A., Peng, C. Y., Nanayakkara, A., Gonzalez, C., Challacombe, M., Gill, P. M. W., Johnson, B., Chen, W., Wong, M. W., Andres, J. L., Gonzalez, C., Head-Gordon, M., Replogle, E. S., , and and, J. A. P. *Gaussian 98, Revision A.7.* Gaussian Inc., Pittsburgh PA, (1998).

[159] Bena, C. and Montambaux, G. *New J. Phys.* **11**, 095003 (2009).

[160] Kresse, G. and Furthmller, J. *Comput. Mat. Sci.* **6**, 15 (1996).

[161] Kresse, G. and Furthmller, J. *Phys. Rev. B* **54**, 11169 (1996).

[162] Blöchl, P. E. *Phys. Rev. B* **50**, 17953 (1994).

[163] Kresse, G. and Joubert, D. *Phys. Rev. B* **59**, 1758 (1999).

[164] Girifalco, L. A. and Hodak, M. *Phys. Rev. B* **65**, 125404 (2002).

[165] Hasegawa, M. and Nishidate, K. *Phys. Rev. B* **70**, 205431 (2004).

[166] Perdew, J. P., Burke, K., and Ernzerhof, M. *Phys. Rev. Lett.* **77**, 3865 (1996).

[167] Perdew, J. P., Burke, K., and Ernzerhof, M. *Phys. Rev. Lett.* **78**, 1396 (1997).

[168] Perdew, J. P. In *Electronic Structure of Solids '91,* Ziesche, P. and Eschrig, H., editors, 11. Akademie Verlag, Berlin (1991).